Interaction of Light with Metallized Ultrathin Silicon Membrane

by

Krishanu Shome

Submitted in Partial Fulfillment

of the

Requirements for the Degree

Doctor of Philosophy

Supervised by

Professor Philippe M. Fauchet

The Institute of Optics
Arts, Sciences and Engineering
Edmund A. Hajim School of Engineering and Applied Sciences

University of Rochester
Rochester, New York

2013

Biographical Sketch

The author was born in Burnpur, West Bengal, India in 1982. He received his Bachelors in Science with Honours in Physics from Presidency College, Kolkata under the University of Calcutta in 2004. He received his Masters in Physics from Indian Institute of Technology Bombay, Mumbai in 2006. He joined the Institute of Optics at the University of Rochester under a fellowship in 2006. He has been a Research Assistant under Professor Philippe M Fauchet from summer of 2007 to September 2012. He is currently working as an optical design engineer, in a company associated with the semiconductor industry.

List of Publications

K. Shome, M. N. Kavalenka, D. Z. Fang, and P. M. Fauchet, "Metallized Ultrathin Porous Silicon Membranes for Biological Sensing Using SERS", Frontiers in Pathogen Detection: from Nanosensors to Systems, SPIE, Vol. 7553, pp.75530F-9, 2010.

K. Shome and P. M. Fauchet, "Metallized Ultrathin Porous Silicon Membranes as Surface Plasmon Resonance Sensors", manuscript in preparation.

K. Shome and P.M. Fauchet, "Slot effect in Nanoholes", manuscript in preparation.

Presentations

K. Shome, M. N. Kavalenka, and P. M. Fauchet, 'Metallized Ultrathin Nanocrystalline Si Membranes as Biochemical SPR Sensors', CLEO 2011, Baltimore, MD.

K. Shome, M. N. Kavalenka, and P. M. Fauchet, 'Chemical and Biological Detection using Surface Plasmon Resonance in Metallized Ultrathin Porous Silicon Membranes', BiOS, SPIE Photonics West 2011, San Francisco, CA.

K. Shome, M. N. Kavalenka, and P. M. Fauchet, 'SPR in Metallized Ultrathin Porous Membranes for Biological and Chemical Sensing', Materials Research Society, Fall 2010 Meeting, Boston, MA.

K. Shome, M. N. Kavalenka, D. Z. Fang, and P. M. Fauchet, ‘Metallized Ultrathin Porous Membranes for Biological and Chemical Sensing’, 2010 Frontiers in Optics/Laser Science in Rochester, NY.

K. Shome, M. N. Kavalenka, D. Z. Fang, and P. M. Fauchet, 'Metallized ultrathin porous silicon membranes for biological sensing using SERS', conference presentation at BiOS, SPIE Photonics West 2010, San Francisco, CA.

K. Shome and P. M. Fauchet, ‘Nano-holes and Slot Effect’, 2012 Frontiers in Optics/Laser Science in Rochester, NY.

Acknowledgement

I would like to thank my advisor, Professor Philippe M. Fauchet who has over the years been patient with me, and given me the independence and opportunity to pursue my research.

I am indebted to the help received from Professor James L. McGrath and his group during the last stages of my research. I am grateful to Brian McIntyre and Alex Mann from URnano, who helped me with issues during the fabrication process.

I would like to thank all the past and present members of the Fauchet group who were always willing to help out in any problems and helped in creating a collaborative environment in the group. Thank you, Maryna Kavalenka, Josh Winans, Jo Qi, Adam Heiniger, Chanse Hungerford, Karl Ni, Jonathan Lee, Sean Anderson, Chris Striemer, Halina Krzyzanowska, Stanley Lo, David Fang, Sudeshna Pal, Elisa Guillermain, Yijing Fu, Lingyun Miao, Mindy Lee, Jeff Clarkson, Han Yoo, Jidong Zhang, Gloria See and Xi Liu. Thanks are also due to Victoria Heberling, Betsy Bendict and Audrey Pierce for help with administrative issues.

Lastly I would like to thank my family and friends, scattered in different parts of the world, who have constantly been a source of support.

Abstract

Freestanding metallized structures, a few tens of nanometer thick, show promise in creating flow-through sensors, single molecule detectors and novel solar cells. In this thesis we study test structures that are a step towards creating such devices. Finite-difference time-domain simulations have been used to understand and predict the interaction of light with such devices. Porous nanocrystalline silicon membrane is a novel freestanding layer structure that has been used as a platform to fabricate and study sensors and novel slot nanohole devices. Optical mode studies of the sensing structures, together with the method of fabrication inspired the creation of ultrathin freestanding hydrogenated amorphous silicon p-i-n junctions solar cells. All the freestanding structures used in this thesis are just a few tens of nanometers in thicknesses.

In the first part of the thesis the sensing properties of the metallized porous nanocrystalline structure are studied. The surprising blueshift associated with the sensing peak is observed experimentally and predicted theoretically with the help of simulations. Polarization dependence of the membranes is predicted and confirmed for angled deposition of metal on the membranes.

In the next part, a novel slot structure is fabricated and modeled to study the slot effect in nanohole metal-insulator-metal structures. Atomic layer deposition of alumina is used to conformally deposit alumina within the nanohole to create the slot structure. Simulation models were used to calculate the lowest modal volume of 4×10^{-5} μm^3 for an optimized structure.

In the last part of the thesis, freestanding solar cells are fabricated by effectively replacing the porous nanocrystalline silicon layer of the membranes with a hydrogenated amorphous silicon p-i-n junction with metal layers on both sides of the p-i-n junction. The metal layers act both as electrical contacts as well as mirrors for a Fabry Perot cavity resonator. This helps in tuning the absorption profile of the solar cell to target near infrared part of the solar spectrum. A correspondence is found between the simulation absorption results with the experimental spectral response of the solar cells. This helps in designing metallized solar cells with ITO layer to improve absorption and hence the efficiency.

Contributors and Funding Sources

The work has been done under the supervision of Professor Philippe M. Fauchet and under the guidance of the thesis committee comprised of Professor Lukas Novotny, Professor Andrew J. Berger and Professor Qiang Lin.

The author performed all experiments and analysis in this thesis except for the collaborations below.

The porous nanocrystalline membranes used in the sensing experiments were obtained from David Z. Fang. Metallization of the membranes was done in collaboration with Maryna N. Kavalenka. Transmission electron microscopy studies on the metallized membranes were done with the help of Maryna N. Kavalenka. Thiol sensing experiments were performed under the supervision of Professor Benjamin L. Miller with the help of Hsin-I Peng. Chengzhu Qi fabricated the porous nanocrystalline membranes used in the slot effect part of the thesis. Transmission electron microscopy on the slot membranes was done with Chengzhu Qi's help. The fabrication of the hydrogenated amorphous silicon p-i-n junction was performed by the collaborative effort of Joshua D. Winans, Chengzhu Qi, Chanse Hungerford and Adam Heiniger. The ITO deposition over the metallized solar cells was performed with the help of Joshua D. Winans.

Chapter 3 is partially derived from a paper titled, "Metallized Ultrathin Porous Silicon Membranes as Surface Plasmon Resonance Sensors", whose manuscript is under preparation. Chapter 4 is derived from the paper whose manuscript is in preparation titled, "Slot effect in Nanoholes". Chapter 5 is comprised of unpublished data.

The author acknowledges the CEIS Bio Imaging Program, supported by New York State, and SIMPore Inc. as funding for this work. Resources at the Center for Integrated Research Computing were used to run simulations.

Table of Contents

List of Figures

Chapter 1 Introduction

1.1 Membranes

All living cells must communicate with each other, exchange nutrients and excrete waste materials to function as the basic building blocks of life. The membrane is an essential component of this complex biological mechanism. The function of membranes in organisms is to separate and physically hold material inside a cell. They constitute an important part of the outer structure that provides mechanical support to the cell. We, as a species have tried to imitate nature by creating devices to suit our needs and purposes. Membrane with holes is the obvious choice for mimicking natural living membranes. The porous membrane can provide a platform for molecular separation, one of the basic functions of a cell membrane. To this respect, many porous membranes have been synthetically built from inorganic and organic materials as well. These include tracked etched membranes [1], anodic alumina membrane [2], carbon nanotube membrane [3] and ultrathin membranes [4,5]. All these types of membranes have drawbacks either in their structure, some are too thick or brittle, or because of the high manufacturing cost. The invention of the porous nanocrystalline silicon [6] (pnc-Si) membrane mitigates some of these problems and provides a unique platform in membrane technology.

Pnc-Si membranes are ultrathin freestanding nanocrystalline films of Si with nanoholes in them. A schematic comparing the novel pnc-Si membrane to the conventional tortuous path membrane is shown in Figure 1.1. Pnc-Si membranes are

made using scalable, Si wafer based and standard semiconductor fabrication process. The nanoscale holes are spontaneously formed during the rapid phase change of a thin Si layer from amorphous to nanocrystalline. No postproduction expensive hole drilling or precision lithographic processing is needed. These free standing membranes can be a few nanometers in thickness yet can cover up to a few square millimeters in size. They can have high porosity with a narrow pore size distribution. These properties give the membrane a unique advantage over other membranes; the resistance offered to particles flowing through these membranes is substantially lower than anything comparable.

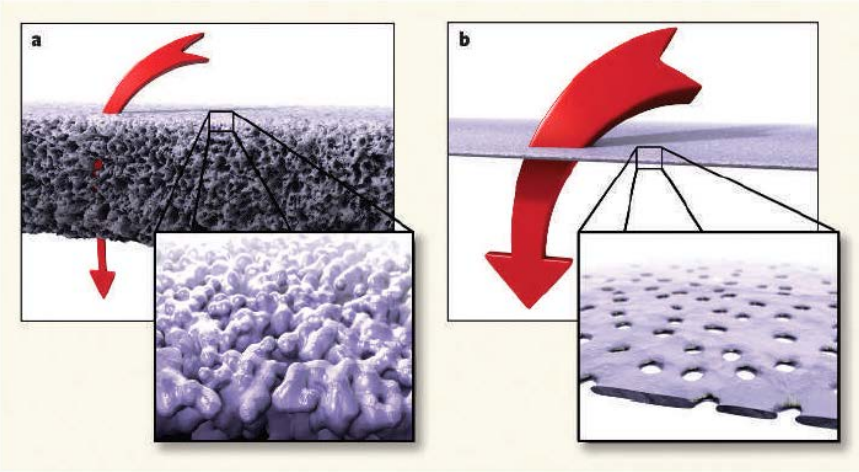

Figure 1.1: Comparison of pnc-Si membrane with conventional membranes. a) In conventional membranes with thicknesses of microns, the path taken by the molecules is a tortuous path. b) In ultrathin pnc-Si membranes with a thickness of a few nanometers, the flow rate is much higher as the resistance offered by the membrane material is several orders of magnitude smaller than the conventional membrane. [Reprinted by permission from Macmillan Publishers Ltd: Nature [7], copyright (2007)]

The gas permeance property of the pnc-Si membrane is orders of magnitude higher than comparable membranes [8]. These membranes have shown significant ability to separate molecules [9] and nanoparticles [10] and also act as substrates for cell

cultures [11]. The membrane structure provides a basic platform for the distinctive structures and their applications studied in this thesis.

1.2 Metallized Pnc-Si Membranes and Sensing

Nanoholes have been used to establish the size of small molecules [12] and proteins [13–15], the electrophoretic forces [16] and zeta potential [17] of molecules using electrical measurements. Nanoholes in metal films have been used in sensing [18 – 23] including single molecule sensing [24, 25], and in flow-through sensing [18, 26, 27] using optical measurements. Because they are ultrathin, the freestanding membranes let molecules pass through them without much resistance [8]. The narrow hole size distribution allows them to act as precise size-based filters [9, 10]. One goal of this thesis was to utilize these properties and create a sensor, capable of identifying the molecule passing through it and also to study the dynamics of the diffusion process through the nanoholes in these ultrathin membranes.

When metal is deposited on the pnc-Si structure with the holes open, a unique insulating metal structure is created with nanoholes [28]. A scanning electron microscopic image showing the cross-section of the membrane is contained in Figure 1.2. The interaction of light with holes of diameter much less than the wavelength of light has generated a lot of interest [29–31]. The extraordinary transmission of light (EOT) phenomena associated with the sub-wavelength apertures in metallic films have been studied experimentally [31–33] as well as theoretically [34, 35]. Some of the various methods for studying the interaction of light with the nanoholes are the multiple-

multimode method [36], Green's dyadic method [37, 38] and finite-difference time domain (FDTD) methods [39 – 41]. In most cases, a single hole or array of nanoholes is analyzed in metal films. FDTD simulations are faster and more accurate than other methods but the grid size for metal interfaces must be small leading to large computational memory requirements. However, the speed, ease of use and accuracy of FDTD makes it a preferred tool in this work. Both, single hole structures as well as a distribution of hole sizes imitating the real metallized pnc-Si membrane are studied in this work using FDTD simulations. The simulation tool becomes an integral part in understanding the sensing properties of these metallized pnc-Si membranes.

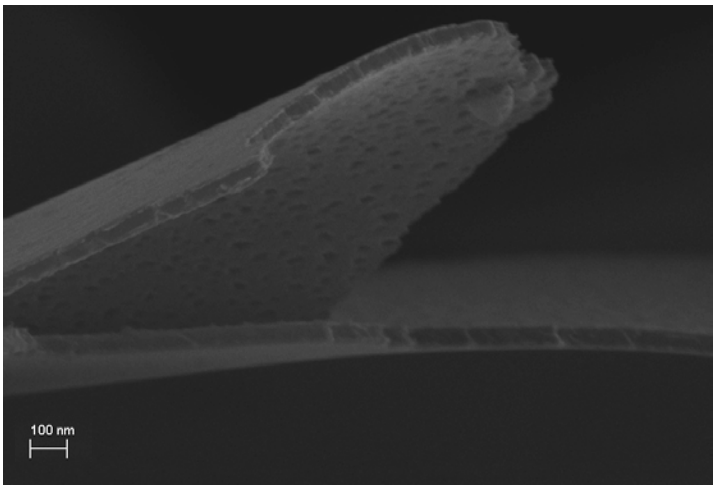

Figure 1.2: Scanning electron microscope image of the metallized membrane showing the cross-sectional view of the metallized pnc-Si membrane. 15 nm of metal is deposited on both sides of the 30 nm pnc-Si membrane. The upper part shows a piece of the broken metallized membrane, inclined at an angle, with the nanoholes seen on the surface. The lower part shows the cross-sectional view of the same membrane.

1.3 Pnc-Si Membranes and Slot effect

The fluorescence rate of a single molecule depends on the photonic environment [42]. This rate can be enhanced or quenched depending on various factors [43]. A common way to enhance fluorescence from single molecules is to manipulate the photonic environment by using the plasmonic interaction of light with metal nanostructures [44,45]. This manipulation of the local field also influences the molecule's emission rate, lifetime and quantum efficiency. Some examples of these metal nanostructures are metallic nanoparticles [46 – 48], core-shell particles [49], thin metal films [50], nanohole arrays [51 – 55] and single nanoholes [24, 56]. The nanohole based enhancement is specifically relevant as it reduces the volume of analyte interacting with the optical field [25, 32] and allows for easier microfluidic integration [57].

The pnc-Si membrane used in this work with its high permeance is a good candidate for future integration. However, simulation results [58] have shown that the plasmonic field enhancement on such ultrathin metallized pnc-Si films is not as high as currently seen in literature [58–60].

In a slot waveguide a region of low refractive index material is present within the core of a waveguide [61]. The continuity of Maxwell's equations, across the low index slot and the higher index waveguide core boundary, enhances and localizes the electric field inside the slot, for an incident polarization perpendicular to the boundary. Slot waveguides have been used in sensing [62, 63] and for optical manipulation of nanoparticle and biomolecules [64]. The ultra-small mode volumes obtained from the slot cavities in photonic crystal waveguides have been found to increase the Purcell

enhancement factor [65]. The fabrication of these slots, however, demands the use of high precision electron beam lithography and is a top-down processing.

In this work, a bottom-up process is used to make air slots inside the nanoholes in the metallized pnc-Si membrane. Atomic layer deposition (ALD) is used to deposit a conformal layer of Al_2O_3 around the nanohole. This method of fabrication is advantageous because the simple ALD process is capable of providing precise control over the deposition thickness of Al_2O_3 without the use of precision lithography. Simulation results show that creating slots inside the metallized pnc-Si structure decreases the modal volume of the slot and increases the Purcell factor. The work here shows that this type of nanohole based slot devices can be fabricated and demonstrate promise in flow-through single molecule fluorescence measurements.

1.4 Ultrathin Metallized Membrane based Solar Cells

The cost associated with greenhouse gases and climate change is prohibitive [66]. Solar energy is a safe and abundant alternative [67–69] to fossil fuels for mitigation of negative environmental effects. Conversion of the solar energy directly to electricity using solar cells is called photovoltaics. To make the solar energy a viable and popular alternative energy source, the cost per unit watt must be kept low. To keep the time and cost of manufacturing down, the solar cells should be easy to manufacture and the material, cheap and abundant. Silicon is the second most abundant element in the Earth's crust [70]. It is non-toxic and easy to handle. However, Si being an indirect bandgap material, it needs a phonon to conserve momentum in the absorption of a photon [71]. Consequently the absorption coefficient of crystalline Si is low. Thin film solar cells help

in reducing the material cost associated with the low energy density of solar radiation [72]. Thin film solar cells, a few microns thick, have been fabricated using a-Si:H [73], GaAs [74], CdTe [75,76], $CuInSe_2$ [77] and organic semiconductors [78]. Thin film hydrogenated amorphous Si (a-Si:H) p-i-n junction based solar cells are comparatively easy to make, have elemental abundance and absorb more solar energy than thin film crystalline Si solar cells [79] of the same thickness. However, absorption in a-Si:H is poor especially in the near-infrared part of the solar spectrum. Various methods have been utilized to increase the absorption of solar radiation in these solar cells. Patterning or texturing the surface of the solar cell [80, 81] and adding plasmonic nanoparticle [82–84] or nanoholes [85] are some of the ways to increase light interaction with the thin solar cells.

This work is inspired by the simulation studies of light interaction with metallized pnc-Si membrane. An ultrathin freestanding metallized a-Si:H p-i-n junction is introduced as a solar cell. The metal film on both sides of the a-Si:H acts both as an electrical contact as well as cavity mirrors. The absorption of this solar cell can be tuned by changing the thickness of the a-Si:H p-i-n junction. Tuning will allow absorption wavelengths in the near-infrared spectrum of the solar radiation where the a-Si absorption is poor. This scheme shows promise in working with tandem solar cells [86, 87] in targeting specific wavelengths or as transparent solar cells, which is used on windows to generate solar electricity but allows visible light through [88].

1.5 Thesis Outline

The thesis is structured as follows. The fabrication of all the devices used in the thesis is remarkably similar and follows from the fabrication of the pnc-Si membranes. The fabrication and characterization of metallized pnc-Si membrane, slot structures in metallized pnc-Si membrane and a-Si:H p-i-n junction solar cells with metal contacts have been discussed in Chapter 2.

In Chapter 3, the interaction of light and the response of the sensing device both for an isolated single nanohole and for a size distribution of holes over an area of the metallized pnc-Si membrane are studied with the help of FDTD simulations. Experimental transmission measurements are performed to characterize the sensing performance of the device.

The slot effect in metallized pnc-Si is examined in Chapter 4. The slot effect is defined and the conceptual structure discussed. Three-dimensional FDTD simulation shows the creation of the slot effect in the low refractive part inside the nanohole. Various conditions are simulated to characterize the effect in the Al_2O_3 deposited metallized pnc-Si membranes.

Chapter 5 examines the photovoltaic effect on freestanding metallized a-Si:H p-i-n junctions. These structures are inspired by the simulation result obtained in metallized pnc-Si membranes and are made by replacing the a-Si layer in pnc-Si membrane with a-Si:H p-i-n junctions. FDTD simulations of absorptance show the associated optical mode of the structure. Experimental I-V curve and EQE measurements were obtained under AM 1.5 illumination. The correspondence between the absorptance simulations and EQE

measurements show that absorptance simulations provide a simple method to characterize and predict the photovoltaic performance of these ultrathin membranes.

Conclusions and outlook for future work are discussed in Chapter 6.

Chapter 2 Fabrication and Characterization

The first part of this chapter describes the fabrication and characterization of the porous nanocrystalline silicon (pnc-Si) membranes. The metallization of the pnc-Si membranes is then outlined to make a novel freestanding sensing platform in section 2.1. The fabrication and characterization of devices based on slot architecture and of freestanding, ultrathin, amorphous silicon-based photovoltaic membranes is outlined in section 2.2 and section 2.3 respectively.

2.1 Fabrication and Characterization of Metallized Pnc-Si Membrane Devices for Sensing

This section focuses on the fabrication and characterization of the devices used in this thesis. Fabrication and characterization of the ultrathin nanocrystalline Si porous membrane are first outlined. This structure acts as the basis for the sensing devices and the slot devices.

2.1.1 Fabrication of Pnc-Si Membranes

The porous nanocrystalline membranes were first discovered by Striemer et al. [1]. They can be made in various thicknesses ranging from <10 nm to >30 nm. The average pore diameters range from 5 nm to 80 nm and the porosities can range from 0.1% to > 15 %. The fabrication of these membranes is attractive because no precision lithography

tools like focused ion beam or electron beam lithography are needed to make nanoholes in the membrane. A distinctive feature that makes these membranes unique is that despite being only a few tens of nanometers thick, they are freestanding and can cover an area upto a few mm^2.

Standard semiconductor manufacturing processes are used in fabricating these membranes [89], The steps are outlined schematically in Figure 2.1.

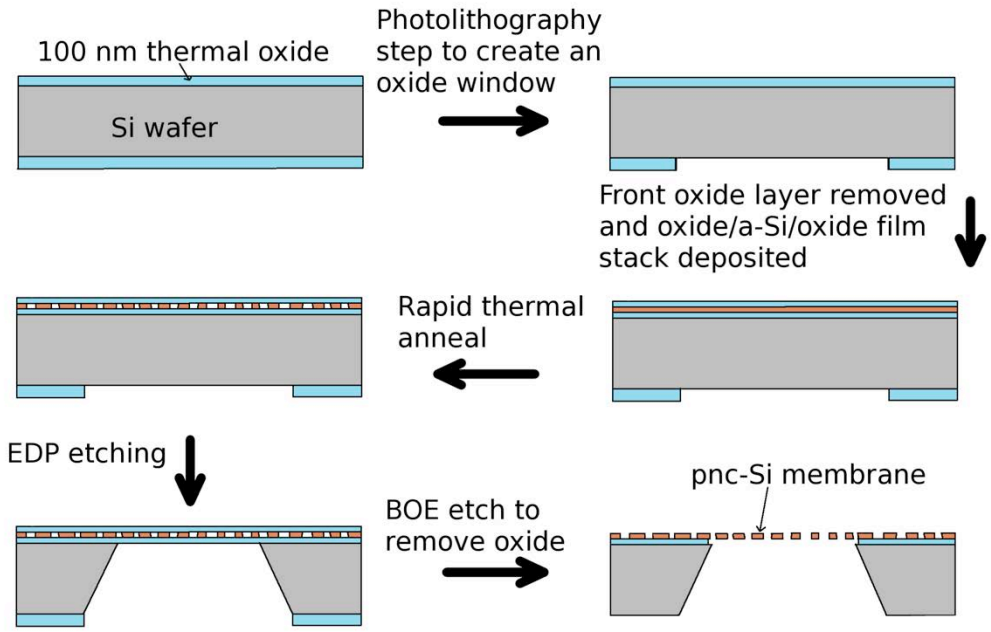

Figure 2.1: Schematic for fabrication process of the porous nanocrystalline silicon membrane

The starting material is a 4-inch diameter, 200 µm thick, < 100 > orientation double polished and n-type doped Si wafer. The silicon wafer is cleaned using standard RCA [90] clean process that removes organics, native oxides and metal contaminants. 100 nm of thermal oxide is grown on both sides of this wafer using a tube furnace. The backside of the oxidized wafer is then patterned using standard photolithography process.

Hexamethyldisilazane (HMDS) and a positive photoresist (Shipley 1813) are spun and baked on the backside of the oxidized wafer. This layer is then exposed to UV light through the patterned transparency mask and developed. The pattern in the SiO_2 layer on the backside and the front oxide layer are both removed using a 1:10 aqueous HF solution followed by the removal of the photoresist. The shape and size of this pattern determines the geometry of the freestanding membrane. In the next step, a high quality 3 layer film stack typically 20 nm of SiO_2, 15 nm of amorphous Si and 20 nm of SiO_2 is deposited using an AJA International ATC-2000-V RF magnetron sputtering tool. The thickness of the sandwiched amorphous Si layer determines the thickness of the membrane. In this study both 15 nm and 30 nm is used. This three-layer stack is then put into a rapid thermal processing (RTP) chamber. Here the temperature of the stack is raised to between 700 ˚C to 1100 ˚C in a few minutes, where it is kept for a minute and then allowed to cool down. This rapid rise in temperature causes the sandwiched amorphous Si layer to change its state to nanocrystalline silicon. As the nanocrystals begin to nucleate, voids are created in the film. This wafer is then put into a custom made etch cell, with its etched bottom side in contact with the highly selective Si etchant ethylenediamine pyrocatechol (EDP). EDP has a etch rate ratio of 5000:1 between Si and SiO_2. The SiO_2 layer acts as a stop layer for the etching process. This leaves a freestanding stack made of three film of oxide, porous Si membrane and oxide. In the final step, the protective oxide masks are removed using buffered oxide etchant (BOE). The BOE selectively etches away the SiO_2 layers to release the porous nanocrystalline silicon as a freestanding membrane. Those voids, which are spontaneously formed in the RTP process and are large enough to cover

the thickness of the membrane, open up as holes. The Si membrane is released as a freestanding membrane with holes of the order of nanometers in size. This freestanding membrane is supported by the un-etched Si substrate. Pnc–Si membranes of different shapes and geometries are shown in Figure 2.2.

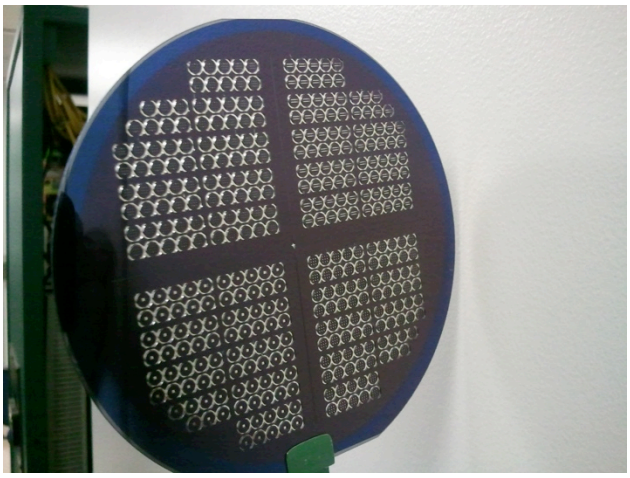

Figure 2.2: Images of pnc-Si membranes with different geometries on a silicon wafer.

The pore density and the geometry of the pores are dependent on a number of fabrication parameters. The most important of them are the annealing temperature and the silicon layer thickness. For an RTP annealing temperature ranging from 700 ˚C to 1000 ˚C, the average pore size ranges from 9.4 nm to 22.2 nm and the porosity ranges from 0.5 % to 6.6 %, respectively [3]. The pore size and porosity of the membranes increases significantly with an increase in the thickness of the Si layer.

2.1.2 Characterization of Pnc-Si Membranes

As seen in section 2.1.1, the nanohole pores are formed spontaneously during the RTP process resulting in a distribution of pore sizes. The shape of the pores also shows a wide variation. The most important parameters that describe the porous membranes are

porosity, pore size and pore shape. Since these membranes are ultrathin and freestanding, they can be characterized by transmission electron microscopy (TEM) to characterize these membranes.

In a transmission electron microscope, a beam of electrons is passed through an ultrathin specimen. As the de Broglie wavelength of the electron is much smaller than the wavelength of visible light, it is possible to form an image of the ultrathin specimen with a resolution in the order of angstroms. The TEM image of a freestanding pnc-Si membrane, supported by a substrate designed to fit in the sample holder of a Hitachi 7650 TEM is shown in Figure 2.3.

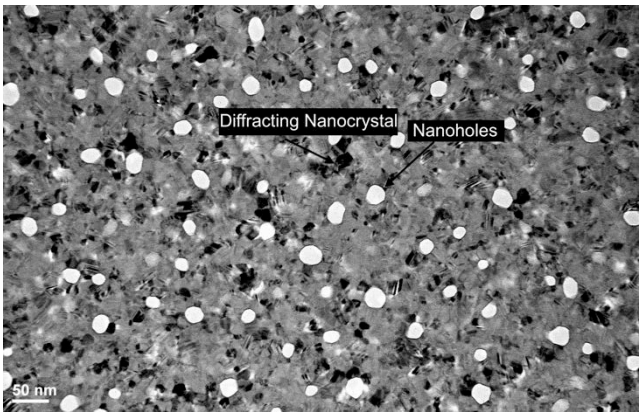

Figure 2.3: Transmission electron microscopic image of the porous nanocystalline Si membrane. The white spots show the nanoholes or pores. The darker regions denote the diffracted nanocrystalline structure, with the darkest regions satisfying Bragg's condition.

The image is taken in the bright field mode. The white, almost circular spots in the TEM images are the open pores through which electrons pass through collinearly without any interaction and hence are imaged as bright spots. Around these white spots, different areas are seen ranging in color from light gray to black. These are the nanocrystalline areas of the membrane. Since the nanocrystals are oriented with different Bragg planes,

the electrons are diffracted by variable amounts giving rise to different shades of gray color. The darkest areas indicate nanocrystal planes satisfying the Bragg condition [91].

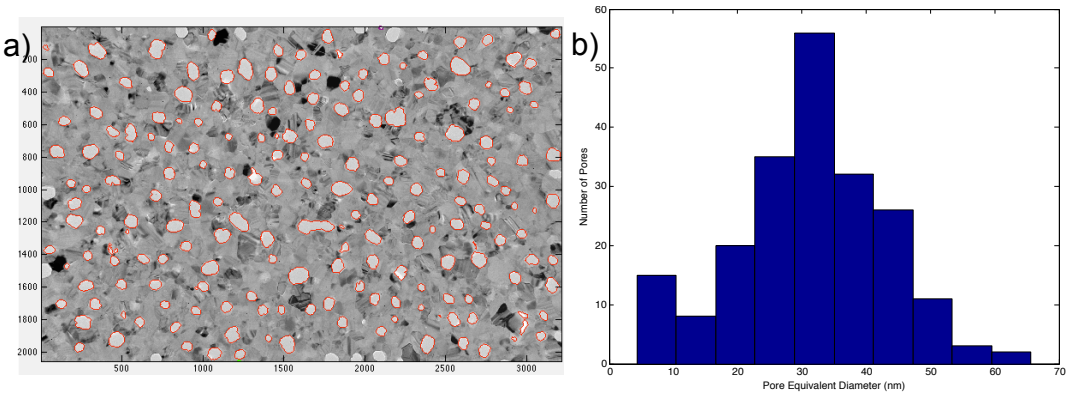

Figure 2.4: a) TEM image of the pnc-Si membrane with the pore outlined in red using MATLAB code. b) Histogram of the pore distribution obtained from the TEM image. The mean diameter of the pores for this membrane is 32.7 nm and the porosity is 10.7 %.

The bright field TEM images not only show the nanohole pores and the nanocrystals, but also help in characterizing the porous membrane properties. Using a custom image processing code written in MATLAB [available for download at nanomembranes.org/resources/software], it is possible to determine the porosity, size distribution and average size of the pores from this bright field TEM image.

Figure 2.4a shows the outline of the pores in red on a TEM image of the pnc-membrane processed using the software. Pores at the edges are not taken into account by the software. The pore distribution is also shown in a histogram in Figure 2.4b. The mean diameter of the pore distribution for this pnc-Si membrane is 32.7 nm. The porosity of the membrane, defined as the ratio of the open space of the pores to the whole area of the membrane expressed in percentage, is 10.7 %. The standard error for the porosity value

and average pore diameter for different locations of the same membrane is low, so statistics from any random location of the membrane can be assumed to represent values for the whole membrane [5].

2.1.3 Metallization of Pnc-Si Membranes

Metallization of the membranes has to fulfill two criteria. First, the metal film should not block the nanoholes or the unique porous property of these pnc-Si membranes would be lost. The second criterion is that the metal must form a continuous and smooth film. Electron beam evaporation is a physical vapor deposition process that satisfies the above criteria for the pnc-Si membranes.

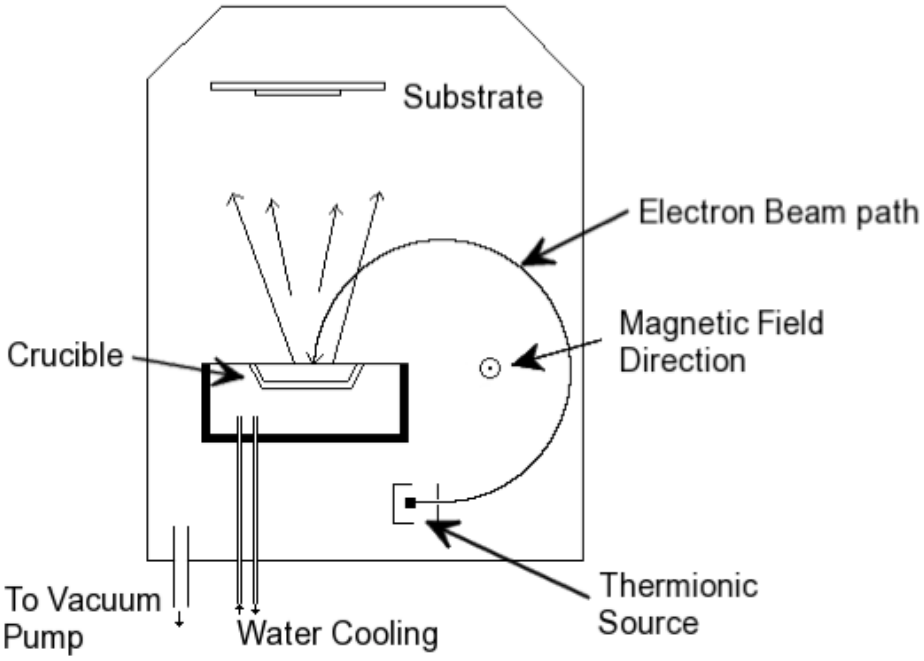

Figure 2.5: Schematic of an electron beam evaporator. The source is a tungsten filament that is heated with high current. The electron beam generated is accelerated using high voltage and

directed using a perpendicular magnetic field to the evaporation material, which acts like a cathode. The crucible is water-cooled and the whole system is kept under vacuum.

A CHA electron beam evaporator is used to deposit metal on the membranes. A schematic of the process tool is shown in Figure 2.5. This tool consists of a chamber that is kept at a base pressure of 10^{-6} to 10^{-7} torr during deposition. A tungsten wire filament acts as a cathode for generating electrons. A high current is passed through this filament causing thermionic emission of electrons. These electrons are then accelerated to high energies using an accelerating voltage. A magnetic field directs the beam to the evaporation material. This beam can be moved around to target the evaporation material. The evaporation material is kept in a crucible liner made up of electrically conductive graphite. The pocket around the crucible liner is grounded and kept in a water-cooled jacket. When the high-energy electrons hit the surface of the evaporation material they lose their kinetic energy rapidly. This causes the evaporation material to heat up and consequently melt or sublime. The substrate holder with the membranes is usually kept on top of the source at a distance of about 700 mm. The vapor from the evaporation material condenses on the substrate and the membrane to form a thin film. This is a line of sight deposition, so necessary care has to be taken to ensure that the membranes are not shadowed in the chamber.

Gold (Au) was deposited on the membranes. However, gold adhesion with silicon is poor so titanium (Ti) is used as an adhesion layer between gold and silicon. The evaporator tool has multiple pockets for multiple layer deposition of different materials.

Firstly; 3 nm of Ti is deposited and without breaking the vacuum, 10-15 nm of gold is then deposited on the membranes. During deposition of Ti, care was taken to ablate oxidized Ti from the surface before opening the shutter for deposition on the substrate. The deposition rate for Ti is 0.5-1 Å/s and that for Au is higher, 1-4 Å/s. A quartz crystal microbalance is used to measure the deposition rates and thickness of the film. The deposition is repeated on both sides of the structure to get a metal insulator metal structure. A different type of geometry is also investigated to enhance the sensing properties of this metallized membrane. This is discussed in Chapter 3.

2.1.4 Characterization of Metallized Pnc-Si Membranes

The continuity and smoothness of the deposited metal films on the pnc-Si membranes are important in making the sensors. Scanning electron microscope (SEM) is a convenient and fast tool in characterizing the metallized films. In this method, a

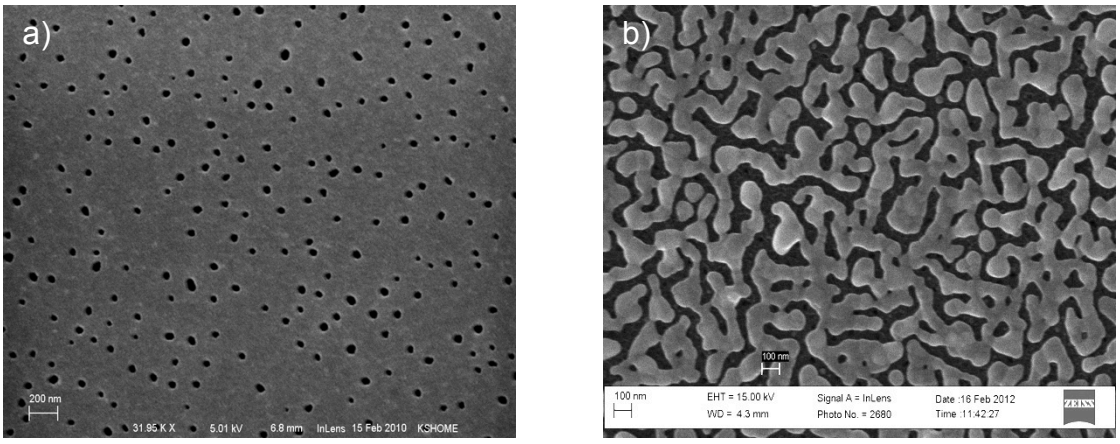

Figure 2.6: a) Scanning electron microscope (SEM) image of a metallized porous nanocrystalline membrane. The nanoholes are shown as black circular holes. The surface of the metallized membrane is continuous. b) SEM image of a metallized membrane where the metal deposition was not continuous leading to island formation. In this case the oxidized Ti layer was not ablated and this resulted in poor adhesion between Au and Si leading to island formation.

sample is scanned with a beam of electrons to form an image. It is possible to get a cross-sectional view of the membrane to measure the thickness and determine the continuity of the metal film.

Figure 2.6 a) shows an SEM image of a metallized membrane. Here the metal is continuous and the holes are seen as dark spots. Figure 2.6 b) shows the SEM of a metallized membrane where the metal is not continuous. Here the oxidized Ti layer was not ablated; this resulted in poor adhesion between Au and Si leading to island formation. From the SEM images, the difference between a continuous metal film and island film growth after metal deposition is clear. This provides a fast and convenient method in characterizing the deposition process.

To image the cross-section of the metallized membrane, the following method is used. The membranes on the Si substrate are kept face down on the polished surface of a Si wafer. A drop of isopropyl alcohol is put on the back. As this liquid evaporates, the membrane attaches itself onto the Si wafer surface. The Si wafer is then cleaved to get a cut through the attached membrane.

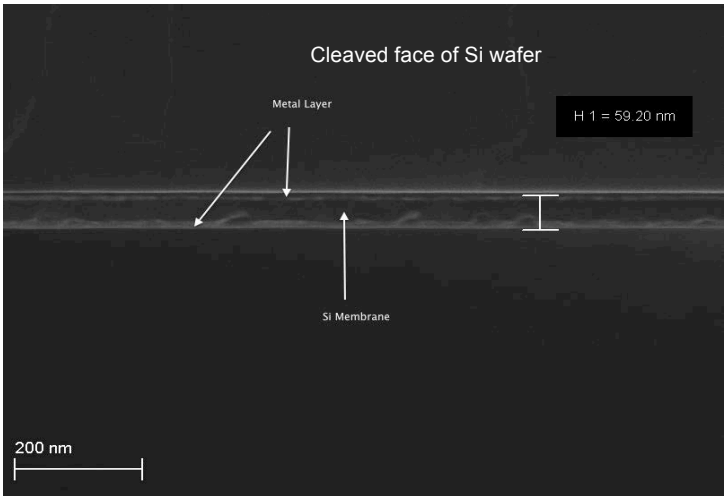

Figure 2.7: SEM image of a metallized pnc-Si membrane showing the cross-sectional view of the membrane. The pnc-Si membrane is 30 nm in thickness; the deposited metal layer on each side is 15 nm in thickness. The cleaved edge of the Si wafer is seen on the top of the membrane.

This piece of Si with the attached membrane is kept perpendicular to the electron beam to get a cross-sectional image of the membrane. Figure 2.7 shows the SEM image of the cross-section. The deposited metal films can be seen on both side of the 30 nm thick pnc-Si membrane. The total thickness of the deposited metal was 15 nm on each side. The cleaved Si wafer edge can be seen on top of the membrane.

The smoothness of the metallized film is characterized using an NT-MDT atomic force microscope (AFM). AFM was developed in 1986 and is a derivative of the scanning tunneling microscope (STM) [6,7]. An AFM consists of a sharp silicon tip at the end of a cantilever. The size of the tip is of the order of nanometers. When this tip is brought near the surface, the various interaction forces between the surface and tip bends the cantilever. A laser spot is reflected off the cantilever to a detector. As the cantilever

bends, the spot moves and the detector records the movement. As the tip scans across the surface, an image is formed with a resolution of less than a nanometer.

Surface roughness and features can be measured with high accuracy using the AFM.

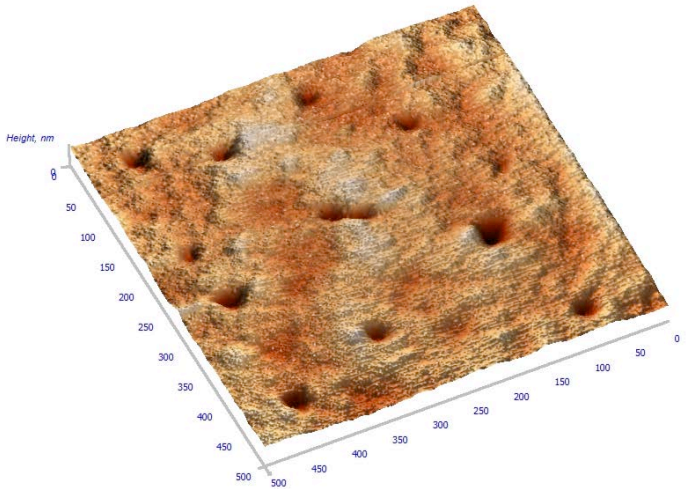

Figure 2.8: AFM image of a freestanding metallized pnc-Si membrane. The surface roughness is 0.3 nm. The metal layer is smooth and the holes can be clearly seen to be open.

The AFM image of Figure 2.8 shows the surface of a freestanding metallized pnc-Si membrane. The rms roughness of the surface measured from this image is 0.3 nm, that is of the same order as that of the deposited a-Si layer in the membrane fabrication process [6]. The AFM image shows that the metal deposition step creates a smooth continuous film and does not block the nanoholes in the pnc-Si membrane.

2.2 Fabrication and Characterization of Slot based Pnc-Si Membranes

The slot architecture is based on the metallized freestanding pnc-Si membranes. The metallization of the membranes is done on a different tool, a PVD-75 Kurt J. Lesker evaporator/sputter tool. The challenges associated with depositing metal on this tool are

outlined. Atomic layer deposition technique is used for the conformal growth of a dielectric inside the nanoholes. The following subsections describe the fabrication and characterization of such a device.

2.2.1 Metallization of the Pnc-Si Membranes for Slot Devices

The metallization achieved in the CHA-ebeam evaporator leads to a continuous and smooth film. However, the processing time of the tool was large. The Kurt J. Lesker PVD-75 evaporator/sputter turn-over time was only 2 hours and the easy accessibility made it a good candidate for metal deposition.

3 nm of Ti and 15 nm of Au was deposited on a 15 nm thick pnc-Si membrane. The initial base pressure before deposition is kept at 2.1e-6 Torr. The rates of depositions are 0.2-0.3 Å/s and 0.3-0.4 Å/s for Ti and Au respectively. SEM image of the deposited membrane is shown in Figure 2.9.

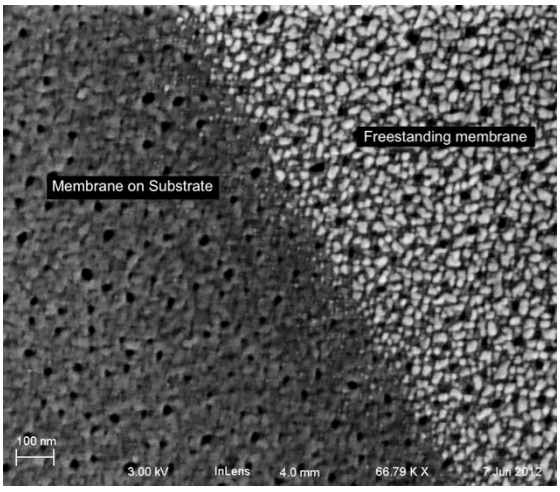

Figure 2.9 SEM image of metallized membrane at the interface between freestanding part of the membrane and the substrate supported part. The metal film is continuous over the substrate while the metal film is broken up over the freestanding part.

The SEM image shows that the metal film over the freestanding part of the membrane is not continuous and broken into pieces. The membrane supported over the substrate is continuous and similar to the one seen in the CHA ebeam evaporator. There can be two probable causes for this type of breakup in the continuous film over the freestanding membrane. Firstly, mechanical vibrations over the freestanding film during deposition breaks the metal film up. Secondly, the distance between the source metal and the membranes being smaller (when compared with the RIT CHA ebeam evaporator), the metal adatoms carry enough energy to move about and coalesce when they reach the freestanding membrane. The substrate being thicker can dissipate this energy faster and make a continuous film. To test out the probable cause, pnc-Si membranes were placed at about 10˚ over the deposition plate, seen as 'angled' in Figure 2.10. This was done, to change the kinetic energy of the atoms hitting the freestanding membrane at an angle. To test out the second hypothesis, the membranes were kept in an orientation such that they were at different distances from the center of the platen but were perpendicular to the direction of deposition. This is seen as 'perpendicular' in Figure 2.10.

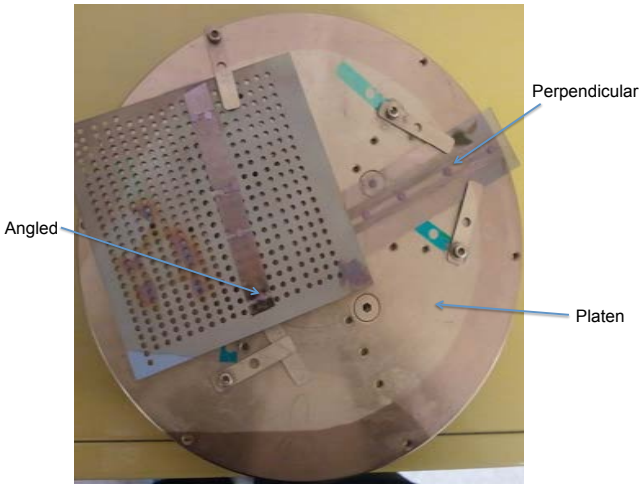

Figure 2.10: Position of the ‘angled’ and ‘perpendicular’ membranes on the platen. The ‘angled’ samples are kept at 10˚ with respect to the surface of the platen. The ‘perpendicular’ samples lie perpendicular to the direction of deposition.

SEM images are taken of the angled samples and the perpendicular samples as shown in Figure 2.11. The angled sample is the one nearer the middle of the platen. The perpendicular sample membrane is the one at the edge of the platen, shown with arrows in Figure 2.10.

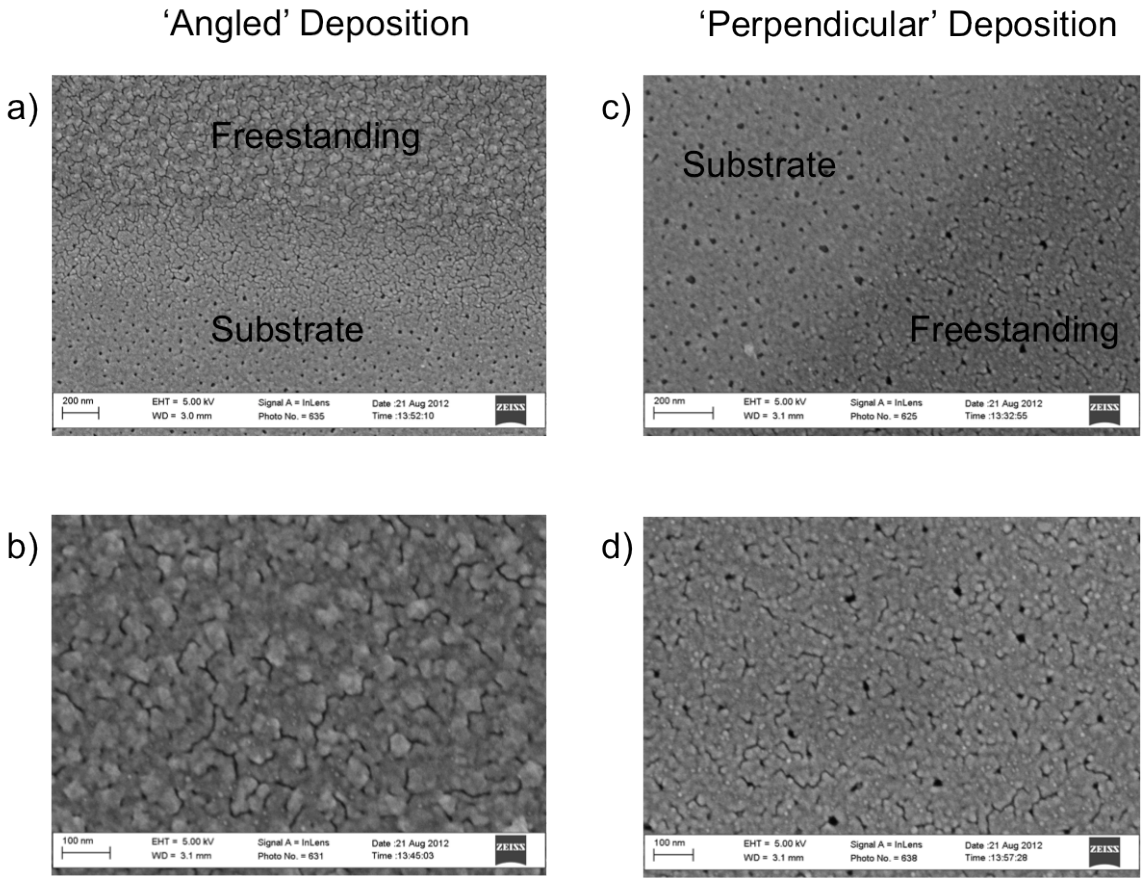

Figure 2.11: a) and b) show the SEM images of 'angled' metallized pnc-Si membrane. a) Shows the interface between the freestanding and substrate supported part of the membrane. b) Shows the SEM over the freestanding membrane. The images show that metal film is discontinuous and blocks up the nanoholes for 'angled' deposition. c) and d) Shows the SEM images of 'perpendicular' deposited metallized pnc-Si membrane with c) showing the interface. d) Shows the SEM image over the freestanding membrane. Although the metal film is not as continuous as previously seen using the CHA ebeam evaporator, the holes are not blocked.

Figure 2.11 shows that keeping the membranes at an angle does not help in depositing a continuous film over the membrane. Increasing the distance between the membranes and the evaporating source material does help in making the film smoother and does not lead to deposits over the nanoholes. However, the metal film still does not have the film

quality seen using the CHA ebeam evaporator. A TEM image of the metallized membrane further shows the open nature of the holes and the discontinuity in the metal, as seen in Figure 2.12.

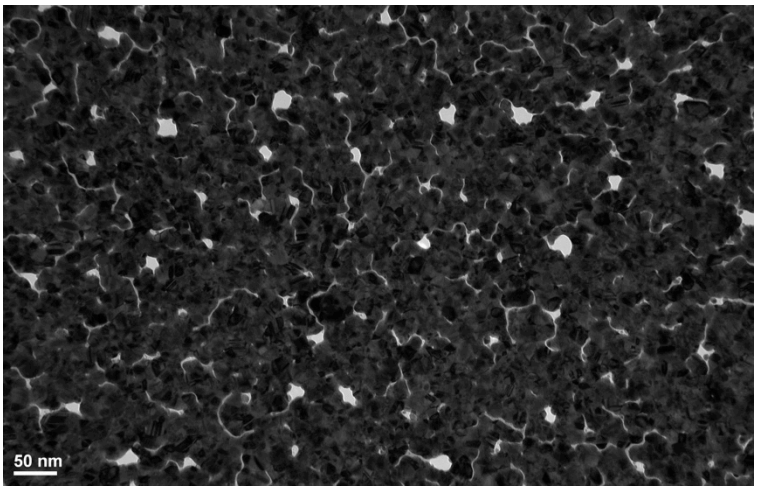

Figure 2.12: TEM image of the metallized membrane showing the open nanoholes and the cracks in the metal film.

From the TEM image, it is seen that although the metal is not totally continuous, the nanoholes are open and this metallized membrane is suitable for the atomic layer deposition process for depositing Al_2O_3.

2.2.2 Atomic Layer Deposition (ALD) Process

Atomic layer deposition is a chemical vapor thin film growth technique, discovered in the late 1970's by Suntola et al. [94]. The pair of chemicals used in growing the films is called precursors. The growth of the film is a cyclic process. In each cycle, a single monolayer of material is deposited. Each cycle consists of four basic steps as follows. First, the saturated vapor of the precursor is introduced into the chamber; this reacts with the surface to create an intermediary compound. In the next step, a purge step makes sure

that excess precursor is removed from the chamber environment. This is done by evacuating the chamber to a low pressure and using a purging gas like Argon. Then the second precursor is introduced to react with the first intermediary compound already present on the surface of the substrate. The final step consists of removing the excess products of the reaction and the second precursor. This creates a monolayer of the material being deposited. The thickness of one cycle can be 0.1 Å to 3 Å [95]. The cycle is repeated to create films of the desired thickness. This process gives very precise control over the thickness of the film being deposited. As the deposition is based on saturated vapor deposition process, the film is extremely conformal.

The freestanding ultrathin pnc-Si membranes have a higher gas permeance than any other membrane [8]. ALD deposition of Al_2O_3 has been shown to shift the pore size histograms by conformally covering the holes and thereby decreasing their size [96]. Here, we use the ALD process to deposit Al_2O_3 conformally on the metallized membrane to create an air slot inside the nanohole. Precise control of the film thickness and conformal depositions are both satisfied by ALD. The outline of the process is shown in Figure 2.13.

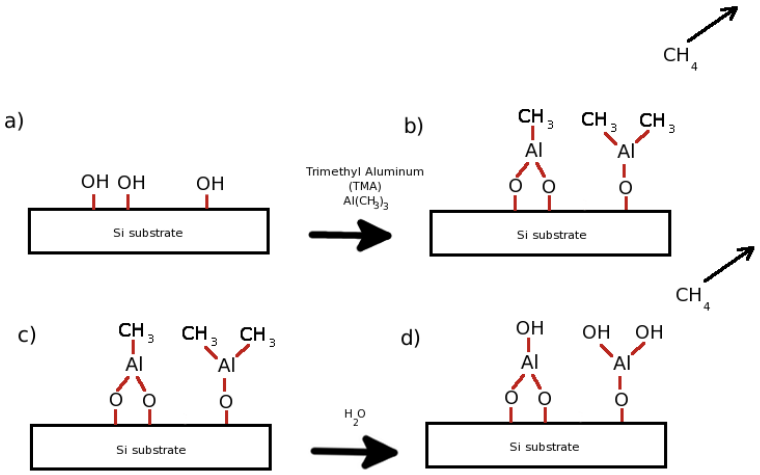

Figure 2.13: Steps outlining the ALD deposition of Al_2O_3 on a Si substrate. a) The Si surface is hydroxylated by water vapor. b-c) Trimethyl Aluminum is introduced as a pulse; this reacts with the surface hydroxyl groups. The unreacted precursor and reaction products are expunged from the chamber. d) Water is pulsed; it reacts with the intermediary compound on the surface to form hydroxylated aluminum oxide. The byproduct of this reaction, methane and excess precursors are again expunged from the reaction chamber. This cycle is repeated to grow multiple layers of Al_2O_3.

The deposition is performed in Cambridge NanoTech Savannah S200 system (Cambridge, MA). Individual chips were loaded into the chamber. In one configuration, they are set in between the edges of two glass slides to maintain the uniform flow of gases on the top and bottom of the freestanding membranes. The pressure change is enough to blow these chips in the membrane. So two other glass slides are placed on top of the membranes to sandwich them and hold in them place. The membranes and glass slides are oriented such that they do not impede the gas flow inside the chamber. The films are of better quality at higher temperature. The chamber is heated to 250˚C and pumped to a base pressure of 10mTorr to evacuate the excess products. 20 sccm of argon is introduced continuously in the chamber to help expunging the unreacted precursors and

reactant products. The precursor pulses of water and trimethyl aluminum are 50 milliseconds long with a 5 second pause between the pulses to help in purging the products. 1.1 Å of material is deposited after each cycle.

The metallized membranes have pores of different sizes, with an average diameter of ~30 nm. So by depositing a 10 nm layer or 91 cycles of Al_2O_3, an average air slot diameter of 10 nm is created provided the deposition inside the holes is conformal and at the same rate. It is important to note that the hydrophobicity/hydrophilicity of the Si surface and the Au surface is different [97]. The hydrophobicity/hydrophilicity of Au depends on the impurities present in it. Pure Au is hydrophilic. Carbon contamination renders it hydrophobic [98]. As has been seen for ALD deposition, a hydrophilic surface is necessary to form the hydroxyl groups on the surface. The deposition rate and profile on Au and Si surface of the metallized membrane may be different.

2.2.3 Characterization of Slot Metallized Membranes

ALD deposition at 250˚C results in agglomeration of the metal film to form isolated metal films. This is a thermally activated process [99]. There are various models describing this agglomeration process [100–103]. An SEM image of the interface between the freestanding and substrate supported metallized membrane after the ALD deposition of Al_2O_3 is seen in Figure 2.14. The image shows that the metal film gets agglomerated to form metal islands. The conformally deposited Al_2O_3 around the metal islands can be seen as a change in contrast around the metal islands.

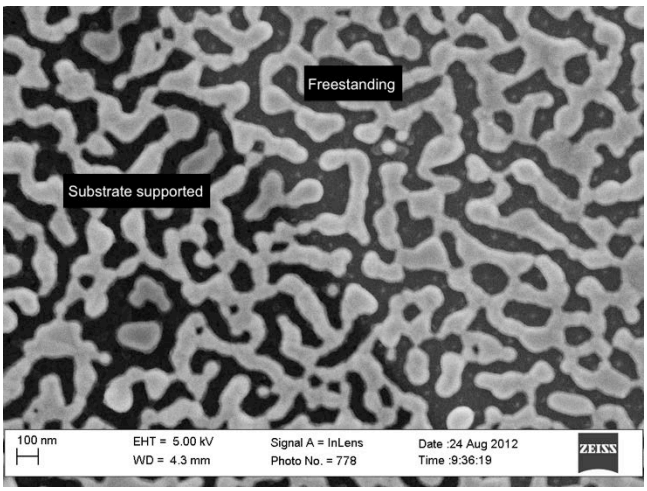

Figure 2.14: SEM image of the interface between the freestanding and substrate supported metallized membrane after the ALD deposition of Al_2O_3 at 250˚C. The image shows the agglomeration of the metal at 250˚C to form metal islands. The conformally deposited Al_2O_3 layer surrounding the metal is also seen.

TEM image of such an ALD deposited metallized pnc-Si membrane is also taken, shown in Figure 2.15.

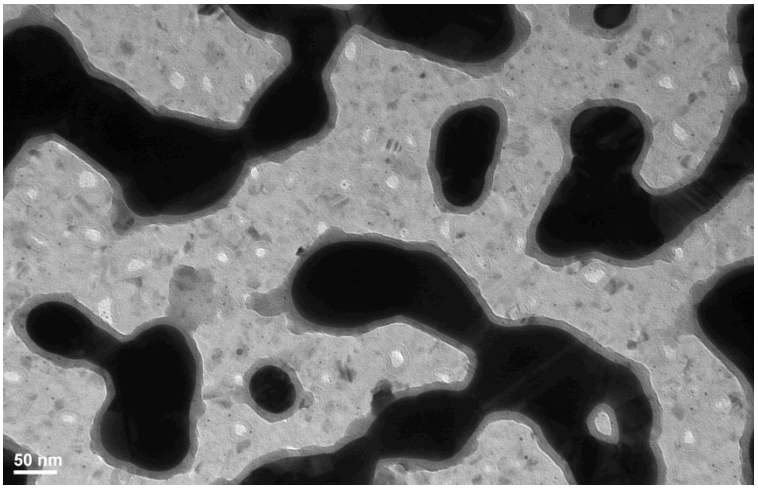

Figure 2.15: TEM image of the metallized membrane after the ALD deposition of Al_2O_3 at 250˚C. The image shows the metal islands in dark after the agglomeration of the metal film. Conformal deposition of Al_2O_3 is also seen around the metal and also around the nanoholes in the pnc-Si membrane.

The TEM image shows the metal islands in dark and the pnc-Si membrane with its characteristic nanocrystals and nanoholes. Al_2O_3 deposition around the metal islands and nanoholes can also be seen. 250˚C for the deposition of Al_2O_3 is too high for the integrity of the metal film over and near the freestanding membrane.

Much further away from the freestanding part of the membrane over the substrate, the metal film does not form islands after the ALD process. It remains as a continuous metal film. The Al_2O_3 is deposited conformally around the hole. This can be seen in the SEM image of the ALD deposited metallized membrane shown in Figure 2.16. The image is taken over the substrate part of the membrane much further away from the freestanding part.

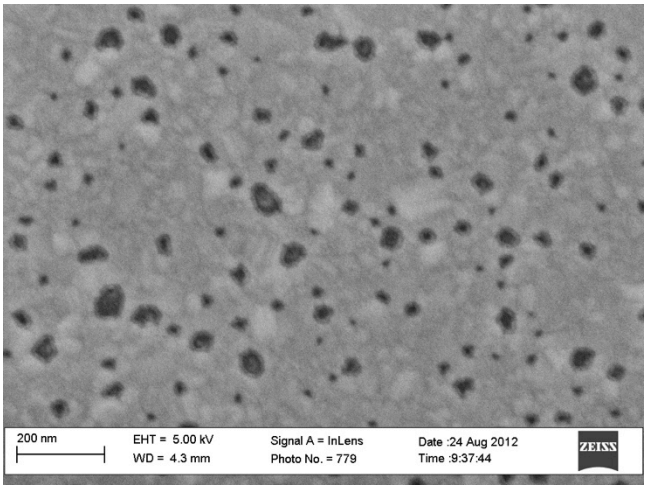

Figure 2.16: SEM image of the metallized membrane after the ALD deposition of Al_2O_3 at 250˚C, taken over the substrate much further away from the freestanding part of the membrane. The metal film does not agglomerate and the ALD deposition leads to conformal growth of Al_2O_3 around the holes as seen by the contrast surrounding the holes.

This shows that the deposited metal film quality over the substrate is good enough to withstand the 250˚C temperature of the ALD deposition.

The Al_2O_3 film quality is higher at 250˚C, but because of the agglomeration of the metal film, a 100˚C temperature recipe was used to deposit Al_2O_3 using the ALD process.

The SEM picture of the metallized membrane after the Al_2O_3 deposition is shown in Figure 2.17. The SEM image shows the freestanding part of the ALD deposited metallized pnc-Si membrane. The change in contrast indicates conformal growth of the Al_2O_3 layer. However, it is important to note that Al_2O_3 being an insulator, it is difficult to image such a membrane because of charging effects.

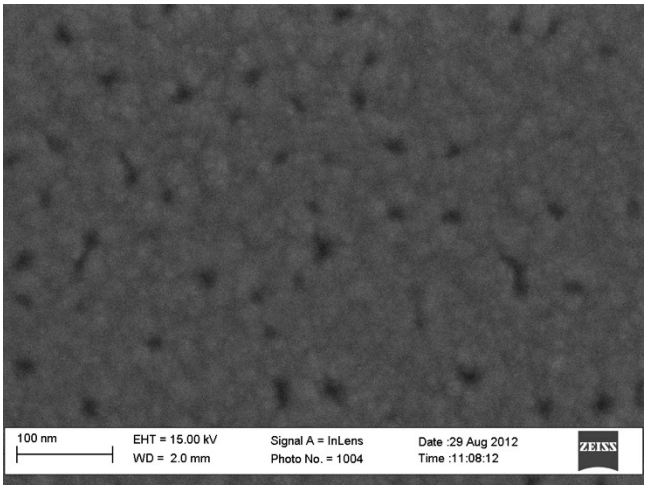

Figure 2.17: SEM image over the freestanding membrane of a metallized pnc-Si membrane after deposition of Al_2O_3 using ALD process at 100 ˚C. The image shows a difference in contrast around the holes indicating the conformal growth of Al_2O_3.

A TEM image of the ALD deposited metallized membrane is shown in Figure 2.18.

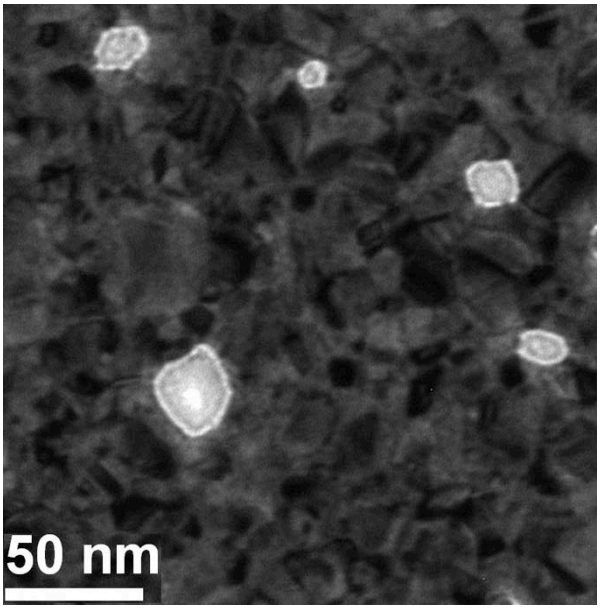

Figure 2.18: TEM image of the metallized membrane after the ALD deposition of Al_2O_3 at 100˚C. The image shows the Al_2O_3 layer deposited conformally around the biggest nanohole leaving a slot in the middle. The Al_2O_3 covers the smaller nanoholes completely.

The TEM image shows the conformally deposited Al_2O_3 layer surrounding the nanohole. The thickness of the starting pnc-Si membrane is 15 nm. The thickness of the Ti and Au films is 3 nm and 15 nm respectively. The temperature during the ALD deposition is kept at 100˚C and 91 cycles gave a thickness of around 10 nm of conformal Al_2O_3.

2.3 Fabrication and Characterization of Freestanding a-Si:H Membrane Solar Cells

In this section, a novel freestanding amorphous silicon solar cell is described. The fabrication of the solar cell is inspired from the pnc-Si membrane fabrication. The fabrication process is similar, and involves depositing a p-i-n a-Si:H junction using a plasma enhanced chemical vapor deposition tool. The advantage of using this type of

freestanding solar cell is twofold. One, it has two surfaces the back and front which can be coated with materials to act as electrical contacts and help in optical confinement. Second, this type of fabrication allows deposition of MOS fabrication incompatible materials.

2.3.1 Fabrication of a-Si:H Solar Cells

The fabrication of the freestanding a-Si:H solar cells is similar to the fabrication of the pnc-Si membranes. The major differences are the deposition of an a-Si:H p-i-n junction film instead of the a-Si film. The rapid thermal anneal process is also absent. The steps of the fabrication are outlined below in Figure 2.19. First, a thermal oxide layer 100 nm thick is grown on a 200 μm thick double-sided polished 5-10 Ω-cm n-type <100> Si wafer. The backside of this wafer is patterned to open a 2 x 2 mm window using contact lithography followed by buffered oxide etch (BOE). The front 100 nm oxide is also stripped off by this BOE etching step. 45 nm of oxide is then deposited on the front side of the wafer using GSI plasma enhanced chemical vapor deposition (PECVD) tool. This oxide acts as a stop layer during the Si etching step. A hydrogenated amorphous Si p-i-n type junction (a-Si:H p-i-n) is then deposited over the deposited oxide using the GSI PECVD. The n layer is deposited first so that it is closer to the back contact of the solar cell. The power during the deposition is kept at 50 watts. The thickness of the p-i-n junction is dependent on the time of deposition. In a typical case, deposition times of 13, 25 and 9 seconds gives corresponding thicknesses of 20, 25 and 15 nm for the n, i and p layers respectively. The n-doped film is kept at the bottom of the stack, closest to the

back contact as in the a-Si:H film, as the n-doped film absorbs more light compared with the p doped film.

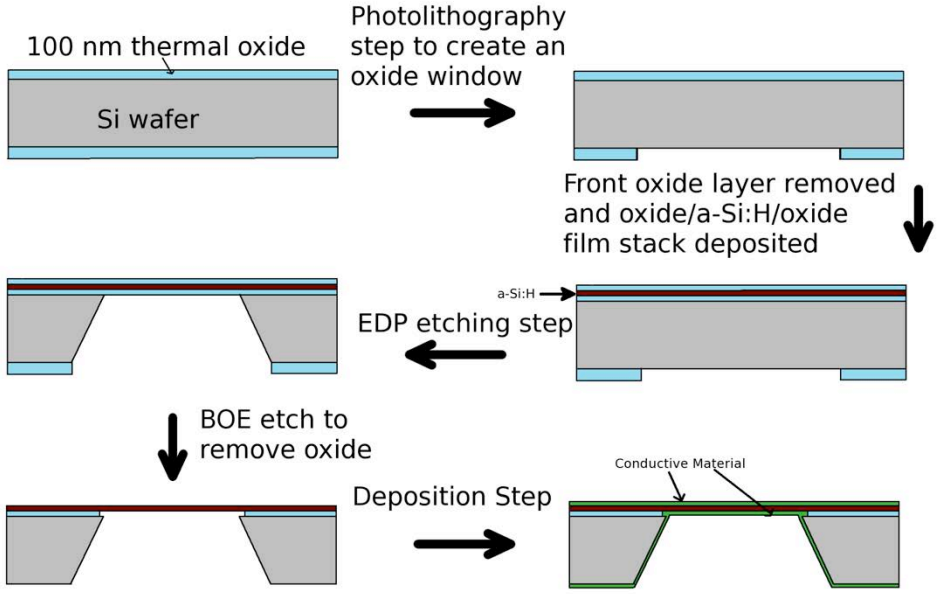

Figure 2.19: Steps outlining the fabrication of the freestanding a-Si:H solar cell

The last step involves making the electrical contacts. The most common geometry involved depositing Ag metal on both sides of the membrane. The deposition is similar to the metal deposition of the pnc-Si membranes shown in section 2.1.3, except that no adhesion layer is deposited there. The deposition in the electron beam evaporator was typically performed at a base pressure of 1.9e-7 Torr at an accelerating voltage of 10 kV and at rates of 0.3-0.5 Å/s. The minimum thickness deposited on any side of the PV membrane is 25 nm. It is important to maintain a continuous metal film to have a good electrical contact. The SEM shows that 25 nm of Ag deposition is enough to get a continuous metal film as seen in Figure 2.20

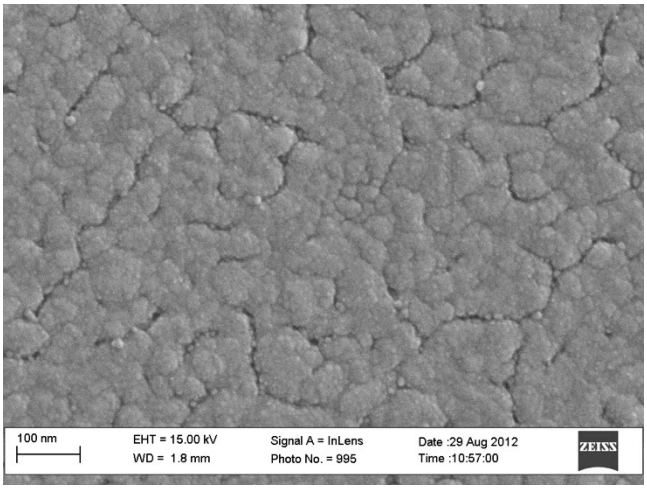

Figure 2.20: SEM image of the 20 nm thick Ag film deposited over the freestanding PV membrane. The film is continuous over the membrane and should provide good electrical contact.

The SEM image shows that the deposited Ag film is continuous and therefore should maintain good electrical and optical properties.

2.4 Conclusion

In conclusion, this chapter describes the processes involving the fabrication and characterization of metallized pnc-Si membranes, ALD deposited slot metallized membranes and metallized ultrathin freestanding a-Si:H solar cells. The common platform in all the three devices is the fabrication of ultrathin freestanding membranes. The fabrication is MOS compatible and hence follows standard fabrication techniques and can be scaled up. The characterization process involves using standard tools like SEM, AFM and TEM. The characterization process confirms the structure of the various devices and gives starting values for simulation models used later to describe the results.

Chapter 3 Nanohole and Sensing

In this chapter, the interaction of light with the metallized membrane is studied and the sensing property of such a structure is investigated. In section 3.1 there is a general discussion about how light interacts with small holes in metals when the radius of the hole is much smaller than the wavelength of light. The fabrication and characterization of the membranes are described in section 3.2. Finite-difference time-domain (FDTD) simulations are used to study the interaction of light with the structures and understand the relevance of membranes towards sensing in section 3.3. Section 3.4 details the experimental results and their understanding using simulation.

3.1 Background

In this section, surface plasmon resonance (SPR) sensors are introduced. Different sensors using SPR are outlined. A background review of the interaction of light with single nanohole as well as an array of nanholes is outlined.

3.1.1 Surface Plasmon Resonance Sensors

Surface plasmons are collective oscillations of the electron density at a metal-dielectric interface. The resonance conditions associated with these surface plasmons are sensitive to the local environment making it possible to develop refractive index sensors. For the photons to transfer energy to the metal electrons, both the energy and the momentum need to be conserved. When these conditions of coupling between the photons and electrons are satisfied, the resulting propagating electromagnetic wave at the interface is called the surface plasmon polariton (SPP). The SPP wave is a TM polarized

wave with the electric field perpendicular to the direction of propagation of the wave and also to the plane of the interface. The propagation constant for a SPP for a semi-infinite metal dielectric interface is given by

$$\beta = k\sqrt{\frac{\varepsilon_m n_s^2}{\varepsilon_m + n_s^2}} \quad (1)$$

where k is the free space magnitude of the wave vector, ε_m is the complex dielectric constant of metal and n_s is the refractive index of the dielectric [104]. The effective wavelength of the SPP is significantly shorter than the wavelength of the incident field. The most common of approaches to satisfy the above conditions of coupling light are the Kretchmann [105] configuration and grating couplers [106]. In the Kretchmann configuration, a prism is used to couple in light, using total internal reflection, into the metal film on one of the sides of the face of the prism. The resonance condition of coupling, seen as a reflection minimum, is very sensitive to the change in dielectric surrounding the metal film. It is monitored as a function of either the angle or the wavelength [104]. In grating couplers, as the name suggests, there is a periodic corrugation at the metal dielectric interface, when light falling on this grating is diffracted. When the total component of momentum of a diffracted order along the interface equals the momentum of the SPP, the photons transfer energy to the SPP. The coupling resonance condition being sensitive on the dielectric surrounding the grating, the monitoring aspects are similar to the Kretchmann condition. The highest bulk sensitivity of a SPR based attenuated total reflection optical prism based sensor is 8000 nm per refractive index unit (RIU) [107]. In grating based SPR sensors a sensitivity of

1000 nm/RIU has been obtained [108]. Although these configurations have high sensitivity, they do have certain drawbacks. Since both of these approaches work in the reflection mode, the optical infrastructure associated with it increases the footprint of the device. Multiplex sensing is of primary importance in many SPR sensing applications [109,110] and in the above configurations, it is difficult to incorporate flow-through microfluidics.

3.1.2 Light Interaction with Nanoholes

The interaction of light with a hole of radius much smaller than the wavelength of the incident light was first studied theoretically by Bethe [29] and later extended by Bouwkamp [30] and Cohn [111]. For an infinitesimally thin perfect metal conductor, the transmission $T(\lambda)$ was found to be proportional as $(\lambda/r)^4$, where λ is the wavelength of incident light and *r* is the radius of the hole, as shown in Figure 3.1.

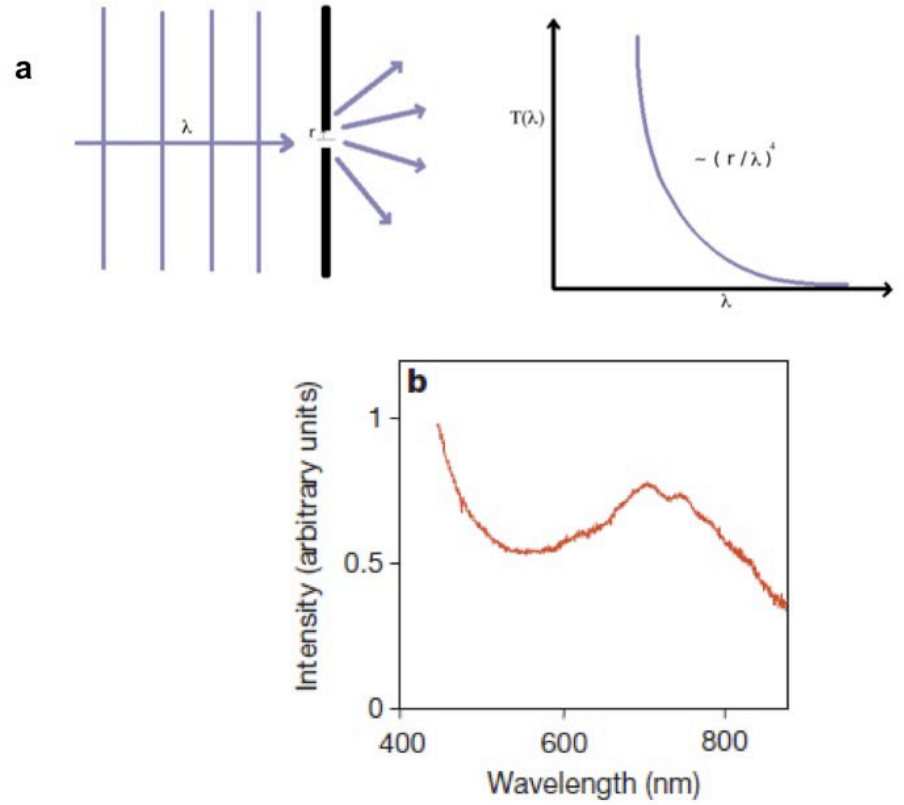

Figure 3.1: (a) Calculated transmission from a hole in an infinitesimally thin perfect metal sheet. The transmission from the hole, whose radius is much smaller than the wavelength of light, falls as $(\lambda/r)^4$. (b) In the case of a nanohole in a real metal, there is a peak superimposed over the $(\lambda/r)^4$ transmission curve. [Reprinted by permission from Macmillan Publishers Ltd: Nature [112], copyright (2007)]

So the transmission is very low as λ becomes longer than the radius of the hole. Ebbesen found that the transmission through a single hole in Ag metal film has an unexpected resonance peak superimposed on a smooth background [112]. This transmission peak indicates the presence of surface plasmon resonance.

In another study, Rindzevicius et al. [113] found that for a nanohole in an optically thin metal film, localized surface plasmons (LSP) are generated at the edge of the nanoholes, resembling dipole radiation. These LSPs then couple into the SPPs, seen in the near-field scanning microscope image shown in Figure 3.2 . The LSP-SPP coupling plays an important role in the way light interacts with these nanoholes. The thickness of the Au metal film in this case is 20 nm and the hole diameter is 60 nm.

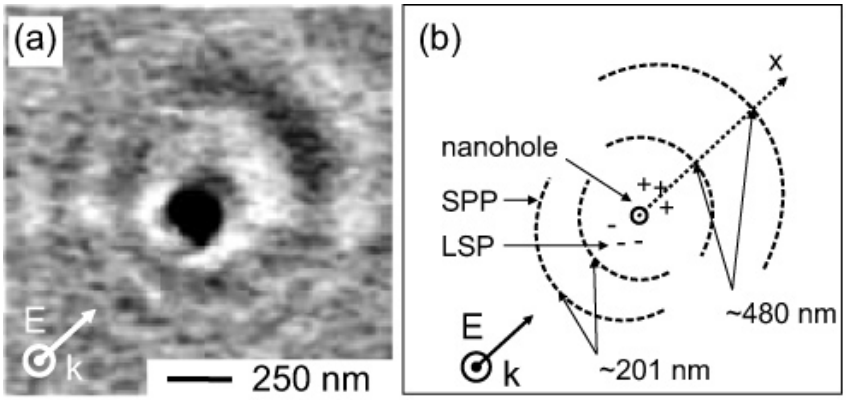

Figure 3.2: (a) Near-field scanning microscope image of light interacting with a nanohole 60 nm in diameter in a 20 nm thick Au film on a glass substrate. The electric field of the incident light is shown and the dipole like LSP generation is parallel across the direction of the electric field. [Reprinted (adapted) with permission from [113]. Copyright (2007) American Chemical Society.]

3.1.3 Nanohole Arrays

A newer configuration for sensing uses ordered nanohole arrays [114]. Nanohole arrays show enhanced transmission through sub-wavelength holes in a metallic film. This enhanced optical transmission is attributed to surface plasmon polariton waves [31]. The condition for coupling light in the structure follows from equation 1 and for a square array of nanoholes, the transmission resonance maximum is given by

$$\lambda_{SP}(i,j) = \sqrt{\frac{\varepsilon_m n_s^2}{\varepsilon_m + n_s^2}} \frac{P}{\sqrt{i^2+j^2}},$$

where P is the periodicity of the nanohole array, i and j are the order of the Bragg resonance, ε_m is the complex dielectric constant of metal and n_s is the refractive index of the dielectric [115]. Nanohole array sensors can use high numerical aperture optics, perform collinear detection, multiplexing and hence achieve smaller device footprint and integration. Recently, flow through sensing using a nanohole array has been demonstrated [116]. The general disadvantage of nanohole arrays is the need for expensive fabrication. To manufacture periodic nanohole arrays, focused ion beam or electron beam lithography is needed. Unordered nanohole patterns and isolated single holes have recently been used as SPR sensors [117–119]. Typically, they have been manufactured using colloidal lithography rather than expensive electron beam lithography or focused ion beam lithography. However, these devices need to be supported by a glass substrate and do not allow flow through sensing configuration. More recently, a flow through sensor with unordered nanoholes has been demonstrated by Jonseson et al. [27], but the fabrication is a multistep process involving colloidal lithography and RIE etching.

The highest sensitivity of 1022 nm/RIU in nanohole arrays have been demonstrated by using 200 nm diameter holes in a 200 nm Au film and using a parallel and orthogonal polarizer-analyzer pair [114]. For unordered short range holes a bulk sensitivity of 110 nm/RIU has been demonstrated with 110 nm diameter holes in 20 nm thick Au film [117]. For a flow-through system, a bulk sensitivity of 630 nm/RIU has been

demonstrated for a 220 nm diameter hole with a 600 nm periodicity in a 125 nm thick Au metal film suspended over a SiN membrane 50 nm thick.

3.2 Materials and Methods

The fabrication and characterization of the metallized porous nanocrystalline membranes have been outlined in section 2.1. The structure proposed here resembles unordered nanoholes in metal films and does not require any precision lithography. The cross-sectional thickness of our structures is one order of magnitude smaller than the conventional nanohole arrays and their area can stretch to the order of mm^2, which is much larger than conventional nanohole arrays. Figure 3.3 shows a typical structure. A freestanding ultra-thin porous Si nano crystalline membrane is coated with Au on both sides of the membrane. Essentially this is a freestanding porous gold membrane supported by a porous Si membrane.

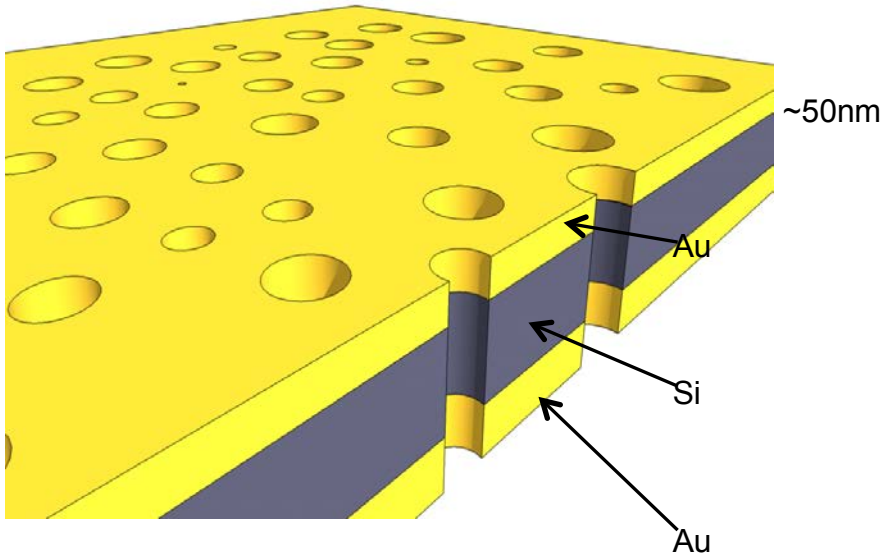

Figure 3.3: Schematic cross section of the metallized membrane showing the freestanding membrane with metal on the top and bottom. The thickness of the structure can be as small as 45 nm.

The nanocrystalline membranes are made using standard microfabrication techniques. In this technique, a rapid thermal process is used to create nanoholes in a sandwiched SiO_2-aSi-SiO_2 structure deposited on a silicon wafer. The silicon wafer substrate is back etched to fabricate the freestanding membrane structure, as described elsewhere [6]. These membranes can be made in various thicknesses ranging from <10 nm to >30 nm. For our work, we have used 15 nm and 30 nm thick membranes. The pores are spontaneously formed during the nanocrystal nucleation process and hence no precision electron beam or ion beam lithography fabrication is required.

These freestanding membranes are robust and capable of withstanding an atmosphere of differential pressure without plastic deformation or fracture [6]. This mechanical robustness is important because in the next step of device fabrication, a metal film is

deposited on this membrane using electron beam evaporation at 10^{-7} Torr pressure. First, a 3 nm thick Ti layer is deposited on both sides of the freestanding membrane. The Ti layer acts as an adhesion layer for Au. The Au film thickness is 15 nm. During deposition, the membrane is kept such that there is an angle of about 10° between the surface normal and the metal deposition direction. After depositing the metal on one side of the membrane, it is rotated by 180° and metal is deposited on the opposite side of the membrane. Schematic of the angled deposition is shown in Figure 3.4.

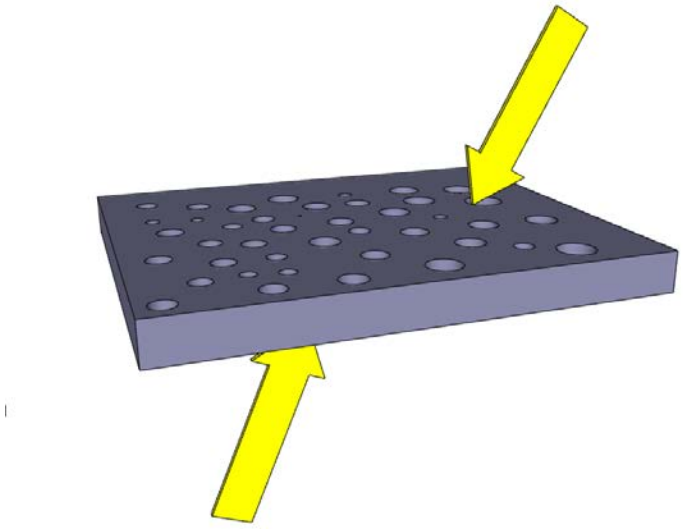

Figure 3.4: Schematic diagram showing the deposition of metal at angles.

Transmission electron microscope measurements are performed on a membrane where metal has been deposited on one side. In Figure 3.5, the TEM image shows the metal deposited on one side of the holes. The RMS surface roughness of the metallized membrane is 0.3 nm, as measured using AFM (see section 2.1.4).

a)

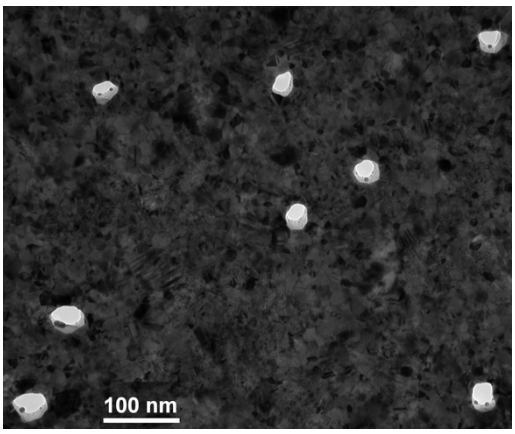

Figure 3.5: TEM image of a metallized membrane with metal deposited at an angle. The metal can be seen deposited on one side of the holes.

3.3 Simulations Results for understanding Interaction of Light with Metallized Pnc-Si Membranes

To obtain a quantitative understanding of how light interacts with this type of free standing metallized structure including when the refractive index of the surrounding medium changes, we make use of three dimensional finite-difference time-domain (FDTD) [120,121] simulations. FDTD simulations are highly effective for understanding light interaction with nanopores and have been used elsewhere [39] to study single apertures in metals. In our work we used commercially available software (FDTD SOLUTIONS from Lumerical Solutions, Inc). Johnson and Christy material data [122] and Palik's material data [123] were used to model Au and Si, respectively.

3.3.1 Scattering Cross-sections of a Single Hole

The effective area around a particle where light either gets absorbed or scattered is defined as the total cross section of the particle. The total cross section of the particle is defined mathematically as the sum of the scattering and absorption cross sections.

Nanoparticles have been studied and characterized using these scattering cross sections theoretically using FDTD simulations [124] as well as experimentally [125]. Scattering cross sections of nanoholes in optically thin metal films have been studied theoretically as well as experimentally [113], where the presence of localized surface plasmons have been seen at the edges of the nanoholes. The structure used here is different from a conventional metal nanohole film on a dielectric substrate. So the scattering, absorption and hence the total cross section for the nanohole is calculated using FDTD simulations. The results shown below in Figure 3.6 show the scattering, absorption and the extinction cross sections for a 30 nm radius nanohole in a 30 nm thick Si membrane with 15 nm Au metal on both sides of the Si membrane. The extinction cross section is the total cross section and is the sum of the scattering and absorption cross sections. A distinct peak in the scattering cross section and hence also in the extinction cross section is seen at around the wavelength of 800 nm. The scattering cross section profiles of these 60 nm diameter nanoholes is markedly different form a Au nanoparticle of the same diameter [126].

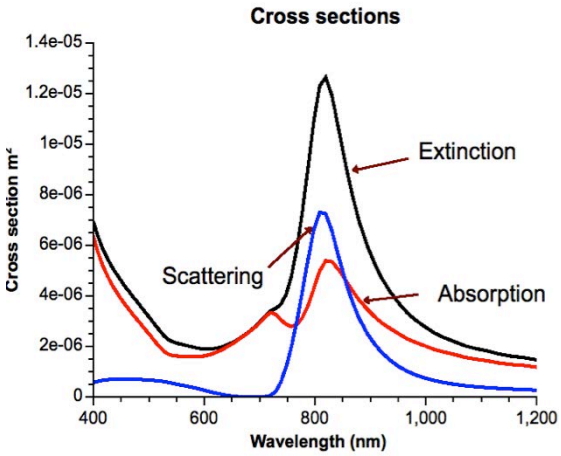

Figure 3.6: The calculated extinction, scattering and absorption cross sections of a 30 nm radius nanohole in a 30 nm thick Si membrane with 15 nm of Au on both sides.

This peak in the extinction cross section shows that nanoholes in this metal insulator metal structure also scatter light and hence their sensing properties can thus be investigated.

3.3.2 Sensing Response for a Single Hole

We first consider a simplified model of a single hole in the metallized Si membrane with a radius 30 nm. The Si membrane thickness for our model is kept at 30 nm and the Au metal thickness on both side of the membrane was 15 nm. The Ti layer is ignored as its thickness is small compared to the Au and Si. The size of the mesh is set at 1 nm. A plane wave was incident on one side of the hole. A two dimensional transmission monitor was placed on the other side of the hole at a distance of 200 nm from the surface of the membrane. This monitor calculates the amount of power transmitted through the monitor normalized to the source power. The simulation was run with 2 different medias, air (n=1.00) and isopropyl alcohol (n=1.37). The transmission spectra showed two characteristic peaks as seen in Figure 3.7a. Peak 1, which corresponds to the maximum transmission is blueshifted by 14 nm with increasing refractive index. Peak 2, which occurs at a larger wavelength, was red shifted by 72 nm with increasing refractive index. To understand the origin of these two peaks and their red or blue shift, the electric field intensity was plotted along the cross section of the hole at the two resonant wavelengths. As shown in Figure 3.7c, for the longer wavelength red shifted peak, the field is confined inside the hole and resembles the cavity mode of a resonator. As expected for such a mode, any increase in the refractive index inside the hole redshifts the resonance

wavelength. The mode profile intensity at the blueshifted peak 1 shows significant field confinement inside the Si membrane, as shown in Figure 3.7b. The mode profile intensity of the blueshifted peak 1 is lower than the mode profile at peak 2, as shown by the relative intensities in the scale bar.

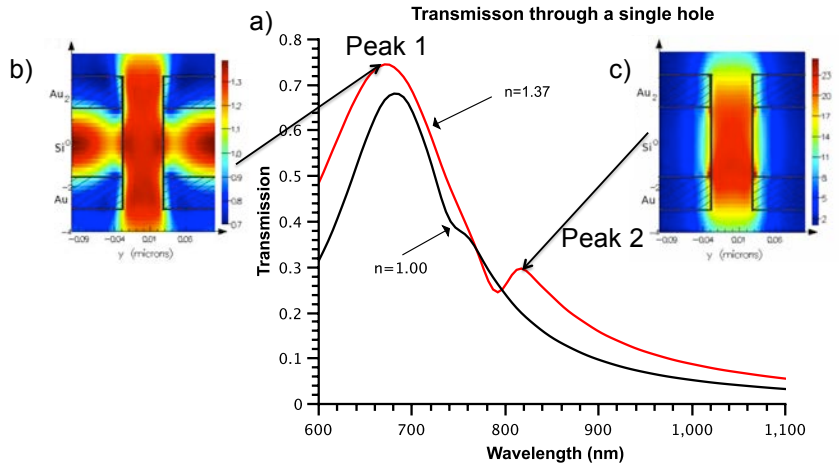

Figure 3.7: a) Transmission calculated through a single hole for refractive index of 1 and 1.37 shown in black and red curves separately. Two distinct peaks are seen for each curve. Peak 1 blueshifts whereas peak 2 redshifts. The insets b) and c) show the electric field intensity at 2 peak wavelengths with the field enhancement factors shown in the color bars.

Considering the fact that the holes only occupy a small fraction of the membrane, a substantial part of the field goes into Si for this mode. When the refractive index inside the hole and its surrounding membrane increases, the field confined in Si is drawn into the higher refractive index leading to a blue shift for the resonance peak.

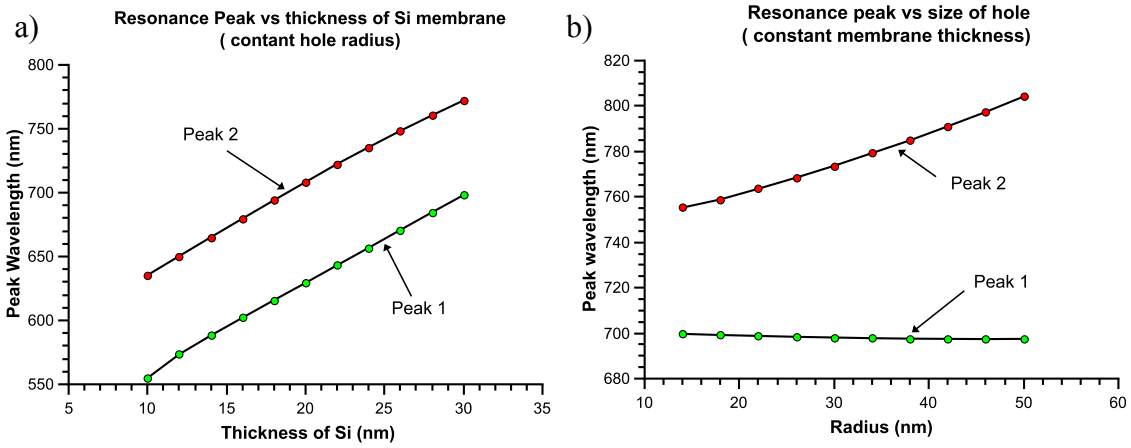

Figure 3.8: a) Resonant wavelengths of peak 1 and peak 2 are plotted against Si membrane thickness, keeping the nanohole size fixed at 30 nm radius. b) Plot of peak 1 and peak 2 position against size of hole, keeping the thickness of Si membrane constant at 30 nm. The metal thicknesses are kept same throughout at 15 nm on each side.

To further investigate these two distinct modes, the resonant wavelength of these modes is plotted against the thickness of the Si membrane and the diameter of the hole separately. In Figure 3.8a, the dependence of peak 1 and peak 2 is plotted against the thickness of the Si membrane keeping the radius of the hole constant at 30 nm. In Figure 3.8b, the dependence of peak 1 and peak 2 is plotted against the radius of the hole, keeping the thickness of the Si membrane constant at 30 nm. Our results show a linear increase in the wavelength of peak 1 with increasing membrane thickness but a very small dependence on the hole radius. In contrast, the mode associated with peak 2 is a "cavity mode", so this mode depends on radius as well as the length of the hole. This can be seen in figures 3.8a and 3.8b, which show a linear dependence of the peak position with respect to the hole radius and the membrane thickness as well.

3.3.3 Simulations for Multiple Holes in the Metallized Pnc-Si Membranes

The simulations shown above correspond to a single hole or a number of identical holes. In our membranes, the pore size is not monodispersive but can be described reasonably well by a Gaussian distribution [6,89]. To accurately model the membrane, the transmission through a square area of 1 μm^2 is calculated.

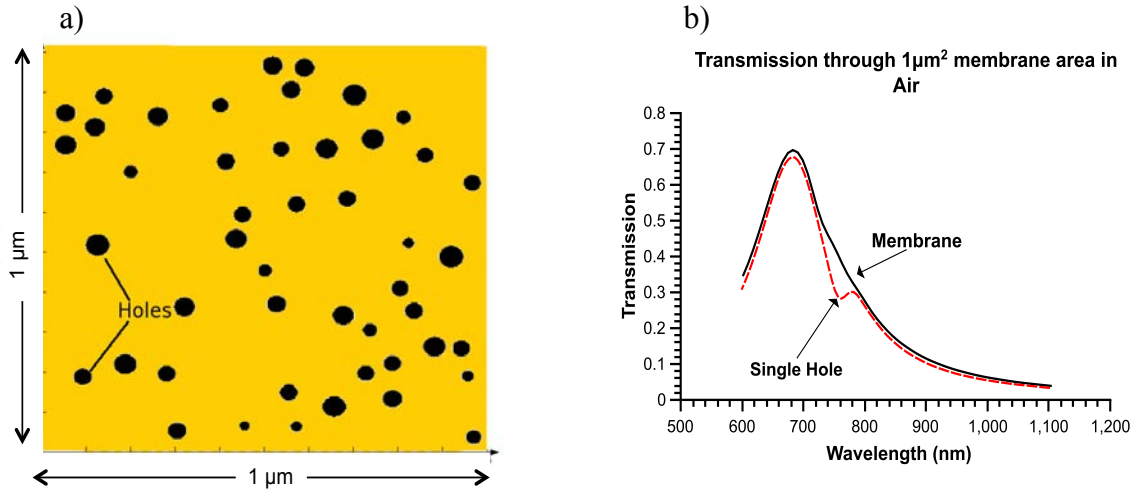

Figure 3.9: a) 1μm^2 area of membrane being simulated for calculating transmission. The hole size distribution is Gaussian and the holes are placed randomly. The porosity and average diameter resemble that of the actual metallized membrane. b) Comparison of calculated transmission for membrane and single hole.

A Gaussian distribution of hole radii sizes having lower and higher cutoffs at 2 nm and 30 nm, respectively, was randomly distributed on the membrane as shown in Figure 3.9a. The membrane porosity of 15% and the average pore radius of 14 nm are typical values in our work. The transmission through the membrane was compared with the transmission through a single hole with the same average size (Figure 3.9b). In the spectrum for the membrane, the cavity resonant peak 2 is absent. The wavelength of peak 2 depends on the size of the nanoholes. Since there are holes of different sizes, each of

these holes peaks at a different wavelength. The net result is a weak shoulder instead of a distinct peak. However, the peak at the smaller wavelength, which depends on the thickness of the Si layer, is identical for a single hole or a hole size distribution. As shown in figure 3c, this mode blue shifts with increasing refractive index. The result is that with increasing refractive index, the transmission through these membranes blue shifts. These results are in sharp contrast to the red shift seen for increase in refractive index for nanohole sensing [127].

3.4 Experimental Results

In this section the sensing of properties of the metallized pnc-Si membrane are measured and investigated. First, the sensing property of the Si membranes is investigated by thermally growing an oxide layer over the pnc-Si membrane before metallization. The results are compared with simulations. Next, the sensing properties of these membranes are characterized experimentally and theoretically for liquids. In the last section, thiol terminated alkane molecule of different sizes is chemically deposited and the sensing properties are again investigated.

3.4.1 Sensing Properties of the Metallized Pnc-Si Membrane

A preliminary test of the sensitivity of the membrane and the accuracy of our simulation models was devised. In this test, the pnc-Si membrane was oxidized in a tube furnace for various times at 800 ˚C in an O_2 atmosphere. Inert Ar was flowed while

loading and unloading the samples. The thickness of the oxide layer over the membrane depends on the oxidation time and temperature. TEM images comparing the pre and post oxidation of the pnc-Si membrane is shown in Figure 3.10 for 15 min and 45 min oxidation at a furnace temperature of 800˚C. The figure shows that after oxidation, the contrast in the image showing the various nanocrystal orientations is decreased. With the growth of the oxide, the nanocrystal diffraction efficiency decreases. Some nanoholes that were not totally open before oxidation disappear when the membrane is oxidized. The contrast of membrane decreases with higher oxidation time, in this case 45 min. Hence, from these images it can be inferred that it is possible to grow different thicknesses of oxide on these freestanding pnc-Si membranes. It is also possible to oxidize the Si totally to make SiO_2 membranes by keeping the pnc-Si membrane in the furnace at 900˚C for 45 minutes.

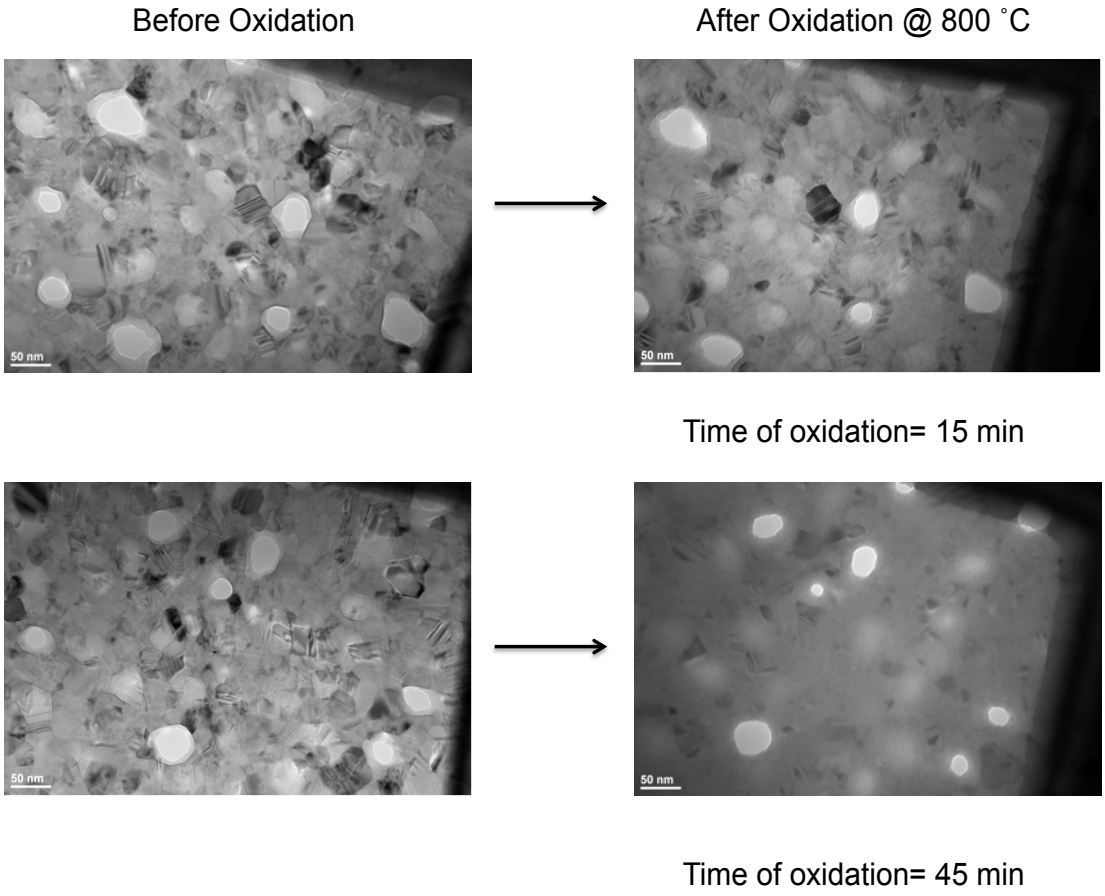

Figure 3.10: TEM image of pnc-Si membranes, intially 30 nm in thickness, before and after oxidation shown at the same position to compare the nanohole and nanocrystals. The images show two sets for 15 min and 45 min oxidation time at 800˚C furnace temperature in an Ar environment.

Fully oxidized pnc-Si(SiO_2) membranes and non-oxidized pnc-Si membranes, initially 15 nm in thickness, are metallized in the next step using the standard electron beam evaporation to deposit 3 nm of Ti and 15 nm of Au. The transmittance in percentage is then measured using a Perkin Elmer Lambda 900 spectrophotometer for the above two membranes and also for a pnc-Si membrane without any metal deposition. The experimental results are shown in Figure 3.11a. The non-metallized pnc-Si transmittance

spectrum resembles the transmittance from an ultrathin Si membrane and matches the FDTD simulation result observed in Figure 3.11 b.

Both the metallized Si membrane and SiO_2 membrane show characteristic peaks. The peak of the Si membrane at 550 nm is red shifted when compared with peak SiO_2 membrane at 675 nm. The same trend is seen in the simulations. In Figure 3.11b, the metallized Si membrane shows 2 peaks; this is however not seen experimentally.

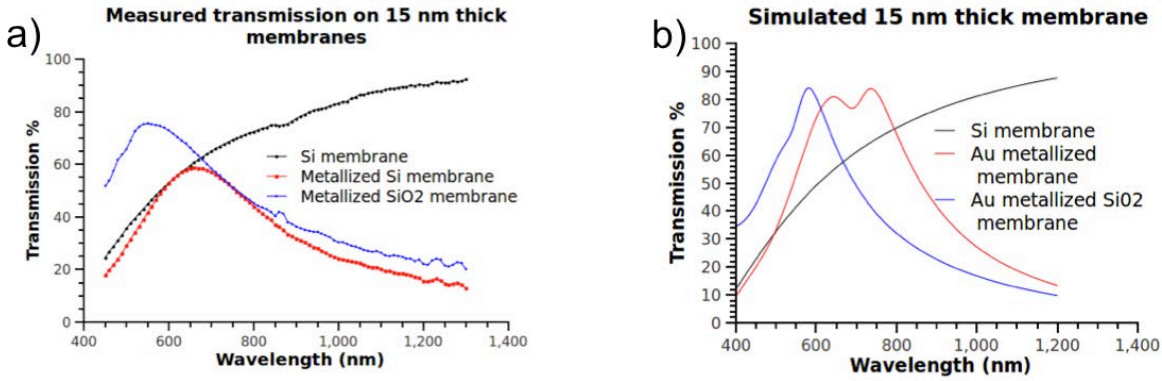

Figure 3.11: a) Transmittance measured from a pnc-Si membrane, initially 15 nm in thickness, metallized pnc-Si membrane and metallized oxidized pnc-Si membrane. b) The experimental results are compared with FDTD simulations of models of the membranes. The figures show good agreement with the position of the transmission peaks.

Next, pnc-Si membranes, initially 30 nm in thickness, are oxidized for different times of 15 min and 45 min respectively. They are metallized using an electron beam evaporator to deposit 3 nm of Ti and 15 nm of Au. The transmittance of these partially oxidized metallized membranes is measured and the results are plotted in Figure 3.12. The figure shows that there is a shift of 27 nm between the two samples. The transmittance levels from the two samples are also different, with the 15 min oxidized sample showing higher transmission.

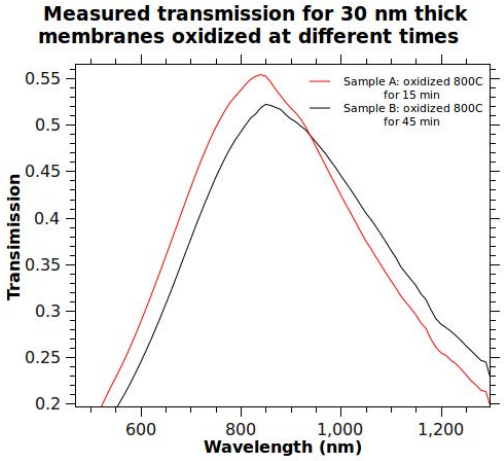

Figure 3.12: Measured transmittance from metallized partially oxidized 30 nm pnc-Si membranes. Sample A (red) and Sample B (Black) are oxidized in a tube furnace at 800˚C for 15 min and 45 min respectively.

These experiments demonstrate that FDTD simulations can predict the transmission characteristics of the membranes. It is interesting to note that the transmission peak from an initially 30 nm thick metallized pnc-Si membrane is red shifted to 825 nm when compared with the transmission peak of 15 nm thick pnc-Si membrane with a peak at 675 nm.

3.4.2 Sensing in a Liquid Environment

Transmission spectra were measured for metallized membranes using a Perkin Elmer Lambda 950 UV/Vis/NIR spectrophotometer and an integrating sphere to capture the total transmitted energy. A 20X objective was used to illuminate only the membrane area.

Transmission measurements were done in an environment of air, methanol and iso-propyl alcohol (IPA). Methanol and IPA have a refractive index of 1.3284 and 1.3772 at 20 °C, respectively. The angle of the incident polarization of the beam was kept constant. Figure 3.13 show that the transmission peak blue shifts with increasing refractive index. The transmission intensity is also seen to be increasing with increasing refractive index. This is because the effective area of the holes increases with increasing refractive index, thereby increasing the amount of transmitted light. Transmission peak in air occurs at 725.1 nm and the transmission peak in IPA blue shifts to 698.1 nm. The resulting sensitivity is 71.6 nm/RIU. In contrast, the transmission peak in methanol blue shifts to 714.9 nm, corresponding to a sensitivity of 31.1 nm/RIU. The smaller than expected blue shift for methanol can be explained with the help of simulations, the results of which are shown as solid curves in Figure 3.13. While modeling IPA, the refractive index on both sides of the membrane is changed. Good agreement is seen between the experimental and simulated data for air and IPA. For modeling with methanol, a good fit between theory and experiments is obtained when the refractive index of only one side of the membrane

was changed. In the experiments, IPA went through the pores to wet both

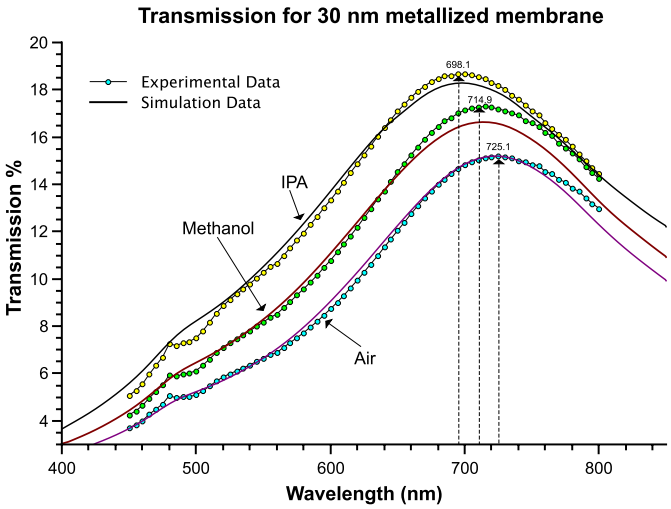

Figure 3.13: Experimentally measured transmission spectrum for the metallized membranes in an environment of ambient air, IPA and methanol is plotted with dots and lines. The simulation fit is plotted as solid line. 1 μm^2 area of the membrane with a porosity of 7% was modeled with 13 nm of Au and 3 nm of Ti on both sides of a 32 nm thick Si membrane. These values closely resemble the experimental values used in the fabrication.

sides of the membrane but methanol exposure was limited to only one side. This blue shift and the relative transmission intensities corroborates with the simulations.

In Figure 3.13, to fit the experimental data 3 nm of Ti has to be included. This thickness of Ti is a fraction of the wavelength but is still important in fitting the experimental data. In Figure 3.14, the experimental transmission data of the metallized pnc-Si membrane is compared with the simulated data with and without 3 nm Ti. Without Ti and with 15 nm of Au and 30 nm of Si, the simulation results show that the full width half maximum (FWHM) of the curve is much narrower than the experimental data. The peak of the transmission curve is blue-shifted with respect to the experimental data. To fit

the data, the 3 nm of Ti is included with 32 nm of Si and 13 nm of Au on both sides of the membrane.

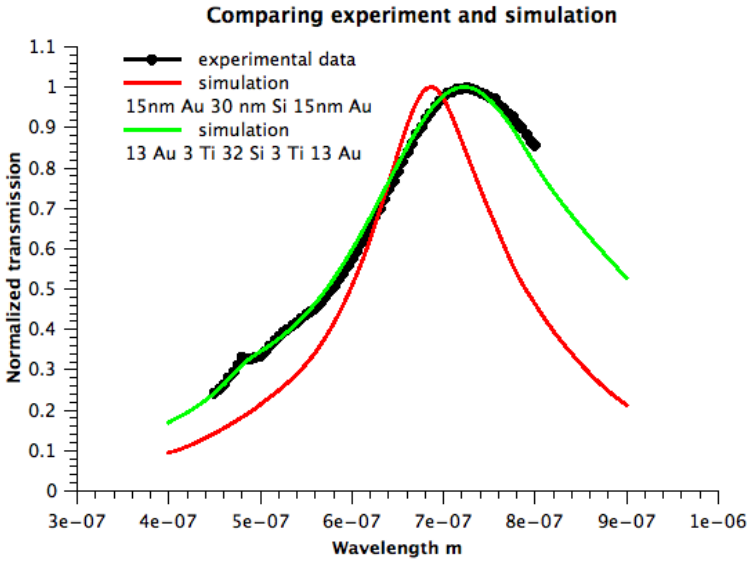

Figure 3.14: Importance of 3 nm thick Ti is shown in fitting the experimental data of the transmission of the metallized pnc-Si membrane (shown in black). Without the including the Ti the full width half maximum of the simulated transmission curve (shown in red) is smaller than the data.

In metal films, only the roughness and thickness of metal can be varied, but the porous nature of our membranes allow the deposition of metal at opposing angles as shown in section 3.2. It is expected that some metal will be deposited on the inner surface at the two opposite openings of the hole. This creates a metal geometry where the transmission of the device depends on the incident polarization of the beam. The simulation model of such deposited nanohole with its cross-section taken along the plane of angle deposition is shown in Figure 3.15a. The electric field intensity is plotted for such a structure and is shown in Figure 3.15b. The incident field is a plane wave with its polarization parallel to the plane of the angled deposition, which in the figure is the z axis. The source is towards

the left of the figure moving right. The electric field intensity profile shows the creation of hotspots [128,129]. The electric field intensity enhancement factor shown in the color bar of Figure 3.15b shows a value of 100 which is 4 times higher than a similar structure where the metal deposition is simulated as being perpendicular deposition (not shown here).

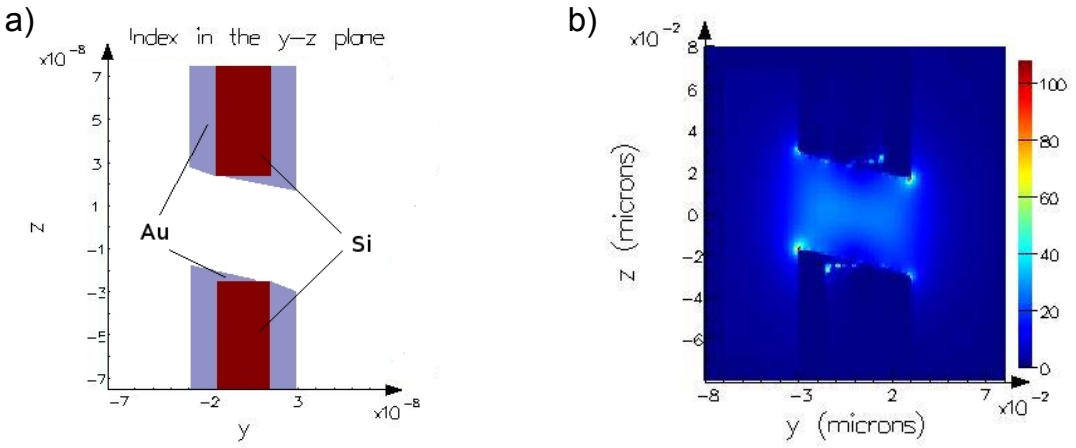

Figure 3.15: a) Cross-section of a 3D model of a nanohole in a metallized membrane. The metal is deposited at angles. b) Electric field intensity profile of the model. The incident electric field is coming from the left of the figure. The polarization is along the z axis. The electric field intensity profile shows the creation of the hot spots, when the incident electric field is parallel to the plane of the angled deposition.

To measure and study this effect, the metallized membranes are rotated along their surface normal while keeping the incident polarization beam fixed and their transmission is measured in the spectrophotometer. The transmission peak of the membrane is found to shift periodically as the membranes are rotated, as shown in Figure 3.16a. Here 0˚ corresponds to the incident electric field being parallel to the plane of angled deposition of metal, 90˚ corresponds to the perpendicular angle. A structure having a single

metallized hole resembling the deposited structure was modeled and the transmission calculated for different polarizations. The simulation result seen in Figure 3.16b shows that it follows the same periodic trend as seen in the experimental results.

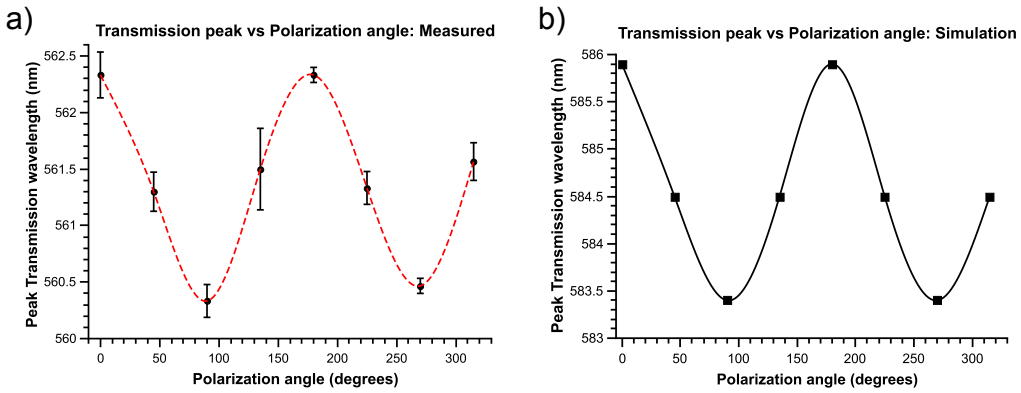

Figure 3.16: a) Experimental transmission peak position versus the incident polarization angle. A periodic trend in the peak wavelength is shown with the dotted curve. b) Simulation of the transmission peak position versus incident polarization angle is shown here for a model of a single metallized hole resembling the deposited structure. The curve joining the points is just an aid to the eye.

The sensitivity of the device is also found to depend on polarization. The blue shift due to IPA measured at 0˚ is 17 nm while for 90 it is 9.5 nm. This confirms that on using the angled deposition, the device becomes polarization sensitive.

3.4.3 Sensing of Thiol Terminated Molecules

In further demonstration of sensing, 100 µM of mercapto-1-hexanol and 1-decanthiol were put on one side of the metallized membranes and incubated in a moist environment. After 2 hours, these membranes were washed with DI water to removes excess thiols. Mercapto-1-hexanol and 1-decanthiol are 6 chain alkane and 10 chain alkane thiol

terminated molecules. The thiol reacts with the Au surface to create a bond and creates a monolayer of the molecules over the surface [130,131]. The length of the chain determines the thickness of the monolayer. This created a monolayer of thiols attached onto the gold surface of the membranes, as shown in Figure 3.17.

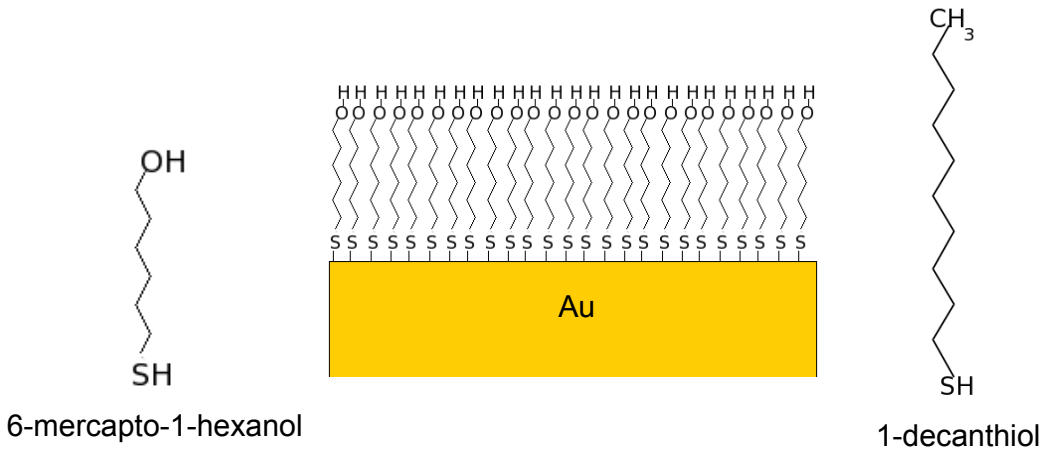

Figure 3.17: Schematic of the thiol terminated alkane molecules 6-mercapto-1-hexanol and 1-decanthiol. The thiol terminated end bonds with the gold surface creating a monolayer of molecules over the Au surface.

Figure 3.18 shows the measured blue shift, induced due to the monolayer of the thiol chemicals at two different polarizations 0˚ and 90˚ with respect to the angle of deposition. The sensitivity of the membrane is seen to be again higher when the incident polarization is parallel to the angle of deposition.

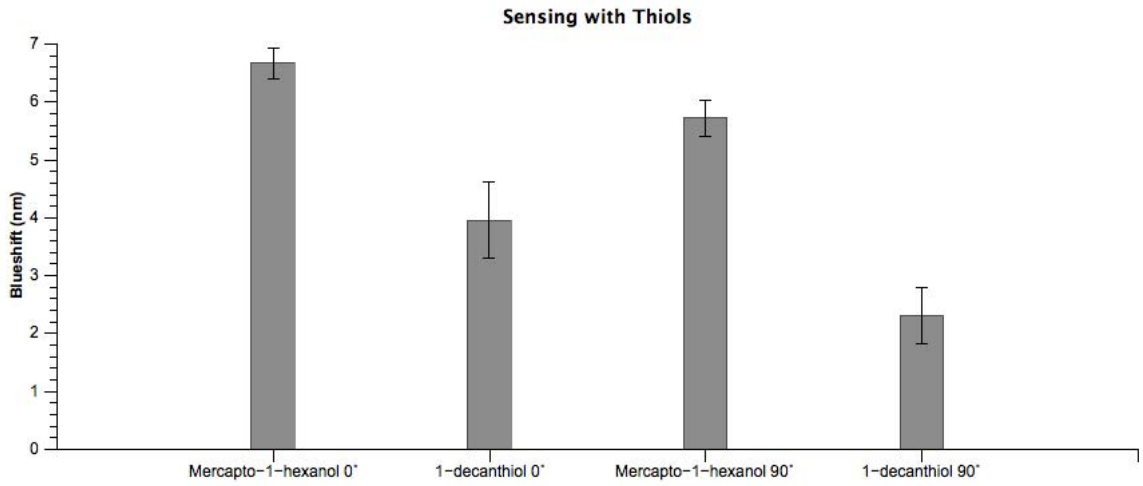

Figure 3.18: Blue shift induced by monolayer thickness of Mercapto-1-hexanol and 1-decanthiol with two polarizations of the incident light. One polarization is parallel to the angle of deposition of the metal and the other perpendicular to it.

It is also seen from the data that the sensitivity is higher for mercapto-1-hexanol compared with 1-decanthiol. This is surprising as the mercapto-1-hexanol is the shorter molecule and hence the layer that it forms should be thinner than that formed by the 1-decanthiol. It could be due to the greater hydrophilicity exhibited by mercapto-1-hexanol that makes it pack differently from 1-decanthiol to form the monolayer.

3.5 Conclusion

The interaction of light with a freestanding ultrathin metallized porous membrane has been studied in this chapter. Experiment results are validated using three-dimensional FDTD simulations. Sensing attributes of the structure is investigated under oxidation of the Si membrane, in a liquid environment and using thiol terminated alkane molecule monolayers. Sensing experiments show a blueshift of transmission peak with increase of

refractive index, which is in sharp contrast to the usual redshift seen in conventional light-matter interaction biosensing. This contrast is explained with the help of simulations.

Chapter 4 Nanohole and Slot Effect

In this chapter, the interaction of light with air slots in nanoholes is described. In section 4.1, the slot effect is introduced and depicted. The description here is based on slot waveguides. In section 4.2, the conceptual structure and experimental fabrication is discussed. The simulation results of the slot effect in the nanoholes are described in section 4.3.

4.1 Background

In this section, waveguide geometry is used to demonstrate the principle of confinement of light in a low refractive index medium. The continuity of Maxwell's equation across the boundary is the basis of this slot effect.

4.1.1 Introduction to the slot effect

The slot effect is a direct consequence of the general boundary condition for electrodynamics coming from Maxwell's equation [132]. A schematic of an infinite waveguide, shown in Figure 4.1, is used in illustrating the effect. The figure shows an infinite waveguide having a low refractive index region n_S inside a waveguide with a core with a higher refractive index n_H. The extent of the core is 2b in width and that of the slot is 2a. The cladding region has an index of n_C.. The general boundary condition for electrodynamics across the interface between the slot and higher refractive index region of the core of the waveguide for the linear medium is given as $D_S^N - D_H^N = \sigma_f$, [133]

where D_S^N and D_H^N are the normal components of electric displacement in the slot and high refractive index region, respectively. σ_f is the free charge at the interface. As there are no free charges, $\sigma_f = 0$. Hence the normal component of the electric displacement across the interface is continuous, i.e. $D_S^N = D_H^N$. The electric displacement can be further written as $\varepsilon_S E_S^N = \varepsilon_H E_H^N$, where ε_S and ε_H are the dielectric constant of the slot region and high index core region, respectively. The dielectric constant in a medium is the square of the refractive index of the medium. Hence, it follows $\frac{E_S^N}{E_H^N} = \frac{n_H^2}{n_S^2}$. So the ratio of the normal component of the electric field inside the slot and core is equal to ratio of square of the refractive index of the core region to the slot region. In most cases and true for the case used here, the slot region is air, so $n_S = 1$. Then the slot field is enhanced by a factor of n_H^2 over the field inside the high refractive index region.

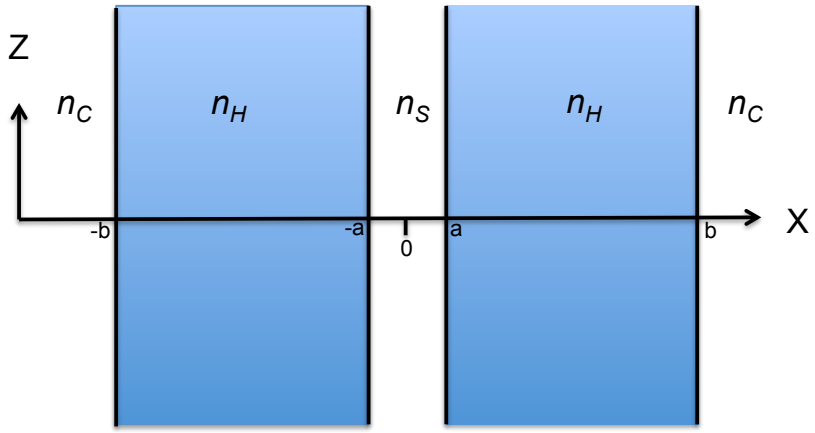

Figure 4.1: Schematic of a 2D waveguide structure showing the slot within the core region of the waveguide. The core has an index of n_H, and the slot has a lower refractive index of n_S. The high index slabs are infinite in the Y and Z direction [61] .

The electric field of such an infinite slab slot waveguide has been plotted by Almeida et al. [61], which is shown in Figure 4.5. The figure shows that the electric field inside the slot is higher than the electric field in the core. This happens only when the width of the slot is much smaller than the decay length of the mode in the waveguide. The evanescent field in the core on both sides of the slot must be able to interact with each other.

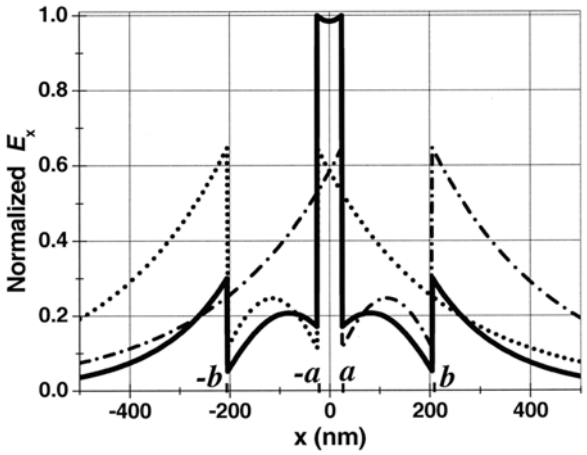

Figure 4.2: Normalized electric field E_x plotted across the slab slot waveguide. The electric field inside the slot region (-a<x<a) shows the peak associated with the slot. The ratio of the electric field in the slot to the electric field in the core region is $n_H{}^2$, which in this case is the square of the refractive index of Si. (Reprinted from [61]).

4.2 Concept and structure

Enhancing light-matter interactions has important applications in sensing [62,63], trapping [64], quantum optics [134] and telecommunications [135]. This enhancement is achieved either by increasing the quality factor (Q) of a resonator, as shown in photonic crystals [136],or by decreasing the mode volume using slot waveguides [65] or plasmonic nanostructures such as nanoholes [60,137,138]. Nanoholes in metal films have shown the phenomenon of extraordinary transmission of light [31]. This leads to light

localization inside the nanohole cavities and has been used for increasing fluorescence yield for molecules [24]. Slot waveguides have been shown to confine and enhance the modes of waveguides into a low refractive index slot [61]. Here a novel freestanding structure that merges the nanohole localization of the electromagnetic energy with the confinement and enhancement property of a slot waveguide is proposed. This creates a structure with an ultra-small mode volume. In this section, such a structure is numerically studied and steps of fabrication outlined.

4.2.1 Fabrication

The fabrication step involves the metallization of the pnc-Si membrane on both sides of the membrane with the help of electron beam evaporator. The metal can be a plasmonic material like Au or Ag. Al_2O_3 is deposited conformally using an atomic layer deposition tool. The schematic of the device is shown in Figure 4.3. The ALD gives a precise control over the thickness of the Al_2O_3, which is shown in blue in the schematic. The slot is created inside the open nanoholes. There is a distribution of hole sizes in the membrane which leads to slots of different sizes. The higher refractive index region, in this structure, is the conformally deposited Al_2O_3 inside the nanohole; the slot is the open volume at the center of the nanohole. The fabrication of the structure is outlined in details in section 2.2.

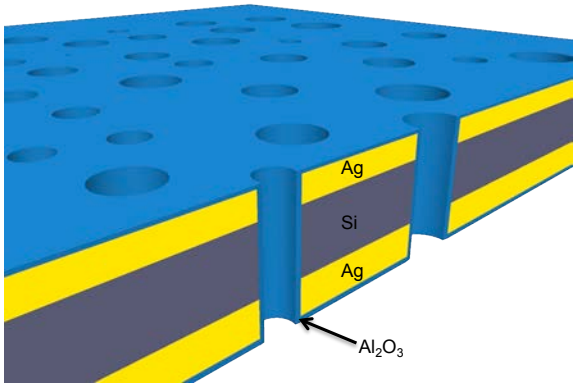

Figure 4.3: Schematic of the slot metallized pnc-Si membrane. The ALD deposited Al_2O_3 is shown in blue. The slot is created inside the hole, where the higher refractive region is Al_2O_3 and air is refractive index of the slot.

4.2.2 Simulation model

The simulation model is based on an ultrathin porous nanocrystalline metallized Si membrane [89], as described in section 3.3. To study this structure, FDTD simulation software from Lumerical Solutions is used. Although the proposed device would have a distribution of hole sizes over a large area, here the simulation is limited to a single hole. A three-dimensional structure representative of the hole is simulated and a schematic of the cross-section of the structure in the x-z plane is shown in Figure 4.4. The Si membrane is 28.5 nm thick, the Ag metal on both sides are 30 nm thick. The Al_2O_3 layer is 15 nm in thickness all over the structure. This creates an air slot, 10 nm in diameter for the 40 nm diameter hole. The source is a plane wave coming from the bottom of the structure with the electric field along the x-axis. The mesh is kept at 0.1 nm around the slot for the simulations. There are a number of monitors to measure and record the electric fields and transmission of the device.

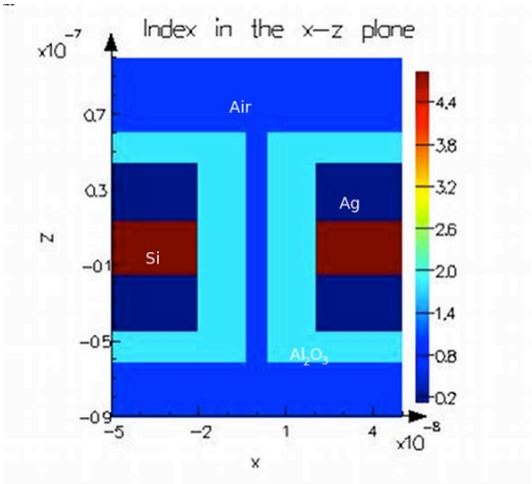

Figure 4.4: A schematic of the cross section of the three dimensional structure along the x-z plane is shown. The size of the nanohole is 60 nm in diameter and the thickness of the conformal layer of Al_2O_3 is 15 nm, leaving a 15 nm diameter slot in the middle of the hole. The thickness of the pnc-Si membrane is 28.5 nm and the thickness of the plasmonic metal Ag is 30 nm on both sides of the pnc-Si membrane.

4.3 Simulation results

In this section the single nanohole slot structure is studied in detail. The electric field intensity is plotted in the logarithmic scale at the resonant slot mode. Next, the resonant field profiles are studied with the variation of the slot size, nanohole size and thickness of the metal layers. The Purcell enhancement factor of the structure is also calculated.

4.3.1 Resonant slot mode

The electric field intensity in logarithmic scale is shown in Figure 4.5 at a resonant wavelength of 665 nm. From the scale, it is seen that a substantial part of the field gets confined in the air slot. Intense localized surface plasmons (LSP) are seen at the interface corners between the Si and Ag metal. The LSP generated in the interfaces are much stronger than the slot effect. The slot effect “squeezes” the electric field of the cavity

mode of the nanohole into the low refractive region. To study the effect, simulations for various slot and hole sizes are performed keeping the thickness of the Si membrane and metal layers constant.

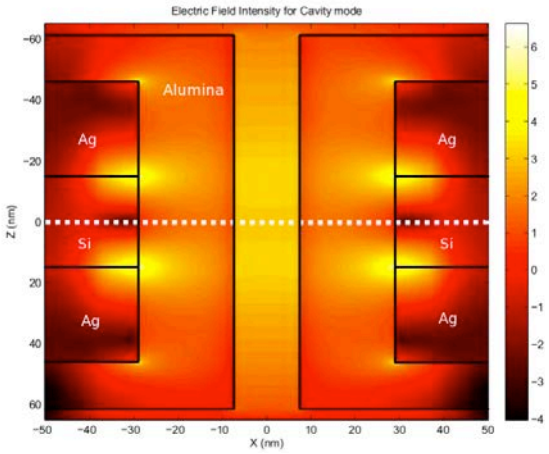

Figure 4.5: The outline of the structure shows the 60 nm hole with the 15 nm diameter slot. The Si membrane and Ag layer are 28.5 nm and 30 nm thick respectively. The electric field intensity is plotted in the logarithmic scale and shows the slot enhancement and the LSPs at the interface between metal and insulator. The field is plotted at the resonant slot wavelength that is 665 nm in this case.

In order to focus our study on the slot effect and to avoid contribution from the LSP's, the electric field intensity is plotted along the x axis (along the white dashed line in Figure 4.5), is shown in Figure 4.6. In the simulations, the incident electric field has a value of one, so the electric field intensity plotted along the y-axis is also the measure of the electric field intensity enhancement factor. This line is along the center of the Si membrane where the field due to LSP is absent. This electric field profile matches the profile shown in Figure 4.2.

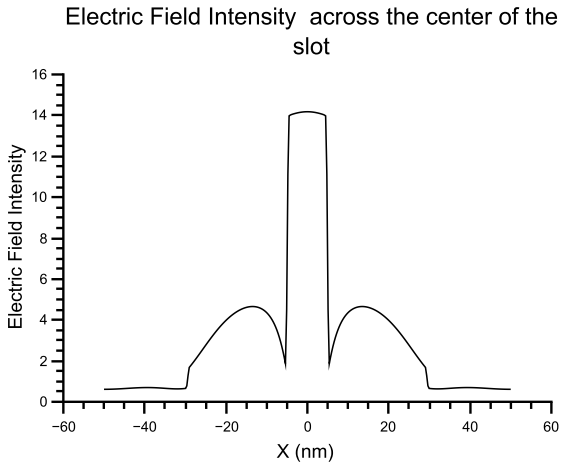

Figure 4.6: Electric field intensity along the center of the slot structured metallized nanohole. The y-axis of the electric field is in linear coordinates. The figure shows that the electric field in the slot gets enhanced and localized.

4.3.2 Effect of varying slot size

Electric field profile for different slot sizes ranging from 2.5 nm to 20 nm in diameter are plotted for a 40 nm diameter hole. The thickness of the pnc-Si membrane and the metal thickness are kept the same at 28.5 nm and 30 nm respectively. The field intensity profile for the different slot sizes is shown in Figure 4.7a; all resembling the typical profile of a slot mode [50]. Figure 4.7b shows the change in intensity enhancement factor at the center of the slot (in black) and the calculated modal volume (in red) with the variation in size of the slot. As the slot becomes smaller, the electric field intensity enhancement factor at the center of the slot increases. The modal volume follows a reciprocal trend and decreases with decreasing size of the slot. When the slot size becomes 0 nm, i.e., the slot collapses, then it is seen that the slot effect disappears, the

intensity of the electric field decreases and the modal volume increases. In the case when the nanohole does not have the Al_2O_3 layer, depicted in Figure 4.7a by a slot size equal to the nanohole size of 40 nm, the electric field enhancement factor is lower and the modal volume higher than the 0 nm slot size. The increase in intensity and decrease in modal volume is due to the nanohole being filled with Al_2O_3 which then effectively creates a bigger hole such that more light is transmitted through it.

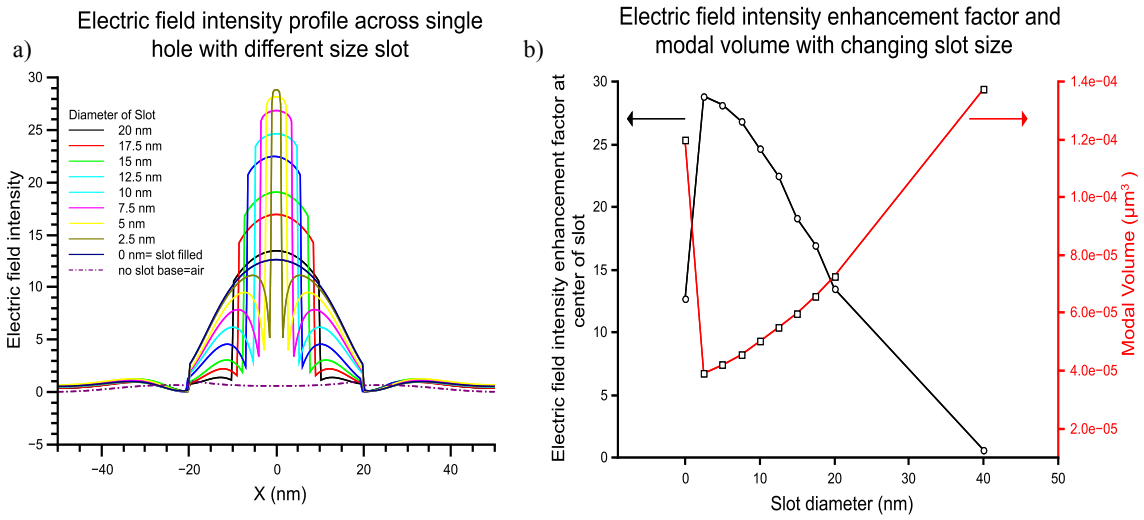

Figure 4.7: a) The electric field intensity enhancement factor plotted along the white dashed line of Fig. 1. Only the thickness of the encapsulating Al_2O_3 layer is changed in order to change the slot size. b) The black line plots the electric field intensity at the center of the slot (X=0). The red line plots the modal volume as a function of the slot diameter. As the slot becomes smaller, the electric field increases while the modal volume decreases. As the slot closes in on itself, the slot effect disappears and the electric field intensity falls and the modal volume increases. At 40 nm slot size, the diameter of the slot becomes same as that of the nanohole, effectively it means that there is no Al_2O_3 layer on the structure.

The smallest calculated modal volume is 4 $x10^{-5}$ μm^3, the mode with a q factor of 20 gives a Purcell enhancement factor [42,135] of $8x10^3$.

4.3.3 Effect of varying nanohole size

The intensity enhancement is also plotted for different size nanoholes with fixed slot size of 10 nm in Figure 4.8. The thickness of the Si membrane and the metal thickness are kept constant. From the figure, it is seen that the slot mode width does not change, yet the electric field intensity in the core region varies with the size of the nanohole. The inset of Figure 4.8 shows the intensity enhancement at the center of the slot. This inset shows that there is an optimum size of the nanohole to get maximum enhancement, which in this case is 45 nm.

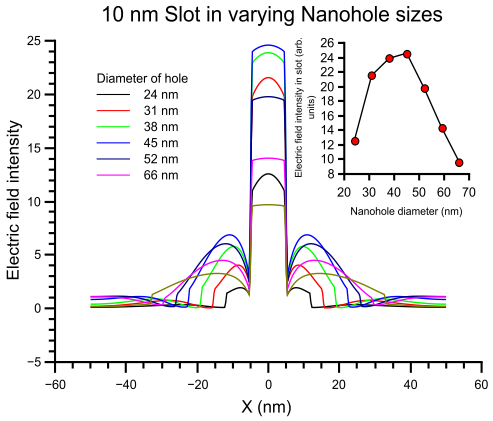

Figure 4.8: The electric field enhancement factor is plotted along the x direction across the center of the slot. The slot size is kept fixed at 10 nm, while the diameter of the nanohole is changed keeping all other parameters same. The inset shows the electric field enhancement factors at X=0, i.e. the middle of the slot. The inset shows that there is an optimum nanohole diameter for a fixed slot size and length.

4.3.4 Effect of varying the metal layer thickness

In another similar study, the size of the nanohole and the slot is kept fixed at 40 nm and 10 nm respectively. The metal thickness on both sides of the pnc-Si membrane is varied simultaneously from 5 nm to 40 nm thicknesses. The electric field intensity along the center of the structure is plotted at the slot resonant mode in Figure 4.9.

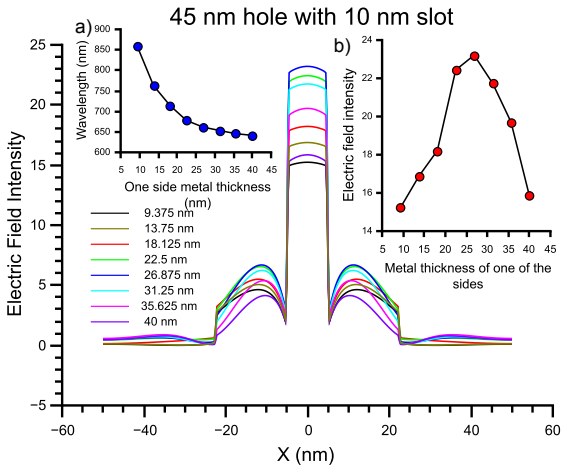

Figure 4.9: The electric field intensity is plotted across the center of the slot structure along the x-axis. The metal thickness on both sides of the membrane is varied keeping the slot size and nanohole size fixed. Inset a) plots the change in the resonant wavelength against the variation in the metal thicknesses. Inset b) plots the electric field intensity enhancement factor at the center of the slot against the thickness of the metal layer.

The electric field is plotted across the center of the structure along the x-axis. The width of the slot mode (at x = ± 5 nm) and the nanohole mode (at x = ± 20 nm) does not change because the nanohole and slot size is not changed. However, when the thickness of metal is changed, the resonant slot mode varies with the metal thickness. This is plotted in the inset a of Figure 4.9, where the resonant slot mode wavelength is plotted against the

thickness of the metal layer. It is seen from the inset that as the metal thickness increases, the slot mode blue shifts to lower wavelength. This gives a way of tuning wavelength of the slot mode by controlling the thickness of the deposited metal. In inset b, the electric field intensity enhancement factor at the center of the slot is plotted against the thickness of metal on one side. The plot shows that there is an optimal thickness for which the enhancement is highest; in this case it is ~27 nm.

4.3.5 Three dimensional visualization of the slot mode

For visualization of the mode, a 3D map of the fields is shown. Figure 4.10a and Figure 4.10b show the same 3D mode from two different angles for the case when the incident light is linearly polarized. In the figure, only field enhancement factors greater than 12 are shown. The side lobes are due to the localized surface plasmons (LSP) at the interface between the metal and Si. These are also in the direction of the polarization of the incident field. The slot mode is seen confined in the middle. When circular polarization is used instead of linear polarization, keeping all other parameters the same, the side lobe of the LSP's become doughnut shaped in geometry. This is shown in figures 4b and 4c. The incident polarization affects the geometry of the LSP part of the mode. The geometry of the slot mode for circularly polarized light is more circular than the linearly polarized light.

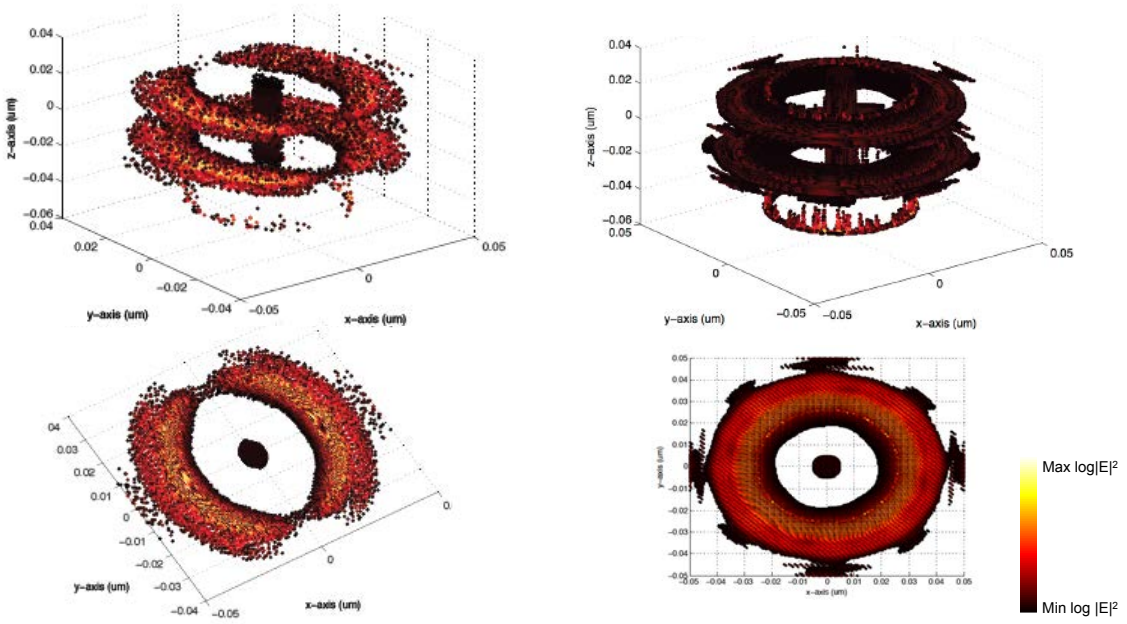

Figure 4.10: a) & b) show the 3D logarithmic electric field intensity profile of the slot mode for linearly polarized incident light. Intensity enhancement factors less than 12 are not plotted in these figures. The LSP lobes are seen in the direction of polarization. The slot mode is seen in the middle. In c) & d) the incident light is circularly polarized, all other parameters are kept same. Circularly polarized light affects the geometry of the LSP and the slot mode also becomes more circular when compared with the linearly polarized light.

4.4 Conclusion

The slot effect within nanoholes in metal-insulator-metal freestanding membranes is investigated. This effect enhances and confines the mode to increase the electric field intensity and decrease the modal volume. The highest electric field intensity enhancement factor is 29 for a 2.5 nm diameter slot and the smallest calculated modal volume for this slot size is 4 $x10^{-5}$ μm^3. An optimum size is found for a fixed nano-slot diameter. The resonant slot mode is found to be dependent on the thickness of metal over both side of

the membrane. The optimum metal thickness is found to be ~27 nm. The geometry of the mode is dependent on the initial polarization of light. Circular polarization produces a doughnut shape mode for the LSP's in contrast to linear polarization that produces lobes.

Chapter 5 Photovoltaic Application of Metallized Ultrathin Membranes

In this chapter the photovoltaic application of p-i-n junction type of hydrogenated amorphous Si (a-Si:H) metallized ultrathin membrane is discussed. Section 5.1 introduces the photovoltaic effect and a-Si:H p-i-n films. In section 5.2, the use of metallized ultrathin p-i-n junctions to make a photovoltaic device is outlined. Simulation of optical interaction of light and experimental results of such p-i-n devices are described in section 5.3.

5.1 Background

In this section the general principle behind photovoltaics and its necessity is described. Later the a-Si p-i-n junction thin films are introduced and discussed.

5.1.1 Solar Cells

The generation of direct current from solar radiation with the help of semiconductor material is called photovoltaics. As the name suggests, this effect has two parts to it; light in the form of photons and electricity in the form of electrons. When photons are absorbed into a photovoltaic semiconductor material, the electrons in the valence band absorb the energy of the photons. The electrons get excited and jump into the conduction band creating electron hole pairs. These electron hole pairs are separated by an electric field and collected by the anode and cathode creating electricity flow. With

solar radiation and semiconducting materials, this photovoltaic effect can be utilized to create a renewable source of energy [69] with a low carbon footprint [139]. For solar energy to be a viable source of alternative energy [67], it needs to be economical and efficient. To satisfy this, the semiconducting active layers need to be optically thick. For an indirect bandgap semiconductor like crystalline Si [140,141], this thickness can be 100 μm [80] and a few microns for a direct bang gap semiconductor like $CuIn_xGa_{1-x}Se_2$ [77]. The use of a substantial amount of material not only increases the material cost, but also increases the time required by the photovoltaic module to payback its energy invested during its fabrication. Thin film solar cells have the potential to lower the fabrication and material cost together with increasing the efficiency [78].

5.1.2 Thin film Solar Cells

Thin film solar cells, a few microns thick have been fabricated using hydrogenated amorphous silicon (a-Si:H) [73], GaAs [74], CdTe [75,76], $CuInSe_2$ [77] and organic semiconductors [78]. Si stands out from the above materials because it is abundant in the earth's crust, has low toxicity and has a mature industry behind it. Crystalline (c-Si) and amorphous (a-Si) are the two common forms that are used in solar cell fabrication. Each has its advantages and disadvantages [71]. Here a-Si is used because it is a direct band gap material, hence the absorption coefficient is higher than c-Si in the visible part of the solar spectrum.

Thin film solar cells must have a high optical absorption coefficient in the solar radiation spectrum. Unfortunately for a-Si, the absorption is rather poor in the near infrared region of the useful solar spectrum. To increase this absorption, methods like

plasmonic light trapping in thin film solar cells [78] have be employed where nanoparticles have been used to trap light and plasmonic back reflectors have been developed [80,142]. Recently, ultrathin a-Si:H n-i-p junction deposited on zinc oxide nanorod array solar cells has been demonstrated where the ultrathin absorber layer is only 25 nm in thickness. It has been found in this study that the ultrathin 25 nm thick solar cells are more efficient, with an efficiency of 3.6%, than a-Si:H solar cells with active layer 75 nm thick with planar or patterned surfaces [84], having an efficiency of 2.6%. Our device consists of an unique solar cell based on ultrathin a-Si:H p-i-n junction.

5.2 Concept and Structure

In this section the concept of the device and fabrication is outlined. The electric field intensity profile previously calculated using FDTD simulations in section 3.3.2 for metallized porous membranes inspired the solar cell application of freestanding ultrathin membranes. Latter part of this section briefly outlines the fabrication of these solar cells.

5.2.1 Concept

Looking back at Figure 3.7, in section 3.3.2 the electric field intensity calculated from the simulation is found to be concentrated mostly in the Si region of the metallized membrane for the mode at the lower wavelength. Further, it was found from FDTD simulations that even with no holes, these metallized membranes concentrate light into the high index dielectric, i.e. Si. When the Si is doped with a p-n or the membrane is made up of a-S:H p-i-n junction, the structure does not change optically. Light is

concentrated in the junction region because of the metal on both sides of the membrane. This is very similar to Fabry-Perot cavity resonance effect [143]; however, the cavity here is of the order of a few tens of nanometers, a fraction of the wavelength of light. This type of cavity resonance effect has been used in improving the optical performance of inverted organic solar cells [144]. In organic solar cells, the refractive index of the active layer is not as high as that of a-Si so the enhancement factor is limited. Organic solar cells also suffer from poor electron-hole transport. Shah et al. [71] have shown p-i-n type solar cells of a-Si:H material. In such structures, it is important for the intrinsic region to have a high optical absorption coefficient and the thickness of the a-Si:H layer is typically kept lower than 400 nm to prevent recombination losses. So it is important to increase the effective optical thickness of the intrinsic layer without increasing the geometric thickness of the intrinsic layer.

The Fabry Perot type effect will increase the effective optical length of interaction of light with material. This is illustrated in Figure 5.1, which shows the electric field intensities and the absorptance for cavity like metallized membrane based solar cell structures, calculated using 3D-FDTD simulation models. Figure 5.1a shows the electric field intensity for an a-Si membrane 30 nm thick with 30 nm of Ag on both sides. The electric field is plotted at the resonant cavity wavelength of 620 nm. From the figure, it is seen that the electric field is confined in the a-Si membrane. The a-Si membrane is representative of the a-Si:H p-i-n junction in the solar cell structure. In the actual structure, the increased absorption inside the a-Si:H p-i-n membrane should correspond to an increase in the interaction of photons with the band structure creating more electron

hole pairs. Figure 5.1b shows the electric field intensity over the outline of the solar cell structure with an a-Si membrane layer thickness of 80 nm and Ag thickness of 30 nm. The structure is exactly the same as the one shown in Figure 5.1a except for the thickness of the membrane layer. This effectively increases the length of the cavity, causing the resonant wavelength to red shift to 915 nm. The absorptivity of both the structures is shown in Figure 5.1c, structure a in black and structure b in blue and is compared with a-Si membrane layer 30 nm thick without any metal layer, plotted in red. From this figure, it is seen that the bare a-Si membrane does not absorb light in the visible to near infrared region of the solar spectra, which has been plotted in Figure 5.2. The quality factor of the resonance also changes with change in thickness of the a-Si layer. Two peaks are seen for the absorptivity spectrum of the 80 nm thick membrane. The peak at 530 nm corresponds to the higher order mode in the cavity. From Figure 5.1c, it is seen that the quality factor of the resonances depend upon the thickness of the a-Si membrane for the same 30 nm thick metal layers on both sides of the structure.

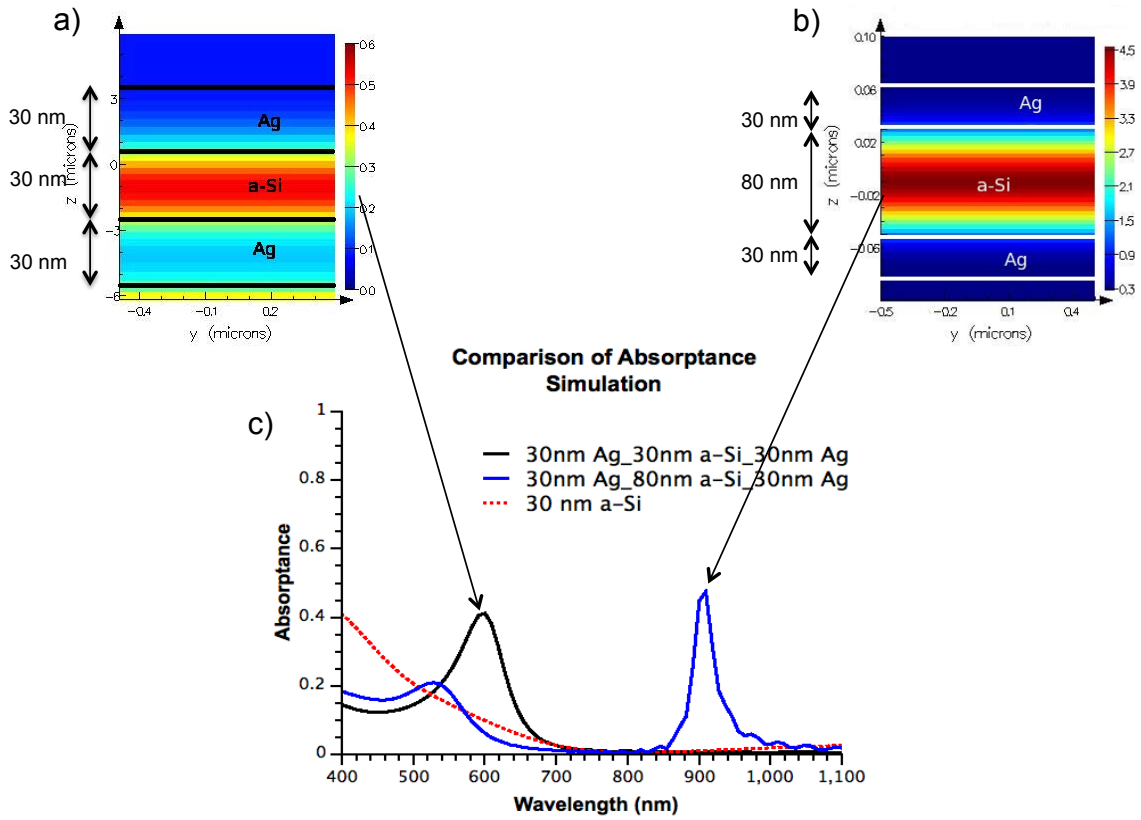

Figure 5.1: a) 3D-FDTD simulated electric field intensity over the solar cell structure. The a-Si membrane thickness (simulating the p-i-n junction of the a-Si:H) is 30 nm and the thickness of Ag metal on both sides is 30 nm. The electric field intensity shown is at the resonant peak wavelength of 620 nm. b) Shows a similar FDTD simulated electric field intensity over the solar cell structure, with a-Si membrane 80 nm thick, keeping other parameters same as in (a). The resonant wavelength is 915 nm. c) Shows the calculated absorptance of 30 nm and 80 nm thick a-Si membranes compared with a 30 nm a-Si membrane without any metal layers.

From the solar spectral radiance, plotted in Figure 5.2, it is seen that the irradiance is highest between 500 nm to 1200 nm. The Fabry Perot based cavity resonance solar cell membranes allows tuning the response of the solar cell across the solar spectrum, above the bandgap of the material in the p-i-n junction. The metal layers in the structure have dual purpose. First, they act as mirrors to make a cavity to trap light; second, they act as

conductive layers to collect the holes and electrons. The thickness of the metal layer is dependent on the quality of deposition to make a continuous layer to keep the sheet resistance low. The quality factor also depends on the thickness of the metal layer. The thicker the metal layer, sharper is the resonance peak and hence higher the quality factor. This gives an added parameter to tune the device to a specific wavelength range.

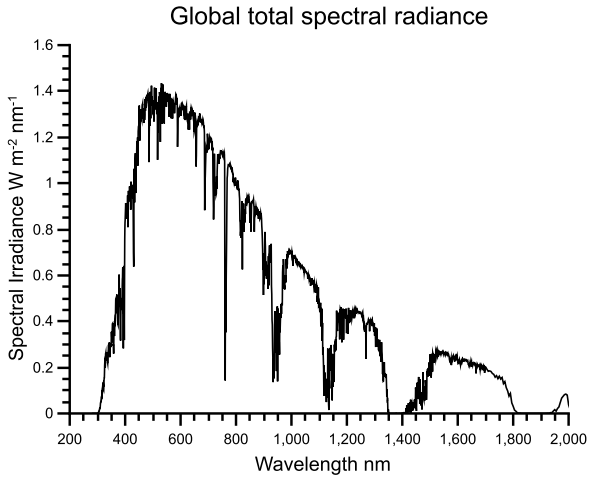

Figure 5.2: Plot of global total solar spectral radiance. (Data taken from [145])

Since the shape and position of the absorptivity can be controlled using such a structure, it can have uses in tandem solar cells [86,87] or as transparent solar cells [88].

5.2.2 Fabrication of Metallized Membrane based Solar Cells

The fabrication of such structures is detailed in section 2.3.1. The fabrication procedure is similar to the fabrication process of the pnc-Si membranes, where a hydrogenated a-Si:H p-i-n junction is deposited in place of a-Si in the sandwiched layer, using a GSI PEVCD tool. Then releasing the membranes using an EDP and BOE etch to create an ultrathin free standing a-Si:H p-i-n junction. This kind of fabrication process helps surpassing the restriction of using metal in the GSI PECVD tool. The metal contact

layers can be added on both sides of the freestanding p-i-n junction as the last step in fabrication. It also allows for adding additional material on both sides of the contact. A schematic of the device is shown in Figure 5.3. The figure shows a 60 nm thick a:Si:H p-i-n junction with 35 nm of Ag on both sides of the junction. The p-doped region is 10 nm and the n-doped region is 20 nm. The light first interacts with the p junction on the front side of the solar cell. This p junction is usually thinner than the n junction; also the absorptance of the p layer is smaller than the n layer. This ensures most of the light is absorbed in the intrinsic layer to create the electron hole pairs.

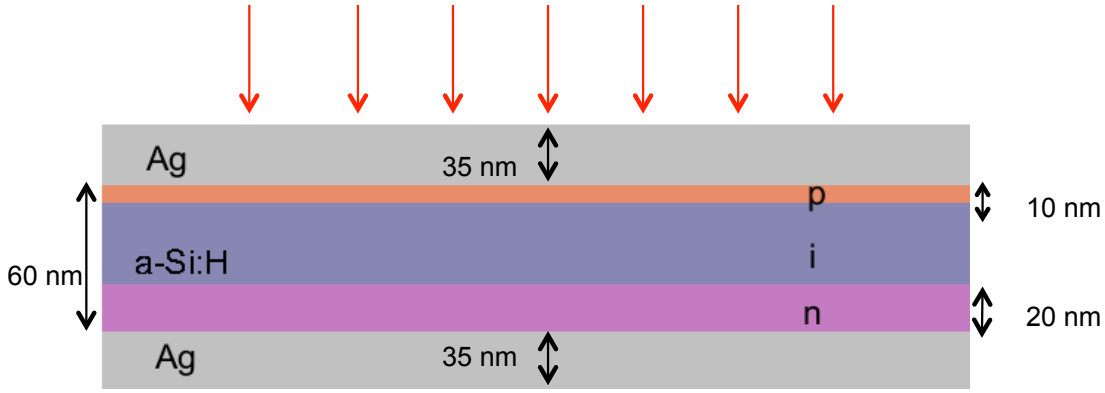

Figure 5.3: Schematic of a freestanding a-Si:H p-i-n junction with metal on both sides of the junction acting as contacts as well as reflectors. The red arrows indicate the direction of illumination.

5.3 Results

In this section, simulation results on the model of the devices fabricated are tested and corroborated. First, absorption calculations from FDTD simulations are compared with the measured absorption of a-Si structures. Next, external quantum efficiency (EQE)

measurements of actual solar cells are compared with simulated absorption results. In the last section, effect of adding ITO layer on top of the metal contact layer to increase sheet resistance and optical coupling is investigated.

5.3.1 Absorption Characteristics of the Solar Cells

To measure the absorptance characteristics of the solar cells, amorphous Si (a-Si) is deposited to imitate the optical response of a-Si:H p-i-n junction solar cell. On top of a standard glass slide, 30 nm of Ag is first deposited using electron beam evaporation. Then using a CVC instrument, 30 nm of a-Si is deposited on top of the metal. Lastly, 30 nm of metal is again deposited on top of the a-Si to create the sandwiched structure to optically imitate the proposed solar cell. The structure's reflectance and transmittance is measured using a Perkin Elmer spectrophotometer using an integrating sphere. The reflectance (R), transmittance (T) and the absorptance (100-R-T) measurements in percentage are plotted in Figure 5.4. The absorptance plot has a peak at 620 nm and is similar to the absorptance peak seen in Figure 5.1c (in black), calculated from the simulation results. The measured absorptance intensity matches the simulated values.

A similar structure is fabricated using the same process, but with an 80 nm thick a-Si layer sandwiched between the 30 nm thick Ag layer. The reflectance and transmittance measurements are plotted in Figure 5.5. The absorptance plot shows two peaks, one at 950 nm, and the other at 610 nm.

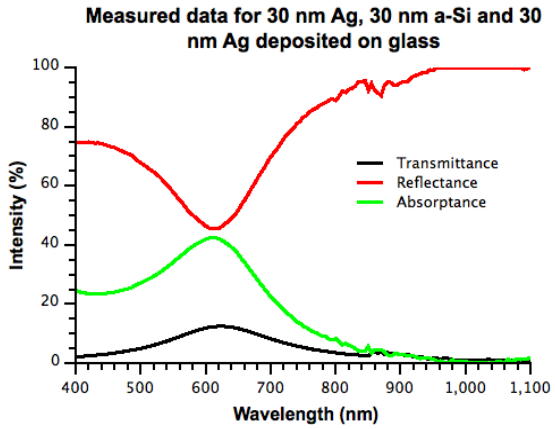

Figure 5.4: Reflectance (R) and transmittance (T) plots, in percentage, of a 30 nm Ag, 30 nm a-Si and 30 nm Ag structure deposited on glass. The absorptance is calculated using 100-T-R. Measurements are performed on a spectrophotometer with an integrating sphere.

Comparing the above values with those seen in Figure 5.1c (in blue), the absorptance plots are similar. The positions of the two absorptance peaks are near the measured values but do not match exactly. This may be due to different deposition rates for a-Si layer leading to change in thickness. The intensities of the measured and simulated plots also match qualitatively.

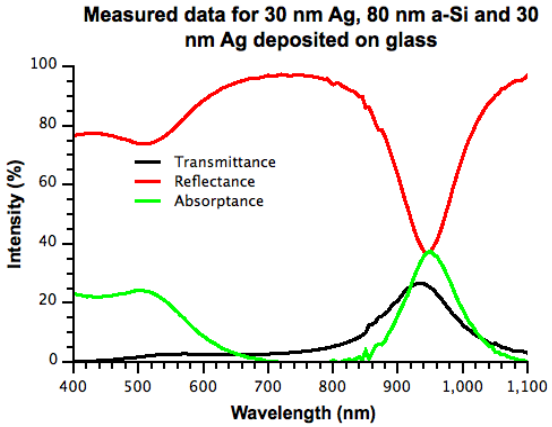

Figure 5.5: Measured reflectance (R) and transmittance (T) plots, in percentage, of a 30 nm Ag, 80 nm a-Si and 30 nm Ag structure deposited on glass. The absorptance is calculated using 100-T-R. Measurements are performed on a spectrophotometer with an integrating sphere to collect stray light.

In another measurement with p-i-n junctions, the absorptance of a freestanding metallized a-Si:H p-i-n junction 40 nm thick is compared with the absorptance of an unmetallized membrane with the same thickness. In Figure 5.6, the absorptance of a freestanding metallized membrane with 35 nm of metal film deposited on both sides of the 40 nm thick a-Si:H p-i-n junction is compared with a similar freestanding p-i-n junction without the metal layers. The figure shows that a resonant peak is seen at 680 nm for the metallized solar cell. The unmetallized membrane absorptivity is similar to that of a-Si silicon. The absorptance around the peak at 680 nm for the metallized p-i-n is higher than the absorptance of the unmetallized solar cell.

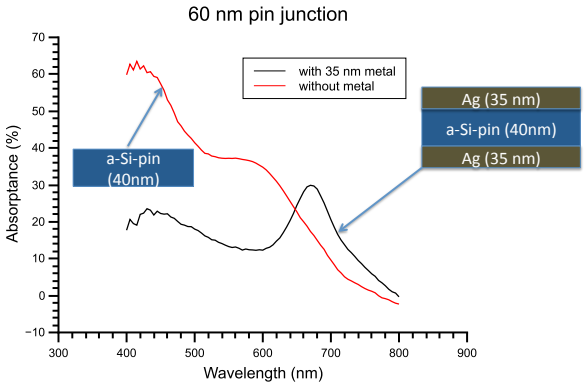

Figure 5.6: Absorptance measurements in percentage of a metallized 40 nm thick a-Si:H p-i-n junction solar cell compared with an unmetallized solar cell of the same thickness.

These measurements confirm with the simulation models and show that it is possible to tailor the optical absorption of such ultrathin metallized solar cells by changing the thickness of the semiconductor layer.

5.3.2 External Quantum Efficiency of Solar Cell Structures

External quantum efficiency (EQE) is a measurement of how efficient a solar cell is in converting photons into electricity. It is defined as the ratio of carriers collected by the contacts of the solar cell to the total number of photons falling on the solar cell within a given energy. The spectral response of the solar cell is usually plotted as the EQE against the wavelength [146]. The EQE curve and the current versus voltage (I-V) curve is a measure of the characteristics of the solar cell.

To measure the EQE characteristics of the solar cell a Xe lamp is used as a broadband source. The light from the source is passed through a collimator into an Oriel Cornerstone 130 1/8m monochromator. The light coming out of the monochromator is focused and

coupled into a fiber bundle that directs the light onto a lens. Here the light is focused onto the solar cell sample. The focused spot on the solar cell underfills the active area of the solar cell. Before measuring the solar cell a c-Si Hamamatzu S1781-12 diode is calibrated under the focused spot. The current from the diode is recorded at 10 nm wavelength increments. The incident power at each wavelength is calculated using the spectral sensitivity specification of the diode. The current from the solar cell is then measured under the same conditions to find out the ratio of the carriers collected by the contacts to the number of photons incident on it at the specific wavelength to calculate the EQE of the solar cell.

The I versus V curve of the device is plotted under illumination in Figure 5.7, for the 40 nm thick a-Si:H p-i-n solar cell, with 35 nm of metal on the illumination side and 50 nm of metal on the back side of the freestanding junction. The thicker metal is used in the backside to act like a partial mirror.

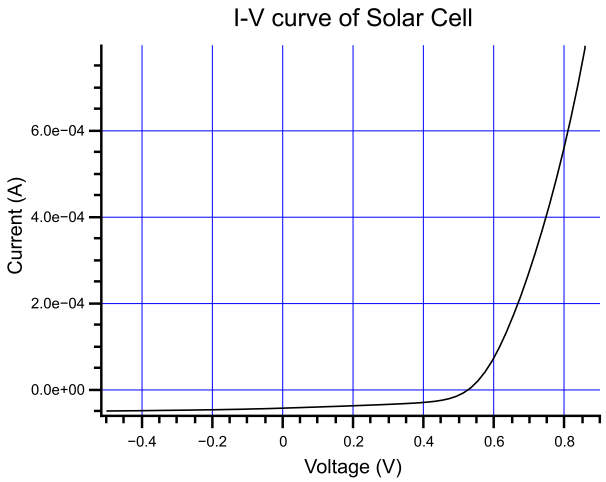

Figure 5.7: Current (I) versus voltage plot of the solar cell under illumination from AM 1.5.

The EQE of the device is plotted in Figure 5.8. A peak is seen at 650 nm indicating the cavity resonance effect seen in simulation and measured absorption data. The characteristics of the solar cell are shown in the table in the inset of Figure 5.8. Efficiency [147] is the ratio of the output energy of the solar cell to the total energy incident on the solar cell in form of solar radiation. From the table, the value of efficiency is only 0.20 %. This is low because the PECVD process used in making the p-i-n junction is not optimized. The short circuit current density, J_{SC} is defined as the current flowing through the solar cell when the voltage across it is zero. In our case, this is 0.67 mA/cm^2. Similarly, the shot circuit voltage is the defined as the voltage across the solar cell when no current is flowing through it. Here the short circuit voltage, V_{OC}=0.51 volts. The fill factor, defined, as the ratio of the maximum power to the product of the J_{SC} and V_{OC} is 0.59 in this cell.

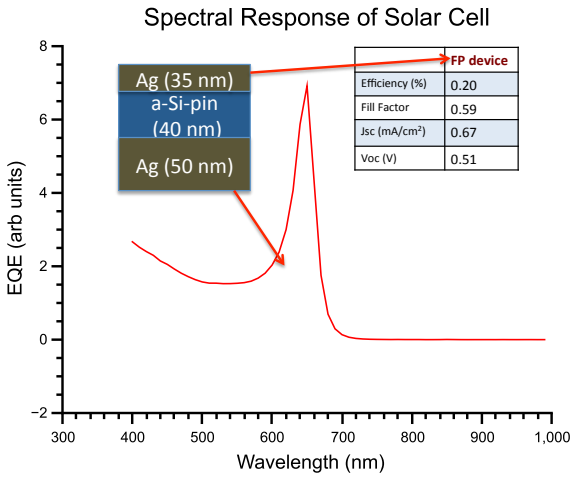

Figure 5.8: Spectral response of the solar cell with the EQE plotted against the wavelength, for a freestanding 40 nm thick a-Si:H p-i-n junction solar cell with 35 nm metal on the side facing illumination and 50 nm metal on the backside. The inset shows the characteristics of the solar cell.

To compare experimental and simulation results, the calculated absorption from simulations is compared with experimental EQE values shown in Figure 5.9. The experimental freestanding solar cell structure is a 40 nm a-Si:H p-i-n junction with 35 nm of Ag on both sides of the junction. This is plotted in black in Figure 5.9. For the FDTD simulation, the structure replaces the p-i-n junction with a material with the refractive index characteristics of a-Si. The red curve in the figure shows the absorption of the structure. There is good agreement to the position of the peaks, between the absorption and experimental EQE. The range of the measuring instrument limits the range of EQE measurements.

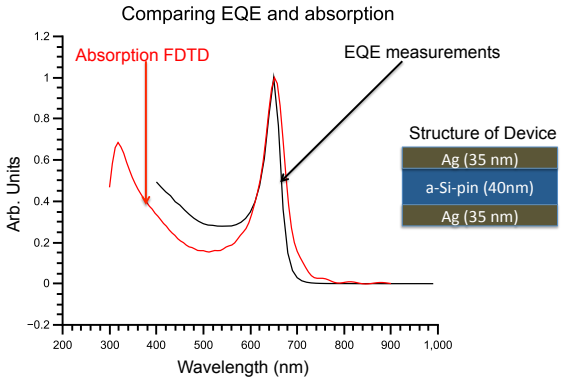

Figure 5.9: Comparison of FDTD simulated absorption profile of a 40 nm a-Si with 35 nm of Ag on both sides with EQE measurement from a similar freestanding a-Si:H p-i-n junction.

A good correspondence is seen between the simulated absorption results and experimental EQE measurements. Hence, different structures can be tested through simulations to predict the experimental spectral response of the solar cell.

5.3.3 Effect of Indium Tin Oxide (ITO) on the Solar Cell Structure

In the previous section, it is seen that the solar cell structure has thin metal films on both sides of the p-i-n junction that act as contacts as well as Fabry Perot mirrors to create a resonant cavity. It has been seen in Figure 2.20 that deposition of 20 nm of Ag on top of solar cells gives a fairly continuous contact. However, to make the contact even better, ITO can be deposited on top of the metal to decrease the sheet resistance of the metal films. ITO has been used in thin film solar cells [148] and a-Si solar cells [142,149] as a collector for charges. Adding ITO on top of the metal changes the optical characteristics of the freestanding thin film metallized structure. So, simulations on such ITO deposited structures are performed to see how it affects the optical absorption. Figure 5.10 shows the absorptance calculated from FDTD simulation of similar structures with and without ITO. The structure for the plot in red is of a freestanding structure with 60 nm of a-Si layer with 35 nm of Ag layers on both sides. The plot in black shows the same 60 nm a-Si layer and 35 nm Ag layers with 25 nm of ITO on the two metal films.

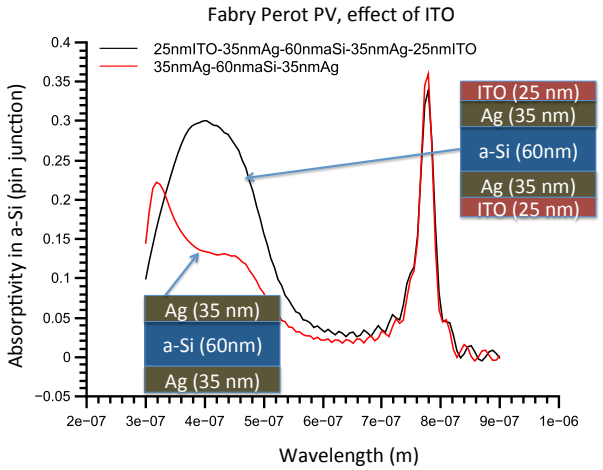

Figure 5.10: FDTD calculated absorptance (absorptivity) in the a-Si layer of a freestanding 60 nm a-Si layer with 35 nm of Ag layers on both sides shown in red. The plot in black shows calculated absorptivity of the same structure in the a-Si layer with 25 nm of ITO on both sides of the metal layers.

In Figure 5.10, it is seen that the absorptance in the a-Si layer increases in the spectrum range from 320 nm to 600 nm with the addition of the ITO layer on both sides of the structure. Although the cavity resonance peak at 780 nm decreases, overall there is an increase in the absorptivity of the structure when ITO is added. This is attributed to the index matching, as the refractive index of ITO is high (1.7 at 600 nm). The ITO layer acts like an index matching layer for the metal layer [150], so less light is reflected from the metal.

To confirm the increase in absorptance and hence the increase in the efficiency and performance of a solar cell, 20 nm of ITO is deposited on the front side of the solar cell. The performance of the ITO deposited solar cell is compared with the same solar cell before deposition of ITO. The results are plotted in Figure 5.11. The FP device is the solar cell without ITO (plotted in red), and the ITO FP device is the same device after

ITO deposition (plotted in black). From the EQE measurements, it is seen that overall EQE value for the ITO FP device increases when compared with the FP device. The EQE increases significantly from 400 nm to 600 nm. This increase is also reflected in the inset table in Figure 5.11 which tabulates the characteristic solar cell parameters. There is an increase of 45 % in the efficiency of the ITO FP device when compared with the FP device. The fill factor decreases, but the J_{SC} increases from 0.67 mA/cm^2 to 1.04 mA/cm^2. The V_{OC} remains unchanged.

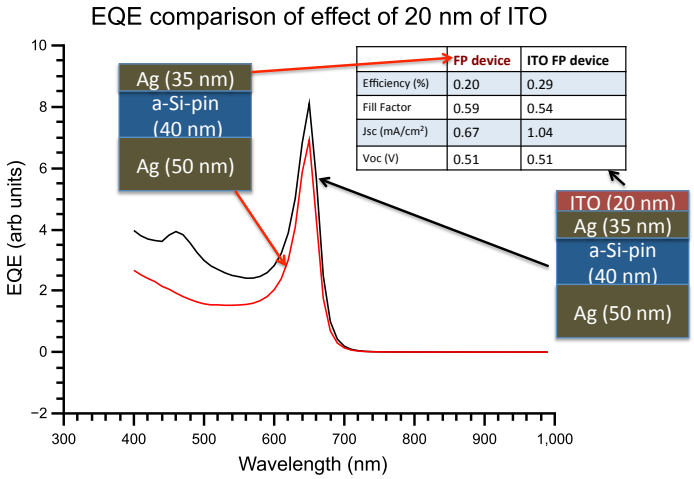

Figure 5.11: Comparison of solar cell EQE measurement before and after deposition of 20 nm of ITO on the front side of a freestanding 40 nm thick a-Si:H p-i-n junction with 35 nm of Ag on the front side and 50 nm of Ag on the backside. The inset tables compare the characteristic solar cell parameters before and after ITO deposition on the solar cells.

To compare the results with the simulation, 3D FDTD simulation on the above structure is performed. The absorptance in the a-Si layer of the structure is calculated and compared for a 40 nm a-Si freestanding membrane with 35 nm and 50 nm thick layer of Ag, on the front and back side respectively, with and without 20 nm ITO as depicted in Figure 5.12. The comparison is for the same structure shown in Figure 5.11. The

absorptance for the device with ITO is higher than the one without it. There is qualitative agreement with the EQE measurements in Figure 5.11, and the FDTD calculated absorptance.

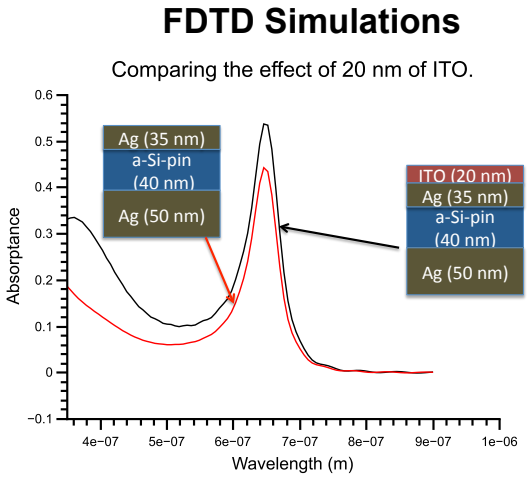

Figure 5.12: FDTD simulation of structures used in Figure 5.11, for comparing the simulation absorptance and EQE measurements. The calculated absorptance of the solar cell structures with and without ITO is presented in red and black plots, respectively.

5.4 Conclusion

In this chapter, a unique freestanding ultrathin membrane based solar cell is introduced. The device is inspired from simulation results in metallized membrane, which showed a Fabry Perot type resonant effect. The spectral response of this device can be designed to target the near infrared part of the solar spectrum by controlling the thickness of the p-i-n junction.

FDTD simulations of such structures calculated absorptance spectrum of the device. A strong correspondence was found between the simulated and experimental absorptance with EQE measurements of fabricated devices. Simulations also helped in designing structures with index matching layers, which helped in increasing the performance of these solar cells.

The solar cell can be designed to target the infrared region of the solar spectrum, so it can be used as the bottom layer in a tandem solar cell. The near infrared part will pass through the upper layers of the tandem cell and be absorbed in our device layer, while the visible part will be reflected to the upper layers. Another possible application is in near infrared detectors where currently there is a lack of cheap efficient detectors.

Chapter 6 Conclusion and Future Outlook

Pnc-Si membranes have been fabricated and used as a platform to make sensors and novel slot nanohole devices. To understand and predict the interaction of light with such devices, FDTD simulations have been used as a vital tool. The freestanding a-Si:H p-i-n junction solar cells were inspired by the fabrication and optical mode studies of the metallized pnc-Si membrane. Each section summarizes the results and discusses the future aspects of these devices.

6.1 Sensors based on Pnc-Si Membranes

As a first step in making a flowthrough sensor that would take advantage of the high permeance of the pnc-Si membranes, metallized pnc-Si membranes are studied as sensors.

Metal deposition of Ti and Au were performed to create metallized pnc-Si membranes. TEM and SEM images confirmed that the metal layer was continuous and successful in keeping the nanoholes open. Characterization of the deposited metal layer using AFM showed rms thickness to be 0.3 nm only. A novel method of angled deposition was also carried out. TEM image of such devices indicated the creation of structures inside the nanohole of the metallized pnc-Si membrane. Three dimensional model structures of the devices were analyzed using FDTD simulations. Scattering cross-sections and sensing properties of a single hole were investigated. In general, transmission calculations showed the presence of two peaks, one which red shifted and the other which blue shifted

with increasing refractive index of the surroundings. To model a Gaussian distribution of holes for mimicking part of the real metallized membrane, it was found that the blue shifting peak was the dominant peak during sensing. Experimental transmission measurements on these membranes confirmed the simulation results and experimental transmittance plots could be fitted with the help of simulation data. Polarization dependence of the transmission peak and sensitivity was seen experimentally and confirmed using simulation models of angled metal deposited pnc-Si membranes.

A major shortcoming to using these membranes for sensing is that the mode associated with sensing resides in the a-Si layer, i.e the insulator layer of the metal insulator metal structure. Certainly, the nanoholes do influence this mode as seen from the polarization dependence of transmission and sensitivity of this mode, but most of it is concentrated in the a-Si layer. This results in the loss of sensitivity for the device. Another impediment to better sensitivity is the Ti layer used as an adhesion layer for the Au metal. Although the thickness of Ti layer is less than 3 nm that is a fraction of the wavelength of light, simulations show that this layer absorbs light and affects sensitivity. Using a different method for deposition that can avoid such adhesion layer would improve the sensitivity. Simulations have shown that using a pnc-Si membrane with a bigger average size hole would improve the sensitivity. Until recently, such membranes were not available; a novel development to membrane design may help in improving the sensitivity of these devices.

6.2 Slot Effect in Metallized Pnc-Si Membranes

The slot effect was used in a novel way to enhance and localize the electric field mode inside the metallized pnc-Si membrane device. ALD deposition of Al_2O_3 to make the slots in the nanohole was consistent with the bottom-up approach for fabrication of the pnc-Si membrane and needed no precision lithographic techniques.

The fabrication process involved optimization of a new Kurt J. Lesker electron beam evaporator. TEM images of the slot nanoholes in the membranes showed the formation of the slot. The slot in the ~25 nm diameter nanohole was ~5 nm in size. Three-dimensional FDTD model simulations of a nanohole in the conformally deposited metallized pnc-Si membrane were performed. The simulations showed the enhancement and localization of the mode inside the air slot of the nanohole. The mode profile was consistent with the typical mode profile seen across a slot waveguide. Various nanohole and slot diameters together with metal thicknesses were simulated to find out the optimum parameters. The highest enhancement was found to be 29 for a 2.5 nm slot with the smallest mode volume being $4 \times 10^{-5}\ \mu m^3$.

The Ti adhesion layer optically reduces the enhancement factor because of absorption. Hence, a different technique of depositing Ag/Au metal on the pnc-Si membrane needs to be found. However, this slot concept should work in nanohole arrays or single nanohole in optically thick metal films. On our pnc-Si membrane, increasing the average size of nanoholes will allow the deposition of thicker metal films. These scenarios need to be modeled to optimize the fluorescence interaction. Experimental fluorescence studies must be performed to confirm enhancement of fluorescence signals.

6.3 Metallized Ultrathin Membranes as Solar Cells

The freestanding membrane based metallized ultrathin solar cells were inspired by the simulations showing the blue shift in sensing results with metallized pnc-Si membranes. This mode was found to be concentrated in the pnc-Si layer of the metal insulator metal structure. Since the refractive index of pnc-Si layer and a-Si:H p-i-n are not that different, this mode would get confined within the p-i-n junction to allow for the interaction of the photons to generate electron-hole pairs. The absorption spectra of such devices can be adjusted to target specific range of wavelengths in the solar spectrum.

The fabrication process followed from the fabrication of metallized pnc-Si membranes. The a-Si:H p-i-n junction was deposited using a GSI-PECVD tool. The smallest thickness of the p-i-n junction was 40 nm, the PECVD tool restricted this value. The metal layers on the front and back acted both as electrical conductors to carry charge as well as reflectors to create a cavity for trapping light. The experimental EQE measurements matched the absorption calculations in FDTD models of the solar cell. This gave a convenient method to optimize the structure for better light interaction. ITO layer was added to increase the index matching between layers and to raise the total absorption. Measurements corroborated with an increase in performance of such solar cells.

The efficiency of these devices is not high. There are a number of reasons for this. The primary reason is the quality of the a-Si:H p-i-n junction. The GSI-PECVD tool is not optimized to make solar cells and thus leads to very inefficient solar cells. The device allows for tuning the absorption profile of the solar cell to specific wavelengths. By the

very nature of this design, a large part of the solar spectrum is lost and thus the efficiency is expected to be low. However, this device can specifically target solar spectrum regions where other type of solar cells fail. Thinner a-Si:H p-i-n junctions with higher quality junctions can blue shift the absorption profile into the visible range to increase efficiency. Using patterning or nanoparticles to increase coupling of light can enhance the device performance. Performance of such devices can be predicted using simulations.

Bibliography

1. E. Ferain and R. Legras, "Characterisation of nanoporous particle track etched membrane," Nuclear Instruments and Methods in Physics Research Section B: Beam Interactions with Materials and Atoms **131**, 97–102 (1997).
2. A. Belwalkar, E. Grasing, W. Van Geertruyden, Z. Huang, and W. Z. Misiolek, "Effect of processing parameters on pore structure and thickness of anodic aluminum oxide (AAO) tubular membranes," Journal of Membrane Science **319**, 192–198 (2008).
3. M. Majumder, N. Chopra, R. Andrews, and B. J. Hinds, "Nanoscale hydrodynamics: Enhanced flow in carbon nanotubes," Nature **438**, 44–44 (2005).
4. H. D. Tong, H. V. Jansen, V. J. Gadgil, C. G. Bostan, E. Berenschot, C. J. M. van Rijn, and M. Elwenspoek, "Silicon Nitride Nanosieve Membrane," Nano Letters **4**, 283–287 (2004).
5. S. Unnikrishnan, H. V. Jansen, F. H. Falke, N. R. Tas, H. A. G. M. Van Wolferen, M. J. De Boer, R. G. P. Sanders, and M. C. Elwenspoek, "Transition flow through an ultra-thin nanosieve," Nanotechnology **20**, 305304 (2009).
6. C. C. Striemer, T. R. Gaborski, J. L. McGrath, and P. M. Fauchet, "Charge- and size-based separation of macromolecules using ultrathin silicon membranes," Nature **445**, 749–753 (2007).
7. A. van den Berg and M. Wessling, "Nanofluidics: Silicon for the perfect membrane," Nature **445**, 726–726 (2007).
8. M. N. Kavalenka, C. C. Striemer, D. Z. Fang, T. R. Gaborski, J. L. McGrath, and P. M. Fauchet, "Ballistic and non-ballistic gas flow through ultrathin nanopores," Nanotechnology **23**, 145706 (2012).
9. J. L. Snyder, A. Clark, D. Z. Fang, T. R. Gaborski, C. C. Striemer, P. M. Fauchet, and J. L. McGrath, "An experimental and theoretical analysis of molecular separations by diffusion through ultrathin nanoporous membranes," Journal of Membrane Science **369**, 119–129 (2011).
10. T. R. Gaborski, J. L. Snyder, C. C. Striemer, D. Z. Fang, M. Hoffman, P. M. Fauchet, and J. L. McGrath, "High-Performance Separation of Nanoparticles with Ultrathin Porous Nanocrystalline Silicon Membranes," ACS Nano **4**, 6973–6981 (2010).
11. A. A. Agrawal, B. J. Nehilla, K. V. Reisig, T. R. Gaborski, D. Z. Fang, C. C. Striemer, P. M. Fauchet, and J. L. McGrath, "Porous nanocrystalline silicon membranes as highly permeable and molecularly thin substrates for cell culture," Biomaterials **31**, 5408–5417 (2010).
12. J. W. F. Robertson, C. G. Rodrigues, V. M. Stanford, K. A. Rubinson, O. V. Krasilnikov, and J. J. Kasianowicz, "Single-molecule mass spectrometry in solution

using a solitary nanopore," Proceedings of the National Academy of Sciences **104**, 8207–8211 (2007).
13. D. Fologea, B. Ledden, D. S. McNabb, and J. Li, "Electrical characterization of protein molecules by a solid-state nanopore," Applied Physics Letters **91**, 053901–053901–3 (2007).
14. A. Han, M. Creus, G. Schürmann, V. Linder, T. R. Ward, N. F. de Rooij, and U. Staufer, "Label-Free Detection of Single Protein Molecules and Protein−Protein Interactions Using Synthetic Nanopores," Analytical Chemistry **80**, 4651–4658 (2008).
15. D. S. Talaga and J. Li, "Single-Molecule Protein Unfolding in Solid State Nanopores," Journal of the American Chemical Society **131**, 9287–9297 (2009).
16. S. van Dorp, U. F. Keyser, N. H. Dekker, C. Dekker, and S. G. Lemay, "Origin of the electrophoretic force on DNA in solid-state nanopores," Nature Physics **5**, 347–351 (2009).
17. M. Firnkes, D. Pedone, J. Knezevic, M. Döblinger, and U. Rant, "Electrically Facilitated Translocations of Proteins through Silicon Nitride Nanopores: Conjoint and Competitive Action of Diffusion, Electrophoresis, and Electroosmosis," Nano Letters **10**, 2162–2167 (2010).
18. F. Eftekhari, C. Escobedo, J. Ferreira, X. Duan, E. M. Girotto, A. G. Brolo, R. Gordon, and D. Sinton, "Nanoholes As Nanochannels: Flow-through Plasmonic Sensing," Analytical Chemistry **81**, 4308–4311 (2009).
19. G. M. Hwang, Lin Pang, E. H. Mullen, and Y. Fainman, "Plasmonic Sensing of Biological Analytes Through Nanoholes," Sensors Journal, IEEE **8**, 2074–2079 (2008).
20. G. Xiang, N. Zhang, and X. Zhou, "Localized Surface Plasmon Resonance Biosensing with Large Area of Gold Nanoholes Fabricated by Nanosphere Lithography," Nanoscale Research Letters **5**, 818–822 (2010).
21. R. Wei, D. Pedone, A. Zürner, M. Döblinger, and U. Rant, "Fabrication of Metallized Nanopores in Silicon Nitride Membranes for Single□Molecule Sensing," Small **6**, 1406–1414 (2010).
22. A.-P. Blanchard-Dionne, L. Guyot, S. Patskovsky, R. Gordon, and M. Meunier, "Intensity based surface plasmon resonance sensor using a nanohole rectangular array," Optics Express **19**, 15041–15046 (2011).
23. A. G. Brolo, R. Gordon, B. Leathem, and K. L. Kavanagh, "Surface Plasmon Sensor Based on the Enhanced Light Transmission through Arrays of Nanoholes in Gold Films," Langmuir **20**, 4813–4815 (2004).
24. H. Rigneault, J. Capoulade, J. Dintinger, J. Wenger, N. Bonod, E. Popov, T. W. Ebbesen, and P.-F. Lenne, "Enhancement of Single-Molecule Fluorescence Detection in Subwavelength Apertures," Physical Review Letters **95**, 117401 (2005).
25. M. J. Levene, "Zero-Mode Waveguides for Single-Molecule Analysis at High Concentrations," Science **299**, 682–686 (2003).

26. C. Escobedo, A. G. Brolo, R. Gordon, and D. Sinton, "Flow-through vs flow-over: analysis of transport and binding in nanohole array plasmonic biosensors," Analytical Chemistry **82**, 10015–10020 (2010).
27. M. P. Jonsson, A. B. Dahlin, L. Feuz, S. Petronis, and F. Höök, "Locally Functionalized Short-Range Ordered Nanoplasmonic Pores for Bioanalytical Sensing," Analytical Chemistry **82**, 2087–2094 (2010).
28. S. Hayashi, A. Maekawa, S. C. Kim, and M. Fujii, "Mechanism of enhanced light emission from an emitting layer embedded in metal-insulator-metal structures," Physical Review B **82**, 035441 (2010).
29. H. A. Bethe, "Theory of Diffraction by Small Holes," Phys. Rev. **66**, 163– (1944).
30. C. J. Bouwkamp, "On Bethe's theory of diffraction by small holes," Philips Research Reports **5**, 401–422 (1950).
31. T. W. Ebbesen, H. J. Lezec, H. F. Ghaemi, T. Thio, and P. A. Wolff, "Extraordinary optical transmission through sub-wavelength hole arrays," Nature **391**, 667–669 (1998).
32. F. J. Garcia-Vidal, L. Martin-Moreno, T. W. Ebbesen, and L. Kuipers, "Light passing through subwavelength apertures," Reviews of Modern Physics **82**, 729 (2010).
33. H. J. Lezec, A. Degiron, E. Devaux, R. A. Linke, L. Martin-Moreno, F. J. Garcia-Vidal, and T. W. Ebbesen, "Beaming Light from a Subwavelength Aperture," Science **297**, 820–822 (2002).
34. A. Degiron, H. J. Lezec, W. L. Barnes, and T. W. Ebbesen, "Effects of hole depth on enhanced light transmission through subwavelength hole arrays," Applied Physics Letters **81**, 4327 (2002).
35. J.-M. Yi, A. Cuche, F. de León-Pérez, A. Degiron, E. Laux, E. Devaux, C. Genet, J. Alegret, L. Martín-Moreno, and T. Ebbesen, "Diffraction Regimes of Single Holes," Physical Review Letters **109**, (2012).
36. R. Wannemacher, "Plasmon-supported transmission of light through nanometric holes in metallic thin films," Optics Communications **195**, 107–118 (2001).
37. G. C. des Francs, D. Molenda, U. C. Fischer, and A. Naber, "Enhanced light confinement in a triangular aperture: Experimental evidence and numerical calculations," Physical Review B **72**, 165111 (2005).
38. B. Sepúlveda, Y. Alaverdyan, J. Alegret, M. Käll, and P. Johansson, "Shape effects in the localized surface plasmon resonance of single nanoholes in thin metal films," Optics Express **16**, 5609 (2008).
39. S.-H. Chang, S. Gray, and G. Schatz, "Surface plasmon generation and light transmission by isolated nanoholes and arrays of nanoholes in thin metal films," Optics Express **13**, 3150–3165 (2005).
40. E. Popov, N. Bonod, M. Nevière, H. Rigneault, P.-F. Lenne, and P. Chaumet, "Surface plasmon excitation on a single subwavelength hole in a metallic sheet," Applied Optics **44**, 2332–2337 (2005).
41. S. G. Rodrigo, O. Mahboub, A. Degiron, C. Genet, F. J. Garcia-Vidal, L. Martin-Moreno, and T. W. Ebbesen, "Holes with very acute angles: a new paradigm of

extraordinary optical transmission through strongly localized modes," Optics Express **18**, 23691–23697 (2010).
42. E. M. Purcell, "Spontaneous emission probabilities at radio frequencies.," Physical Review **69**, 681–681 (1946).
43. P. Anger, P. Bharadwaj, and L. Novotny, "Enhancement and Quenching of Single-Molecule Fluorescence," Physical Review Letters **96**, 113002 (2006).
44. L. Novotny and B. Hecht, *Principles of Nano-optics* (Cambridge University Press, 2006).
45. R. R. Chance, A. Prock, and R. Silbey, "Molecular Fluorescence and Energy Transfer Near Interfaces," in *Advances in Chemical Physics*, I. Prigogine and S. A. Rice, eds. (John Wiley & Sons, Inc., 2007), pp. 1–65.
46. S. Kühn, U. Håkanson, L. Rogobete, and V. Sandoghdar, "Enhancement of Single-Molecule Fluorescence Using a Gold Nanoparticle as an Optical Nanoantenna," Physical Review Letters **97**, 017402 (2006).
47. J. Zhang, Y. Fu, M. H. Chowdhury, and J. R. Lakowicz, "Metal-Enhanced Single-Molecule Fluorescence on Silver Particle Monomer and Dimer: Coupling Effect between Metal Particles," Nano Letters **7**, 2101–2107 (2007).
48. Y. Zhang, K. Aslan, M. J. R. Previte, and C. D. Geddes, "Metal-enhanced fluorescence: Surface plasmons can radiate a fluorophore's structured emission," Applied Physics Letters **90**, 053107–053107–3 (2007).
49. F. Tam, G. P. Goodrich, B. R. Johnson, and N. J. Halas, "Plasmonic Enhancement of Molecular Fluorescence," Nano Letters **7**, 496–501 (2007).
50. J. Enderlein and T. Ruckstuhl, "The efficiency of surface-plasmon coupled emission for sensitive fluorescence detection," Optics Express **13**, 8855–8865 (2005).
51. Y. Liu and S. Blair, "Fluorescence enhancement from an array of subwavelength metal apertures," Optics Letters **28**, 507–509 (2003).
52. A. G. Brolo, S. C. Kwok, M. D. Cooper, M. G. Moffitt, C.-W. Wang, R. Gordon, J. Riordon, and K. L. Kavanagh, "Surface Plasmon−Quantum Dot Coupling from Arrays of Nanoholes," The Journal of Physical Chemistry B **110**, 8307–8313 (2006).
53. J. H. Kim and P. J. Moyer, "Laser-induced fluorescence within subwavelength metallic arrays of nanoholes indicating minimal dependence on hole periodicity," Applied Physics Letters **90**, 131111–131111–3 (2007).
54. A. G. Brolo, S. C. Kwok, M. G. Moffitt, R. Gordon, J. Riordon, and K. L. Kavanagh, "Enhanced Fluorescence from Arrays of Nanoholes in a Gold Film," Journal of the American Chemical Society **127**, 14936–14941 (2005).
55. P.-F. Guo, S. Wu, Q.-J. Ren, J. Lu, Z. Chen, S.-J. Xiao, and Y.-Y. Zhu, "Fluorescence Enhancement by Surface Plasmon Polaritons on Metallic Nanohole Arrays," The Journal of Physical Chemistry Letters **1**, 315–318 (2010).
56. U. C. Fischer, "Submicrometer aperture in a thin metal film as a probe of its microenvironment through enhanced light scattering and fluorescence," Journal of the Optical Society of America B **3**, 1239–1244 (1986).

57. D. Sinton, R. Gordon, and A. G. Brolo, "Nanohole arrays in metal films as optofluidic elements: progress and potential," Microfluid Nanofluid **4**, 107–116 (2007).
58. K. Shome, M. Kavalenka, D. Z. Fang, and P. M. Fauchet, "Metallized ultrathin porous silicon membranes for biological sensing using SERS," in *Frontiers in Pathogen Detection: From Nanosensors to Systems*, P. M. Fauchet and B. L. Miller, eds. (SPIE, 2010), Vol. 7553, p. 75530F–9.
59. H. Aouani, O. Mahboub, E. Devaux, H. Rigneault, T. W. Ebbesen, and J. Wenger, "Large molecular fluorescence enhancement by a nanoaperture with plasmonic corrugations," Optics Express **19**, 13056–13062 (2011).
60. J. Wenger, D. Gerard, J. Dintinger, O. Mahboub, N. Bonod, E. Popov, T. W. Ebbesen, and H. Rigneault, "Emission and excitation contributions to enhanced single molecule fluorescence by gold nanometric apertures," Optics Express **16**, 3008–3020 (2008).
61. V. R. Almeida, Q. Xu, C. A. Barrios, and M. Lipson, "Guiding and confining light in void nanostructure," Optics Letters **29**, 1209–1211 (2004).
62. C. A. Barrios, M. J. Bañuls, V. González-Pedro, K. B. Gylfason, B. Sánchez, A. Griol, A. Maquieira, H. Sohlström, M. Holgado, and R. Casquel, "Label-free optical biosensing with slot-waveguides," Optics Letters **33**, 708 (2008).
63. C. A. Barrios, "Optical Slot-Waveguide Based Biochemical Sensors," Sensors **9**, 4751–4765 (2009).
64. A. H. J. Yang, S. D. Moore, B. S. Schmidt, M. Klug, M. Lipson, and D. Erickson, "Optical manipulation of nanoparticles and biomolecules in sub-wavelength slot waveguides," Nature **457**, 71–75 (2009).
65. J. Robinson, C. Manolatou, L. Chen, and M. Lipson, "Ultrasmall Mode Volumes in Dielectric Optical Microcavities," Physical Review Letters **95**, (2005).
66. W. D. Nordhaus, "A Review of the Stern Review on the Economics of Climate Change," Journal of Economic Literature **45**, 686–702 (2007).
67. M. S. Dresselhaus and I. L. Thomas, "Alternative energy technologies," Nature **414**, 332–337 (2001).
68. F. Manzano-Agugliaro, A. Alcayde, F. G. Montoya, A. Zapata-Sierra, and C. Gil, "Scientific production of renewable energies worldwide: An overview," Renewable and Sustainable Energy Reviews **18**, 134–143 (2013).
69. T. B. Johansson, *Renewable Energy: Sources for Fuels and Electricity* (Island Press, 1993).
70. Nave, R., http://hyperphysics.phy-astr.gsu.edu/hbase/tables/elabund.html.
71. A. V. Shah, H. Schade, M. Vanecek, J. Meier, E. Vallat-Sauvain, N. Wyrsch, U. Kroll, C. Droz, and J. Bailat, "Thin-film silicon solar cell technology," Progress in Photovoltaics: Research and Applications **12**, 113–142 (2004).
72. H. W. Schock, "Thin film photovoltaics," Applied Surface Science **92**, 606–616 (1996).
73. D. E. Carlson, C. R. Wronski, J. I. Pankove, P. J. Zanzucchi, and D. L. Staebler, "Properties of amorphous silicon and a-Si solar cells," http://adsabs.harvard.edu/abs/1977RCARv..38..211C.

74. M. Konagai, M. Sugimoto, and K. Takahashi, "High efficiency GaAs thin film solar cells by peeled film technology," Journal of Crystal Growth **45**, 277–280 (1978).
75. J. Britt and C. Ferekides, "Thin□film CdS/CdTe solar cell with 15.8% efficiency," Applied Physics Letters **62**, 2851–2852 (1993).
76. X. Wu, "High-efficiency polycrystalline CdTe thin-film solar cells," Solar Energy **77**, 803–814 (2004).
77. A. Romeo, M. Terheggen, D. Abou-Ras, D. L. Bätzner, F.-J. Haug, M. Kälin, D. Rudmann, and A. N. Tiwari, "Development of thin-film Cu(In,Ga)Se2 and CdTe solar cells," Progress in Photovoltaics: Research and Applications **12**, 93–111 (2004).
78. H. A. Atwater and A. Polman, "Plasmonics for improved photovoltaic devices," Nature Materials **9**, 205–213 (2010).
79. A. Luque and S. Hegedus, *Handbook of Photovoltaic Science and Engineering* (John Wiley and Sons, 2003).
80. V. E. Ferry, L. A. Sweatlock, D. Pacifici, and H. A. Atwater, "Plasmonic Nanostructure Design for Efficient Light Coupling into Solar Cells," Nano Letters **8**, 4391–4397 (2008).
81. B. O'Connor, C. Haughn, K.-H. An, K. P. Pipe, and M. Shtein, "Transparent and conductive electrodes based on unpatterned, thin metal films," Applied Physics Letters **93**, 223304 (2008).
82. W. U. Huynh, J. J. Dittmer, and A. P. Alivisatos, "Hybrid Nanorod-Polymer Solar Cells," Science **295**, 2425–2427 (2002).
83. D. Derkacs, S. H. Lim, P. Matheu, W. Mar, and E. T. Yu, "Improved performance of amorphous silicon solar cells via scattering from surface plasmon polaritons in nearby metallic nanoparticles," Applied Physics Letters **89**, 093103–093103–3 (2006).
84. Y. Kuang, K. H. M. van der Werf, Z. S. Houweling, and R. E. I. Schropp, "Nanorod solar cell with an ultrathin a-Si:H absorber layer," Applied Physics Letters **98**, 113111 (2011).
85. R. Kappera, W. Warrick, and M. B. Tayahi, "Nanohole structures for efficiency enhancement in thin film photovoltaics," in *2010 International Conference on Photonics (ICP)* (2010), pp. 1 –5.
86. Y. Ichikawa, S. Fujikake, H. Ohta, T. Sasaki, and H. Sakai, "12% two-stacked a-Si:H tandem cells with a new p-layer structure," in *Photovoltaic Specialists Conference, 1991., Conference Record of the Twenty Second IEEE* (1991), pp. 1296–1301 vol.2.
87. J. Y. Kim, K. Lee, N. E. Coates, D. Moses, T.-Q. Nguyen, M. Dante, and A. J. Heeger, "Efficient Tandem Polymer Solar Cells Fabricated by All-Solution Processing," Science **317**, 222–225 (2007).
88. C.-C. Chen, L. Dou, R. Zhu, C.-H. Chung, T.-B. Song, Y. B. Zheng, S. Hawks, G. Li, P. S. Weiss, and Y. Yang, "Visibly Transparent Polymer Solar Cells Produced by Solution Processing," ACS Nano **6**, 7185–7190 (2012).

89. D. Z. Fang, C. C. Striemer, T. R. Gaborski, J. L. McGrath, and P. M. Fauchet, "Methods for controlling the pore properties of ultra-thin nanocrystalline silicon membranes," Journal of Physics: Condensed Matter **22**, 454134 (2010).
90. W. Kern, *Handbook of Semiconductor Wafer Cleaning Technology: Science, Technology, and Applications* (Noyes Publ., 1993).
91. L. Reimer and H. Kohl, *Transmission Electron Microscopy: Physics of Image Formation* (Springer, 2008).
92. G. Binnig, C. F. Quate, and C. Gerber, "Atomic Force Microscope," Physical Review Letters **56**, 930–933 (1986).
93. G. Binnig and H. Rohrer, "Scanning tunneling microscope," U.S. patent 4343993 (August 10, 1982).
94. T. Suntola and J. Antson, "Method for producing compound thin films," U.S. patent 4058430 (November 15, 1977).
95. H. S. Nalwa, *Handbook of Thin Film Materials: Deposition and Processing of Thin Films* (Academic Press, 2002).
96. D. Z. Fang, "Fabrication, Characterization, and Functionalization of Porous Nanocrystalline Silicon Membranes," Ph.D., University of Rochester (2011).
97. N. P. Kobayashi, C. L. Donley, S.-Y. Wang, and R. S. Williams, "Atomic layer deposition of aluminum oxide on hydrophobic and hydrophilic surfaces," Journal of Crystal Growth **299**, 218–222 (2007).
98. T. Smith, "The hydrophilic nature of a clean gold surface," Journal of Colloid and Interface Science **75**, 51–55 (1980).
99. J.-Y. Kwon, T.-S. Yoon, K.-B. Kim, and S.-H. Min, "Comparison of the agglomeration behavior of Au and Cu films sputter deposited on silicon dioxide," Journal of Applied Physics **93**, 3270–3278 (2003).
100. F. Y. Génin, W. W. Mullins, and P. Wynblatt, "Capillary instabilities in thin films: A model of thermal pitting at grain boundary vertices," Acta Metallurgica et Materialia **40**, 3239–3248 (1992).
101. K. T. Miller, F. F. Lange, and D. B. Marshall, "The instability of polycrystalline thin films: Experiment and theory," Journal of Materials Research **5**, 151–160 (1990).
102. D. J. Srolovitz and S. A. Safran, "Capillary instabilities in thin films. I. Energetics," Journal of Applied Physics **60**, 247–254 (1986).
103. T. P. Nolan, R. Sinclair, and R. Beyers, "Modeling of agglomeration in polycrystalline thin films: Application to TiSi2 on a silicon substrate," Journal of Applied Physics **71**, 720–724 (1992).
104. J. Homola, I. Koudela, and S. S. Yee, "Surface plasmon resonance sensors based on diffraction gratings and prism couplers: sensitivity comparison," Sensors and Actuators B: Chemical **54**, 16–24 (1999).
105. C. Nylander, B. Liedberg, and T. Lind, "Gas detection by means of surface plasmon resonance," Sensors and Actuators **3**, 79–88 (1982).
106. P. S. Vukusic, G. P. Bryan-Brown, and J. R. Sambles, "Surface plasmon resonance on gratings as a novel means for gas sensing," Sensors and Actuators B: Chemical **8**, 155–160 (1992).

107. P. Pfeifer, U. Aldinger, G. Schwotzer, S. Diekmann, and P. Steinrücke, "Real time sensing of specific molecular binding using surface plasmon resonance spectroscopy," Sensors and Actuators B: Chemical **54**, 166–175 (1999).
108. M. J. Jory, P. S. Vukusic, and J. R. Sambles, "Development of a prototype gas sensor using surface plasmon resonance on gratings," Sensors and Actuators B: Chemical **17**, 203–209 (1994).
109. J. Dostálek, J. Homola, and M. Miler, "Rich information format surface plasmon resonance biosensor based on array of diffraction gratings," Sensors and Actuators B: Chemical **107**, 154–161 (2005).
110. Y.-D. Su, S.-J. Chen, and T.-L. Yeh, "Common-path phase-shift interferometry surface plasmon resonance imaging system," Optics Letters **30**, 1488–1490 (2005).
111. S. B. Cohn, "The Electric Polarizability of Apertures of Arbitrary Shape," Proceedings of the IRE **40**, 1069–1071 (1952).
112. C. Genet and T. W. Ebbesen, "Light in tiny holes," Nature **445**, 39–46 (2007).
113. T. Rindzevicius, Y. Alaverdyan, B. Sepulveda, T. Pakizeh, M. Kall, R. Hillenbrand, J. Aizpurua, and F. J. Garcia de Abajo, "Nanohole Plasmons in Optically Thin Gold Films," The Journal of Physical Chemistry C **111**, 1207–1212 (2007).
114. K. A. Tetz, L. Pang, and Y. Fainman, "High-resolution surface plasmon resonance sensor based on linewidth-optimized nanohole array transmittance," Optics Letters **31**, 1528–1530 (2006).
115. H. F. Ghaemi, T. Thio, D. E. Grupp, T. W. Ebbesen, and H. J. Lezec, "Surface plasmons enhance optical transmission through subwavelength holes," Physical Review B **58**, 6779 (1998).
116. A. A. Yanik, M. Huang, A. Artar, T.-Y. Chang, and H. Altug, "Integrated nanoplasmonic-nanofluidic biosensors with targeted delivery of analytes," Applied Physics Letters **96**, 021101–3 (2010).
117. A. Dahlin, M. Zäch, T. Rindzevicius, M. Käll, D. S. Sutherland, and F. Höök, "Localized Surface Plasmon Resonance Sensing of Lipid-Membrane-Mediated Biorecognition Events," Journal of the American Chemical Society **127**, 5043–5048 (2005).
118. T. Rindzevicius, Y. Alaverdyan, A. Dahlin, F. Hook, D. S. Sutherland, and M. Kall, "Plasmonic Sensing Characteristics of Single Nanometric Holes," Nano Letters **5**, 2335–2339 (2005).
119. D. Gao, W. Chen, A. Mulchandani, and J. S. Schultz, "Detection of tumor markers based on extinction spectra of visible light passing through gold nanoholes," Applied Physics Letters **90**, 073901 (2007).
120. Kane Yee, "Numerical solution of initial boundary value problems involving maxwell's equations in isotropic media," Antennas and Propagation, IEEE Transactions on **14**, 302–307 (1966).
121. A. Taflove and M. E. Brodwin, "Numerical Solution of Steady-State Electromagnetic Scattering Problems Using the Time-Dependent Maxwell's Equations," Microwave Theory and Techniques, IEEE Transactions on **23**, 623–630 (1975).

122. P. B. Johnson and R. W. Christy, "Optical Constants of the Noble Metals," Physical Review B **6**, 4370 (1972).
123. E. D. Palik, *Handbook of Optical Constants of Solids II* (Academic Press, 1991).
124. M. Futamata, Y. Maruyama, and M. Ishikawa, "Local Electric Field and Scattering Cross Section of Ag Nanoparticles under Surface Plasmon Resonance by Finite Difference Time Domain Method," The Journal of Physical Chemistry B **107**, 7607–7617 (2003).
125. L. J. E. Anderson, K. M. Mayer, R. D. Fraleigh, Y. Yang, S. Lee, and J. H. Hafner, "Quantitative Measurements of Individual Gold Nanoparticle Scattering Cross Sections," The Journal of Physical Chemistry C **114**, 11127–11132 (2010).
126. P. K. Jain, K. S. Lee, I. H. El-Sayed, and M. A. El-Sayed, "Calculated absorption and scattering properties of gold nanoparticles of different size, shape, and composition: applications in biological imaging and biomedicine," The Journal of Physical Chemistry B **110**, 7238–7248 (2006).
127. L. Pang, G. M. Hwang, B. Slutsky, and Y. Fainman, "Spectral sensitivity of two-dimensional nanohole array surface plasmon polariton resonance sensor," Applied Physics Letters **91**, 123112 (2007).
128. K. Kneipp, Y. Wang, H. Kneipp, L. Perelman, I. Itzkan, R. Dasari, and M. Feld, "Single Molecule Detection Using Surface-Enhanced Raman Scattering (SERS)," Physical Review Letters **78**, 1667–1670 (1997).
129. H. Cang, A. Labno, C. Lu, X. Yin, M. Liu, C. Gladden, Y. Liu, and X. Zhang, "Probing the electromagnetic field of a 15-nanometre hotspot by single molecule imaging," Nature **469**, 385–388 (2011).
130. H.-I. Peng, C. M. Strohsahl, K. E. Leach, T. D. Krauss, and B. L. Miller, "Label-Free DNA Detection on Nanostructured Ag Surfaces," ACS Nano **3**, 2265–2273 (2009).
131. H.-I. Peng, Z. M. Nuffer, and B. L. Miller, "The role of alkanethiol spacers in a metal surface-based label-free DNA detection system," in *Frontiers in Pathogen Detection: From Nanosensors to Systems* (2009), p. 71670T–71670T–8.
132. J. D. Jackson, *Classical Electrodynamics Third Edition*, 3rd ed. (Wiley, 1998).
133. D. J. Griffiths, *Introduction to electrodynamics* (Prentice Hall, 1999).
134. D. K. Gramotnev and S. I. Bozhevolnyi, "Plasmonics beyond the diffraction limit," Nature Photonics **4**, 83–91 (2010).
135. K. J. Vahala, "Optical microcavities," Nature **424**, 839–846 (2003).
136. S.-H. Kwon, T. Sünner, M. Kamp, and A. Forchel, "Ultrahigh-Q photonic crystal cavity created by modulating air hole radius of a waveguide," Optics Express **16**, 4605 (2008).
137. M. J. Levene, J. Korlach, S. W. Turner, M. Foquet, H. G. Craighead, and W. W. Webb, "Zero-Mode Waveguides for Single-Molecule Analysis at High Concentrations," Science **299**, 682 –686 (2003).
138. N. Bonod, E. Popov, D. Gerard, J. Wenger, and H. Rigneault, "Field enhancement in a circular aperture surrounded by a single channel groove," Optics Express **16**, 2276–2287 (2008).

139. E. G. Hertwich and G. P. Peters, "Carbon Footprint of Nations: A Global, Trade-Linked Analysis," Environ. Sci. Technol. **43**, 6414–6420 (2009).
140. A. J. Dekker, *Solid State Physics* (Macmillan India Limited, 2000).
141. R. B. Bergmann, "Crystalline Si thin-film solar cells: a review," Applied Physics A **69**, 187–194 (1999).
142. V. E. Ferry, M. A. Verschuuren, H. B. T. Li, R. E. I. Schropp, H. A. Atwater, and A. Polman, "Improved red-response in thin film a-Si:H solar cells with soft-imprinted plasmonic back reflectors," Applied Physics Letters **95**, 183503 (2009).
143. M. Born and E. Wolf, *Principles of Optics: Electromagnetic Theory of Propagation, Interference and Diffraction of Light* (Cambridge University Press, 1999).
144. Y. Long, "Improving optical performance of inverted organic solar cells by microcavity effect," Applied Physics Letters **95**, 193301 (2009).
145. "http://rredc.nrel.gov/solar/spectra/am1.5/," (n.d.).
146. M. A. Green, K. Emery, Y. Hishikawa, W. Warta, and E. D. Dunlop, "Solar cell efficiency tables (version 39)," Progress in Photovoltaics: Research and Applications **20**, 12–20 (2012).
147. S. Benagli, D. Borrello, E. Vallat-Sauvain, J. Meier, U. Kroll, J. Hoetzel, J. Spitznagel, J. Steinhauser, L. Castens, and Y. Djeridane, "High-efficiency amorphous silicon devices on LPCVD-ZnO TCO prepared in industrial KAI-M R&D reactor," in *24th European Photovoltaic Solar Energy Conference, Hamburg* (2009), pp. 344–349.
148. Y. Ogawa, A. Jäger-Waldau, Y. Hashimoto, and K. Ito, "In_2O_3/CdS/CuInS_2$ Thin-Film Solar Cell with 9.7% Efficiency," Japanese Journal of Applied Physics **33**, L1775–L1777 (1994).
149. D. E. Carlson and C. R. Wronski, "Amorphous silicon solar cell," Applied Physics Letters **28**, 671–673 (1976).
150. C. H. Hsu, Y. P. Lin, H. J. Hsu, and C. C. Tsai, "Enhanced spectral response by silicon nitride index matching layer in amorphous silicon thin-film solar cells," Journal of Non-Crystalline Solids **358**, 2324–2326 (2012).